III-V Semiconductor Photonic Devices for Scalable Quantum Architectures

By

Alexander James Morris

Faculty of Science
Department of Physics and Astronomy
University of Sheffield

Submitted to the University of Sheffield in partial fulfilment of the requirements for the degree of Master of Philosophy

April 2023

Abstract

This thesis describes the optimisation of nanophotonic elements for on-chip integration with III-V semiconductor InAs/GaAs quantum dot single-photon sources and the investigation of photon-mediated interactions between pairs of quantum dots in nanophotonic waveguides.

Effective coupling of light on/off-chip is important for the study of light-matter interactions in nanophotonic systems and for efficient operation of quantum optical devices, such as single-photon sources. Here, optimisation of a circular grating outcoupler coupled to a nanophotonic waveguide is investigated for efficient on/off-chip light coupling. Broadband light input demonstrates increased transmission into an off-chip optical fibre and reduced reflection back into the waveguide, compared to the previous best design, for the InAs/GaAs quantum dot emission wavelength region of 900-950 nm. On-chip control and routing requires nanophotonic beamsplitters. Two approaches are investigated here. The first is a directional coupler beamsplitter, designed with a wider waveguide separation for better fabrication tolerance, providing even splitting with minimal loss in simulation. The second is a multimode interferometer beamsplitter, designed with two permutations of input/output waveguides, whereby broadband light transmission demonstrates even splitting with minimal loss for both designs.

Finally, photon-mediated interactions between pairs of quantum dots in a nanophotonic waveguide are studied. Understanding such interactions is important for nanophotonic systems in which multiple quantum dots interact. The temporal dynamics of a waveguide-embedded quantum dot pair is simulated, demonstrating superradiant and subradiant effects on the coupled quantum dot decay times. Experimentally, quantum dots are resonantly coupled using an applied magnetic field, the photon statistics revealed by Hanbury Brown-Twiss interferometry. For a coupled quantum dot pair in a nanophotonic waveguide, a coherent punching peak is observed, the signature of superradiance.

Acknowledgments

My research was funded by a three-year scholarship from the Doctoral Training Partnership of the Engineering and Physical Sciences Research Council (EPSRC). I worked in the Low Dimensional Structures and Devices group (LDSD) in the Department of Physics and Astronomy at the University of Sheffield. I recognise that my work would not be possible without the infrastructure of LDSD, the people that built it, and the people that maintain it. I would like to thank my two supervisors Maurice and Luke, for keeping my projects and I on track. I would also like to thank Andrew and Dom for their fantastic guidance. I should not forget to thank Sam for writing the basis of the Python code used in my superradiance simulations, or René for fabricating all the photonic devices studied in my thesis. I am grateful for the help I received from the many people of LDSD, each playing an important role in my development. Additionally, I thank my parents for their continuous support through some rather arduous years. Finally, I would like to thank my friends Matthew, James, and Tim, for keeping me entertained.

Conferences

- **A. Morris**, D. Hallett, A. P. Foster, M. S. Skolnick and L. R. Wilson, "*Towards Resonant Coupling of Quantum Dots in Nanophotonic Waveguides*", poster presentation, PG Away Day, 2020.
- **A. Morris**, D. Hallett, S. Sheldon, A. P. Foster, R. Dost, J. Iles-Smith, M. S. Skolnick and L. R. Wilson, "*Superradiant Emission from Chirally Coupled InGaAs Quantum Dots*", oral presentation, UK Semiconductors, 2022.

List of figures

Page

List of tables

Page

Contents

1 Theory

1.1 Quantum information processing

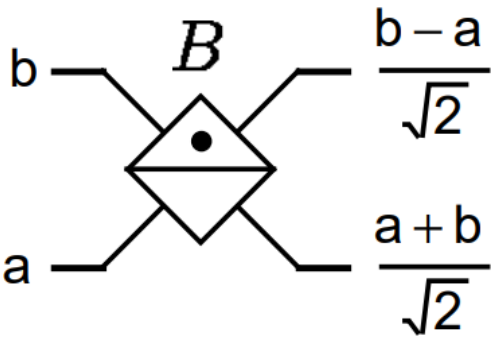

Figure 1.1. 50/50 optical beamsplitter with quantum operator "B" acting on the inequivalent modes "a" and "b" [1].

Solid-state computer chips harnessing the principles of classical physics are struggling to process sufficiently large quantities of information, because chip miniaturization has achieved an increase in capacity but has introduced perturbing quantum mechanical effects. However, these unwanted artefacts can be exploited to boost processing power, by harnessing photonic emissions from tiny semiconductor particles known as quantum dots (QDs) [2]. A QD is an artificial atom whereby an electron is confined to a single point, capable of absorbing or emitting light at any wavelength depending on its size and material [3]. Information transfer via photons has been accomplished with commercially available

quantum key distribution systems, providing enhanced security by communicating information encoded into photons, enabling two parties to share a protected encryption key. An eavesdropper cannot extract more than a tiny fraction of information about the key before being detected [4].

Classical communication employs the binomial model, whereby a system has two possible states at each time step. If the states "0" and "1" are the basis states of this model, then a qubit is a linear combination of these basis states, forming the principle of quantum communication [5]. In a model which uses photons as carriers of information, the vacuum state may be represented as $|0\rangle$, and the single-photon state may be represented as $|1\rangle$. The superposition state is then

$$|\psi\rangle = \frac{1}{\sqrt{2}}[|0\rangle + |1\rangle] \qquad 1.1$$

where the fraction normalizes the wavefunction $|\psi\rangle$ so the total probability is unity, since the probability of each state is determined by the square of the state's coefficient. A 50/50 optical beamsplitter may then be used to generate a superposition state, operating on two inequivalent modes "a" and "b" through the quantum operator "B" (Figure 1.1). If a = 0 and b = 1, then the beamsplitter input may be written as $|ab\rangle = |01\rangle$, outputting

$$B|01\rangle = \frac{1}{\sqrt{2}}[|01\rangle + |10\rangle] \qquad 1.2$$

which describes a quantum beamsplitter, a component in a quantum circuit [1]. For information transfer using photons, the following is required: high photon purity, high photon-emitter coupling efficiency, and photon indistinguishability. A QD satisfies all three requirements, as it possesses well-defined spin-states for effective coupling to photons [6].

1.2 Quantum dot growth

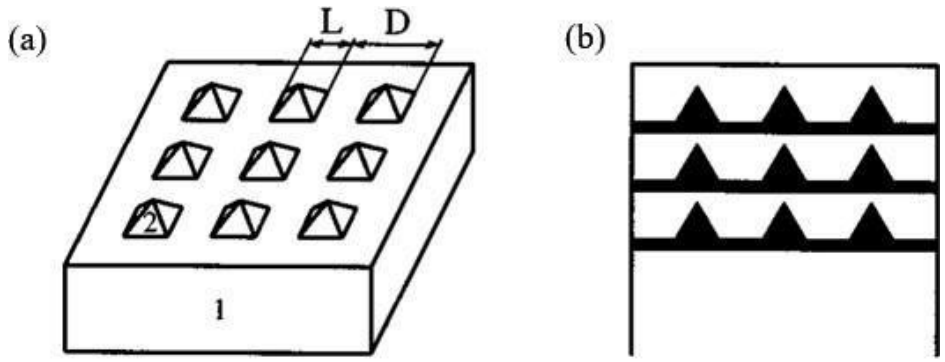

Figure 1.2. Schematics of a spontaneously ordered nanostructure. a) Array of coherently-strained three-dimensional islands (QDs). L is the width of the island, D is the lattice constant of the islands, 1 is the substrate material, and 2 is the island material. b) Cross-section of a multi-sheet array of three-dimensional islands (QDs) [7].

QDs are cultivated by heteroepitaxy, in which a film of a certain material is deposited on a substrate of a different material, creating lattice mismatch, encouraging the growth of a strained film. Over time, more layers of the film stack on top of each other, until a critical thickness is reached, forming a wafer containing three dimensional islands (Figure 1.2). This phase of self-assembled QD development is named the Stranski-Krastanov transition, occurring as an effort to reduce the strain energy of the system [8].

A film is typically deposited onto the substrate by molecular beam epitaxy (MBE). The desired chemical elements are heated in separate effusion cells, where they sublime/condense on the substrate through a beam of evaporated atoms. This process takes place under an ultra-high vacuum, establishing a long mean free path for the atoms,

ensuring that they do not interact with anything until they reach the substrate. MBE is advantageous to other methods due to its slow deposition rate of less than 1 µm per hour (which enhances film growth), and the ability to monitor the process step-by-step thanks to the high-vacuum environment [9].

The growth procedure commonly involves adding impurities to enhance the electrical properties of the QDs, known as doping. Impurities provide electrons to the upper unoccupied energy bands of the semiconductor, transferred by lattice vibrations from foreign atoms to atoms of the pure substance [10]. This creates a p-i-n structure in which an intrinsic emitter layer is sandwiched between p-doped (top) and n-doped (bottom) transport layers. Electroluminescent devices constructed in this manner have demonstrated both high luminance and high efficiency at low operating voltages [11].

III-V semiconductor compounds are the preferred materials, particularly a heterostructure of InAs/GaAs (InAs QDs grown in a GaAs substrate), as this encourages the growth of defect-free QDs with uniform size distributions, boasting high-intensity photonic emissions at low temperatures [12]. A QD of this type grows in the {001} plane of the substrate (given as {xyz}, hence in the upwards direction), commonly experiencing in-plane anisotropy (elongation in one direction parallel to the surface) [13]. It forms a pyramidal shape, with the sides of the base oriented along the [100] and [010] directions (again given as [xyz], where z is the direction of growth). The side facets of the pyramid are close to the {011} plane (the diagonal plane), with the final height (width) typically 6 nm (12 nm). These QDs reside on a continuous wetting layer (WL) with a thickness in the monolayer regime [14].

1.3 Quantum dot properties

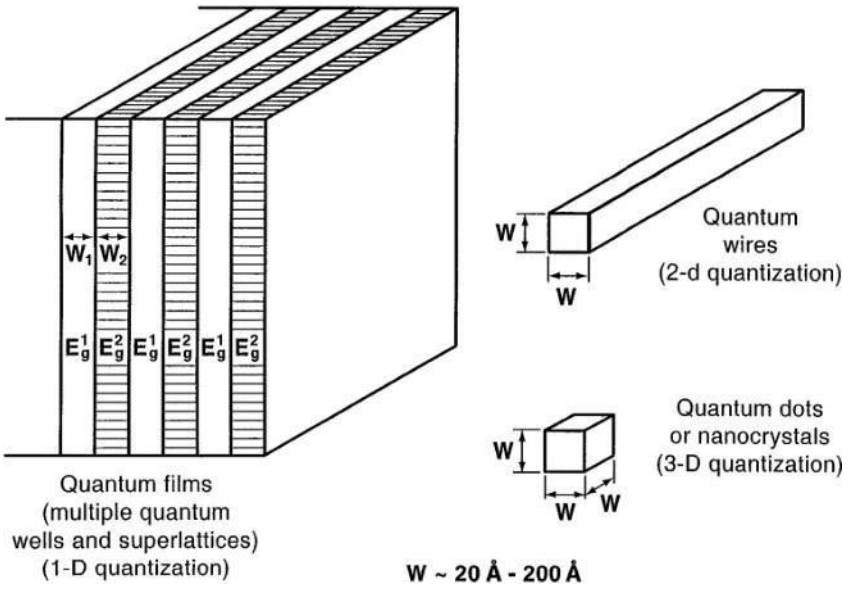

Figure 1.3. Quantization configurations for different quantum structures, with the dimensions given in Angstroms (10^{-10} m). E^1_g is the band gap energy for material one and E^2_g is the band gap energy for material two [15].

In 1977, the discovery that an excited atom emits a stream of single photons founded experimental quantum optics [16]. This field of research performs photoluminescence (PL) on QDs, whereby a laser excites the discrete, atom-like energy levels within a QD. The laser excitation of a QD initiates optical transitions between excited and ground states, generating single photons which are collected by optical fibres for spectral analysis [17]. A QD has a different quantization configuration to other quantum structures, impacting the relaxation dynamics of photogenerated charge carriers within the QD (Figure 1.3). A quantum film is formed by growing layers of semiconductor materials with different band

gaps and sandwiching them together. Semiconductors have a fundamental threshold energy for the absorption of a photon, known as the band gap energy (E_g). If a photon has an energy lower than the band gap of the semiconductor material, it cannot be absorbed. The smaller band gap material forms a quantum well (QW), with the larger band gap material on either side acting as potential barriers. This enforces carrier confinement in one dimension. A quantum wire can be constructed using selective deposition growth [18], resulting in a thin strand of semiconductor material which enforces carrier confinement in two dimensions. Predictably, a QD enforces carrier confinement in three dimensions. This intense confinement of carriers is advantageous as it dramatically alters the relaxation dynamics of the quantum system (reducing hot-carrier cooling rates and impact ionization rates), contingent upon the potential barriers enclosing a space that is smaller than the de Broglie wavelength of the carrier [15].

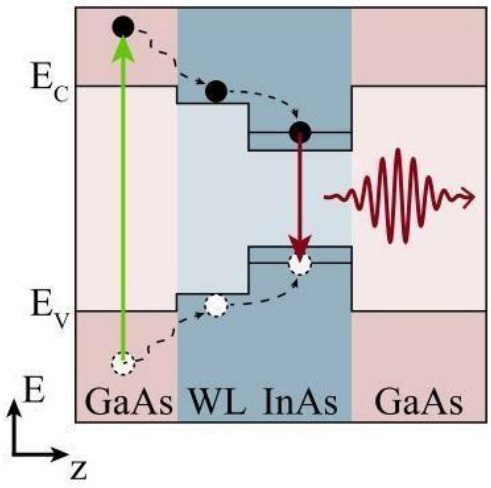

Figure 1.4. Energy levels of a GaAs membrane with an embedded InAs QD, where E_c is the energy of the conduction band, E_v is the energy of the valence band, and WL is the wetting layer [19].

The nature of spontaneous emission (SE) of photons from a QD is determined by its band structure, comprised of a valence band and a conduction band, the latter at a higher energy (Figure 1.4). An electron is excited from the valence band to the conduction band through above band illumination, subsequently undergoes fast, non-radiative decay, then recombines with the hole in the valence band, emitting a photon. The typical SE wavelength of the GaAs substrate is 830-850 nm. For the InAs QD, the SE wavelength is considerably longer at 900-950 nm. Both wavelength ranges fall into the near infrared category of electromagnetic radiation [19]. Noticeably, the QDs are situated inside a WL, which has an energy between that of the GaAs membrane and the InAs QD. Therefore, the two-dimensional wetting-layer states and the localized QD states form an electronically coupled system, whereby the carrier distribution in the system is mediated by the WL [20].

Name	Quantum State	Spin State
Bright Exciton 1	Y_b	$(1/\sqrt{2}) \cdot (\Uparrow\downarrow + \Downarrow\uparrow)$
Bright Exciton 2	X_b	$(1/\sqrt{2}) \cdot (\Uparrow\downarrow - \Downarrow\uparrow)$
Dark Exciton 1	Y_d	$(1/\sqrt{2}) \cdot (\Uparrow\uparrow + \Downarrow\downarrow)$
Dark Exciton 2	X_d	$(1/\sqrt{2}) \cdot (\Uparrow\uparrow - \Downarrow\downarrow)$
Electron	g^-	$u_c \cdot \alpha_c$
Hole	g^+	$u_v^* \cdot \alpha_v^*$
Ground State	G	N/A

Table 1.1. Confined states of a QD. ↑ (↓) *is the positive(negative) electron pseudo-spin state and* ⇑ (U) *is the positive(negative) hole pseudo-spin state, given in the z-basis (along the growth direction).* u_c *is the Bloch function of the conduction band.* α_c *is the spin state of the conduction band.* u_v** is the complex conjugate of the Bloch function of the valence band.* α_v** is the complex conjugate of the spin state of the valence band* [21].

Optical transitions in a QD are controlled by a quasiparticle known as the exciton, an electron-hole pair bound by the attractive Coulomb interaction [22]. For a given QD, the optically active states are always excitonic, hinted by the presence of fine-structure splitting. The Coulomb force creates an exchange interaction, splitting the four excitonic states into two doublets, separated by bright-dark energy splitting (Table 1.1). The X (Y) bright exciton state may decay to the ground state by emission of a vertically (horizontally)-

polarized photon. Spin-flip processes may transpire between the bright and dark states, which are slower than radiative decay. Non-radiative decay may also occur [21].

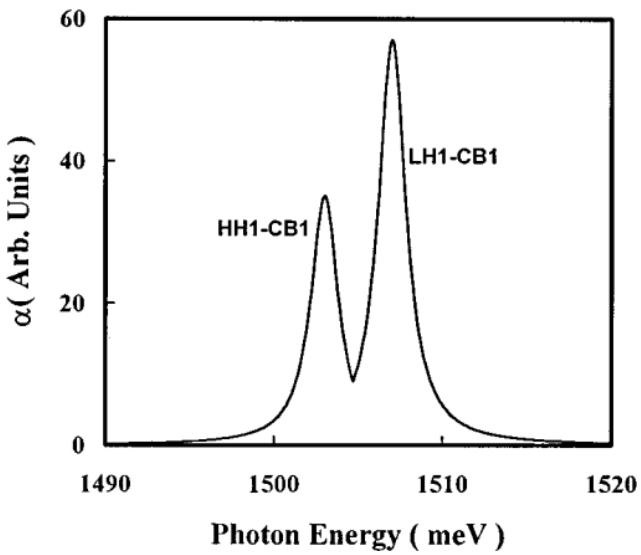

Figure 1.5. Theoretical absorption spectra of an InAs QD in a GaAs substrate, where HH1, LH1, and CB1 are the first energy levels of the heavy-hole band, light-hole band, and conduction band respectively [23].

The band structure of a QD is calculated by a collection of Hamiltonian equations, each representing the energy of a quasiparticle involved in optical transitions. Bulk InAs (QD material) and bulk GaAs (substrate material) have different effective masses which must be considered when calculating the Hamiltonians. Furthermore, the valence band contains heavy-hole (HH) subbands and light-hole (LH) subbands, with the former possessing a larger effective mass than the latter. The theory predicts a higher photon energy for the exciton transition between the first LH band and the first conduction band, than for the exciton transition between the first HH band and the first conduction band (Figure 1.5)

[23]. This agrees with the experimental data gathered by performing PL and PLE (photoluminescence excitation) of InAs/GaAs QDs, the former determining the HH spectra and the latter determining the LH spectra [24].

The temperature of the substrate has a strong impact on the properties of the QDs contained within. The homogeneous linewidth is the full width at half maximum (FWHM) of a QD's photonic emission. Narrow QD linewidths are vital for quantum communication systems, as the photon coherence is inversely proportional to the linewidth, credited to the positive correlation between linewidth and phase noise for QD coherent comb lasers [25]. Rising temperatures will linearly increase the homogenous linewidth of a QD, at a rate of 0.5 μeV/K for an InGaAs QD. This is attributed to the temperature-dependent interactions between the electronic states and the lattice vibrational modes (known as phonons) [26]. Just as light can be quantized as photons, acoustical waves (formed by heat oscillations) can be quantized as phonons [27]. Electron-phonon interactions contribute to the excitonic dephasing rate (the decay rate of the excitonic polarization), which in turn contributes to the homogenous linewidth of a QD. The longitudinal decay constant of the excitonic dephasing rate arises from phonon-assisted transitions between excitonic states. The electron-phonon interaction can then be represented by a Hamiltonian, containing a term that describes the adiabatic fluctuation of the excitonic energy level. This provides a lower limit for the linewidth of a QD [28].

An attractive property of the QD is its fast radiative carrier recombination rate, with the decay time from the excited state to the ground state determining the lifetime of the QD. This is inversely proportional to the modal gain of QD lasers, so short lifetimes are valuable. Determined by time-resolved PL, QD lifetimes have been shown to drastically

increase with rising temperatures (1.0 ns (80 K) to 5.5 ns (300 K) for InGaAs QDs), due to the thermal population of sub-WL continuum states within the system [29].

Because of linewidth broadening and lifetime lengthening, it is crucial to conduct PL experiments at low temperatures for accurate analysis of QD properties. This can be achieved by placing the sample in a liquid helium cryostat, cooling the QDs to temperatures as low as 4 K.

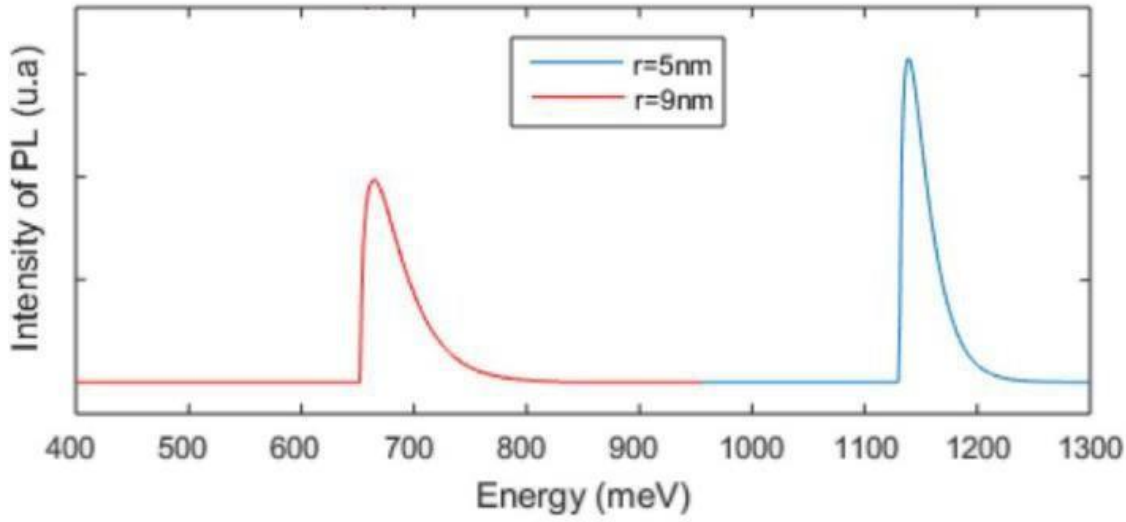

Figure 1.6. Photoluminescence spectra of InAs/GaAs QDs as a function of photon energy. r is the radius of the QD [30].

Depending on the size of the QD, the electron-hole pair states are modified by the strong, intermediate, or weak confinement regime. The strong confinement regime restricts the motion of an exciton state, due to both the reduced Coulomb binding energy and the high confinement potential. The weak confinement regime facilitates a correlated electron/hole motion, with the Coulomb attraction between electrons and holes generating bound exciton states. The intermediate confinement regime describes QDs with a more elliptical shape:

electron-hole pair states in the minor axis experience the strong confinement regime, whereas electron-hole pair states in the major axis experience the weak confinement regime [31]. InAs/GaAs QDs operate in the strong confinement regime, as the size of the QDs are smaller than the exciton Bohr radius (the distance between the electron and the hole in an electron-hole pair). Furthermore, InAs/GaAs QDs demonstrate strong size-dependence on the intensity, broadness, and energy of photonic emissions (Figure 1.6) [30].

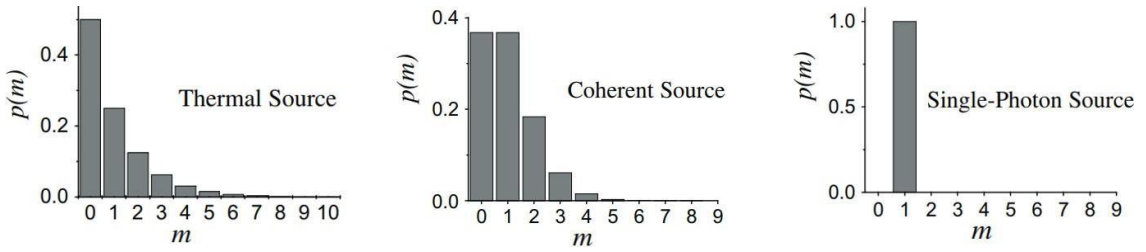

Figure 1.7. Probability distributions of the number of photons generated by different light sources, where the average number of photons is one [32].

To better understand how QDs emit photons, a comparison should be made between different types of light sources (Figure 1.7). Thermal light, emitted by a black body or a lamp, is comprised of numerous independent emitters, producing a superposition of many incoherent waves. The Bose-Einstein statistics of black-body radiation creates field fluctuations, resulting in the state with zero photons having the highest probability of occupation. Coherent light, emitted by a stable laser, has constant amplitude and constant phase: it is in a quasi-classical state, whereby the number of photons experiences Poissonian fluctuation. Squeezed light, emitted by a QD, delivers a regular stream of photons at regular time intervals. This is because a QD has a two-level system. After

emission of a single photon, the QD is in the ground state. For a second photon to be emitted, a new excitation-emission cycle must be carried out, requiring a time delay. Hence, the photon number fluctuation is sub-Poissonian, creating a source of single photons [32].

1.4 Deterministic positioning

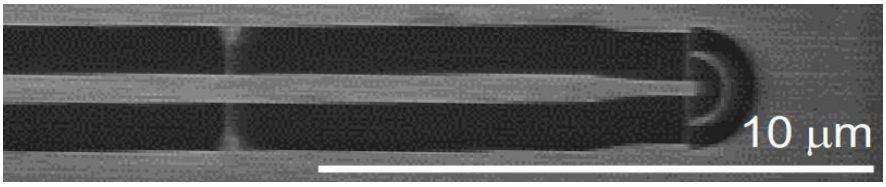

Figure 1.8. Scanning electron micrograph (SEM) of a GaAs nanobeam waveguide (NBWG) with a circular grating outcoupler [33].

The photonic devices investigated and applied in this thesis are: nanobeam waveguides, circular grating outcouplers, directional couplers, and multimode interferometers. Nanobeam waveguides direct light into appropriate channels with minimal propagation loss, by total internal reflection induced by the high refractive index difference between the waveguide material and the cladding material. Circular grating outcouplers scatter incident light in controlled directions for the purpose of on/off-chip light transfer, utilising refraction and constructive/destructive interference induced by alternating rings of materials with different refractive indices. Directional couplers are nanophotonic beamsplitters, whereby two parallel nanobeam waveguides enable light transfer to the adjacent waveguide through overlap of evanescent modes. Multimode interferometers are nanophotonic beamsplitters that direct light from a narrow single-mode waveguide into a much wider multimode waveguide, the latter inducing constructive/destructive interference which evenly splits the light into two output waveguides.

A shortcoming of heteroepitaxial growth is the randomness of the QD position within the substrate. A low quantum yield will be unavoidable if there is no prior information regarding both the spectral and the spatial properties of the QDs. For photon generation that can be used effectively in communications, QDs must be positioned within photonic devices. Such a device is the GaAs nanobeam waveguide (NBWG, Figure 1.8), with this material chosen due to its high refractive index in comparison with air (n_{GaAs} = 3.4, n_{air} = 1), ensuring efficient guiding of light with minimal losses. The QD can be excited by an overhead laser, inducing SE of single photons. The photons propagate through the waveguide to the outcoupler (a circular grating of GaAs and air), refracting upwards into an optical fibre which is coupled to a spectrometer for spectral analysis. An InGaAs QD contained within a GaAs NBWG can generate a high-purity source of indistinguishable single photons, with a quasi-resonant excitation experiment finding a photon purity above 99%, and a photon indistinguishability of over 90% [33].

NBWGs are fabricated by electron-beam lithography (EBL), patterning devices with a beam of electrons at high energy. Sub 10 nm precision has been demonstrated for isolated features. EBL is favourable to other patterning methods, such as scanning probe lithography techniques (scanning tunnelling microscopy/atomic force microscopy), due to its high resolution and fast writing speed [34].

1.5 Tuning techniques

For an integrated system of QDs to be scalable, spectral matching between QDs must be performed. meaning that QDs with the same emission wavelength must be paired. The difficulty of this depends on both the homogeneous linewidth and the inhomogeneous

linewidth of the QDs. The homogeneous linewidth is the natural linewidth of a QD, taking a Lorentzian shape, and broadening from surface-related charge separation or polarization effects. The inhomogeneous linewidth is the contribution to the linewidth from many QDs, taking a Gaussian shape, with its broadening dependent on the size distribution of the QDs [35]. InGaAs QDs have a homogeneous linewidth of approximately 1 μeV, but an inhomogeneous linewidth of tens of meV. As a result, the probability of finding N sets of QDs on a wafer with the same energy becomes vanishingly small with increasing N [36].

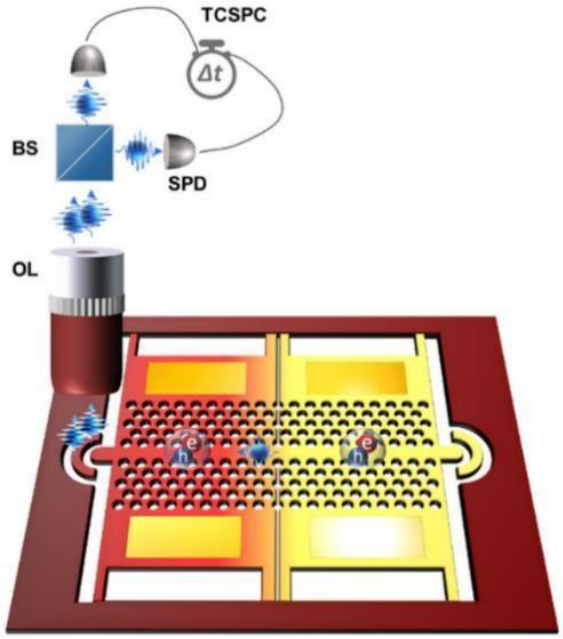

Figure 1.9. Laser tuning of two InAs/InP QDs in a photonic crystal waveguide, utilizing an objective lens (OL), a beamsplitter (BS), a single-photon detector (SPD), and time-correlated single-photon counting (TCSPC) [37].

To overcome this problem, QDs can be tuned into resonance. Such a technique is thermal tuning. Here, a photonic crystal waveguide containing two InAs/InP QDs is separated into two segments, such that each QD is contained within one of the segments, and the segments

are thermally isolated (Figure 1.9). The QDs are selected due to having close emission wavelengths, a difference of just 0.2 nm. A laser is directed onto a heating pad to heat one of the waveguide segments containing a QD. This heating gradually shifts the emission of a QD to a longer wavelength (known as a red shift), until it coincides with the emission wavelength of the other QD. There are two disadvantages to thermal tuning. Firstly, thermal tuning has a narrow spectral range, meaning that QDs with emissions wavelengths that are far apart cannot be tuned. Secondly, thermal tuning heats up the QDs, inducing linewidth broadening which degrades the quality of photonic emissions [37].

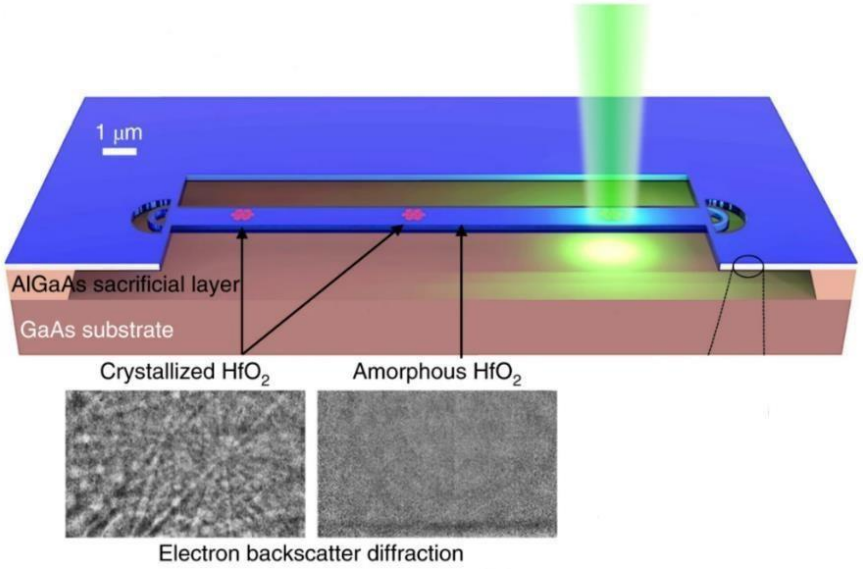

Figure 1.10. Laser-induced strain tuning of a HfO_2 sheath on a GaAs waveguide for three-QD superradiance [36].

An alternative tuning method is strain tuning, which modifies the material in which the QD is embedded. This has been demonstrated for tuning three QDs together (Figure 1.10). A laser crystallizes a HfO_2 sheath on a GaAs waveguide, producing material compression which shifts the emission wavelength of the longer wavelength QD to a shorter wavelength

(known as a blue shift). The degree of crystallinity, the value of Young's modulus, and various geometrical factors define the magnitude of the strain-induced blue shift. Unfortunately, strain tuning is irreversible, as the process modifies the underlying electronic band structure of the QDs, making it a risky procedure for QD tuning [36].

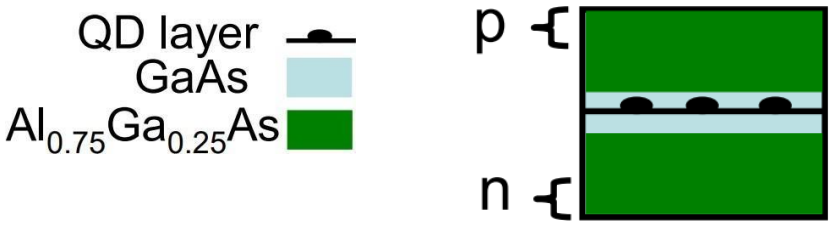

Figure 1.11. Quantum well for observation of the Stark effect in QDs, with the QDs situated in a GaAs layer between a layer of AlGaAs, where p is the positive side of the well and n is the negative side of the well [38].

Another tuning method is field tuning. Large electric fields can be applied to QD heterostructures to significantly change the emission wavelength of QDs, as demonstrated with InAs/GaAs QDs embedded in an AlGaAs/GaAs/AlGaAs QW (Figure 1.11). The AlGaAs layers are necessary to prevent the electrons from tunnelling out of the QD. As the electric field increases, exciton transitions encounter a quantum-confined Stark effect, with the energy defined by

$$E = E_0 + \beta F - \rho F^2 \qquad 1.3$$

where E_0 is the zero-field energy, β is the polarizability, F is the electric field, and ρ is the permanent dipole moment. Stark shifts of up to 25 meV can occur before QD luminescence is attenuated by carrier tunnelling [38].

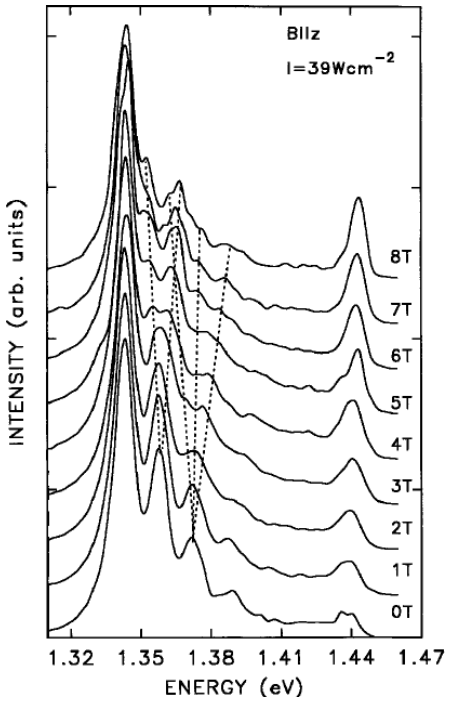

Figure 1.12. Magnetoluminescence spectra of self-organized InP islands on InGaAs/GaAs, with a magnetic field parallel to the growth direction. The dashed lines highlight the splitting that a line experiences as the field strength increases. I is the excitation intensity of the argon laser [39].

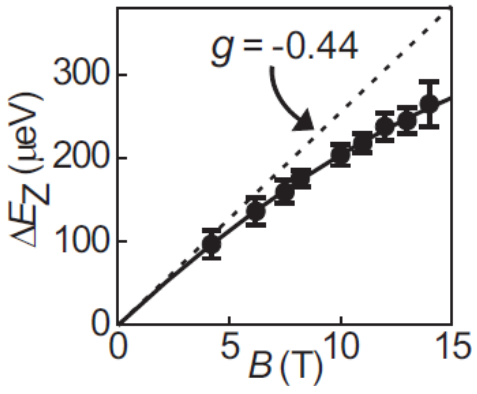

Figure 1.13. Extracted Zeeman splitting as a function of magnetic field strength for a one-electron QD in a GaAs/AlGaAs heterostructure. The dashed line represents the g-factor of bulk GaAs [40].

Alternatively, a magnetic field can perform the QD tuning. The magnetic field splits each QD emission line into a pair of lines (Figure 1.12). This is caused by Zeeman splitting of the interband transitions within a QD, which occurs only when a magnetic field is parallel to the growth direction of the QDs [39]. The magnitude of the splitting is then given by the Zeeman energy shift, written as

$$\Delta E_z = g\mu_B B \qquad 1.4$$

where g is the g-factor, μ_B is the Bohr magneton constant, and B is the magnetic field strength. Therefore, as the field strength increases, the spectral separation of every pair increases at a rate determined by the g-factor (Figure 1.13). The g-factor has four influences: the extension of the electron wavefunction into the AlGaAs region (lower g-factor than bulk GaAs), thermal nuclear polarization (attenuation of the effective magnetic field through hyperfine interactions), dynamic nuclear polarization (enhancement of the effective magnetic field through electron-nuclear flip-flop processes), and the nonparabolicity of the GaAs conduction band [40].

When attempting to resonantly tune two QDs of different emission wavelengths, the inner lines of each pair move closer together as the field strength increases. They eventually overlap, forming a single line on the spectra with an intensity equal to the sum of the two lines. Field tuning does not involve heating, and is reversible, making it the preferable option for spectral matching of QDs.

1.6 Interference

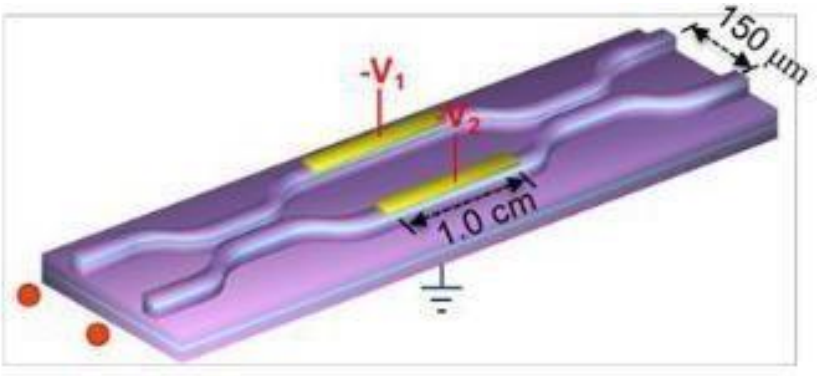

Figure 1.14. Schematic diagram of a Mach-Zehnder interferometer, made of GaAs ridge waveguides, with directional couplers at each end of the device and an electro-optic phase shifter in the centre of the device. V_1 and V_2 are the applied voltages. [41].

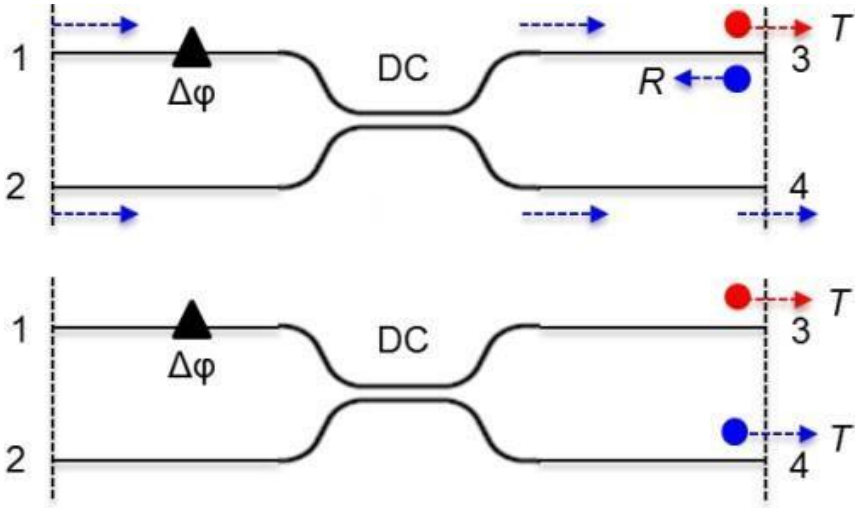

Figure 1.15. Photon pairs sent through a beamsplitter for quantum interference. Δφ is the phase shifter, DC is the directional coupler, T is a transmitted photon, and R is a reflected photon [41].

Photonic devices can be constructed for both classical interference and quantum interference. A combination of waveguide-based phase shifters and beamsplitters can divide/recombine optical modes of light in what is known as a Mach-Zehnder interferometer (Figure 1.14). A voltage induces a phase shift, creating output-power oscillations in the form of sinusoidal curves, known as classical interference fringes [41]. To measure quantum interference, indistinguishable photon pairs are sent through the interferometer, one in each input waveguide (Figure 1.15). Photon pairs have a probability of being detected at the same output waveguide (bunching), or different output waveguides (antibunching). A photon coincidence is a pair of photons simultaneously detected at a waveguide output. Quantum interference is determined by recording the number of photon coincidences at various time delays, controlled by a phase shifter [41].

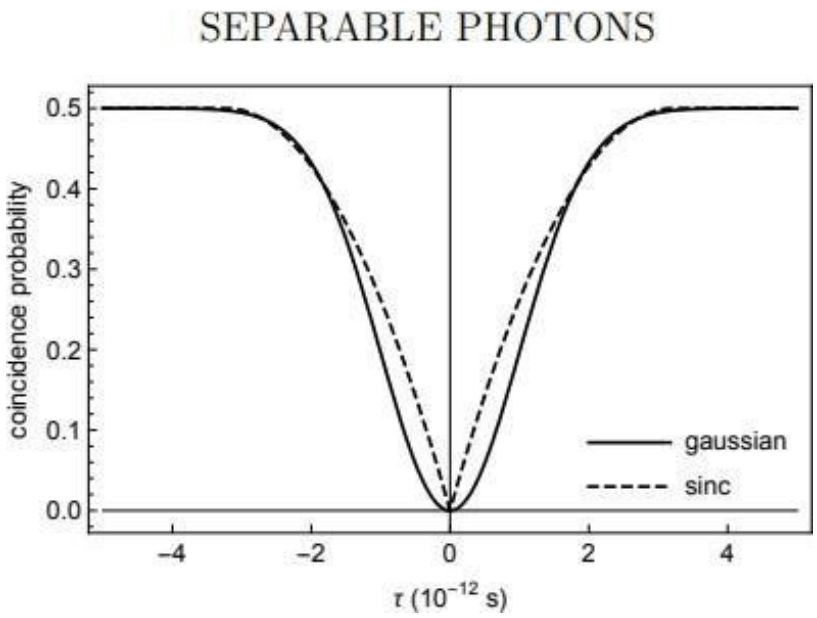

Figure 1.16. The coincidence probability for a pair of separable photons (photons with different spectral amplitude profiles) as a function of time delay [42].

Quantum interference of a photon pair is characterised by the Hong-Ou-Mandel curve, which can take a Gaussian or sinc shape (Figure 1.16). This is dependent on the distinguishability, entanglement, and spectral amplitude profile of the photons. The visibility measures the degree of quantum interference, a test of the photon purity, given by

$$V = \frac{N_{max} - N_{min}}{N_{max}} \qquad 1.5$$

where N_{max} is the maximum number of coincidences, and N_{min} is the minimum number of coincidences. For classical interference, the visibility is instead calculated by the maximum and the minimum output power. Perfect visibility would give $V = 1$, therefore $V < 1$ is expected experimentally. The aim is to produce interference fringes which are well-balanced with high visibility [42].

1.7 Superradiance

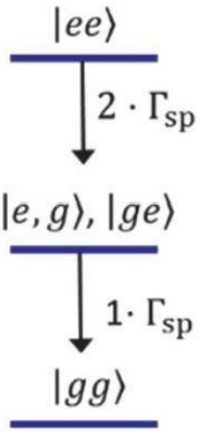

Figure 1.17. Level structure for two non-identical QDs. e is the excited state of a QD, g is the ground state of a QD, and Γ_{sp} is the SE rate of a single QD [37].

When two or more QDs are tuned into resonance, cooperative emission (superradiance) may be observed, whereby the QDs emit photons collectively at a faster rate than they would otherwise do individually. Multiple QD superradiance could be used to create chip-integrated photonic structures which exhibit long-range quantum interactions [37]. Super radiance can be difficult to measure due to coherent dipole-dipole interactions, but when QDs are coupled inside a NBWG, the super-radiant emission propagates within the guided modes rather than into free space [43].

If two QDs emit photons at a different wavelength, the photons are distinguishable, so the QDs are non-identical. A pair of non-identical QDs may be visualized as a level structure (Figure 1.17). First, the system decays from the excited state to the mixed state. Then, the system decays from the mixed state to the ground state with the SE rate of a single QD.

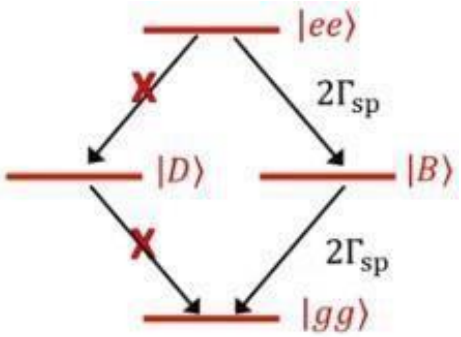

Figure 1.18. Level structure for two identical QDs [37].

If two QDs emit photons at the same wavelength, the photons are indistinguishable, so the QDs are identical (Figure 1.18). During the deexcitation process, there is a statistical mixture of ground states and excited states, described by the Dicke States, written as

$$|B\rangle = \left(|eg\rangle + e^{ikL}|ge\rangle\right)/\sqrt{2} \qquad 1.6$$

for the bright state, and

$$|D\rangle = \left(|eg\rangle - e^{ikL}|ge\rangle\right)/\sqrt{2} \qquad 1.7$$

for the dark state. In Eq. 1.6 and Eq. 1.7, *e* is the excited state, *g* is the ground state, *k* is the waveguide propagation constant, and *L* is the distance between the QDs. These states represent an entangled superposition of two QDs. For the dark state, the matrix element is antisymmetric and is therefore equal to zero. No transitions can occur through this route, so it is known as the subradiant state. For the bright state, the matrix element is symmetric, and is therefore nonzero. Consequently, the two QD system behaves as a single two-level system, whereby the system decays from the bright state to the ground state with double the SE rate of a single QD, a signature of superradiant emission [44].

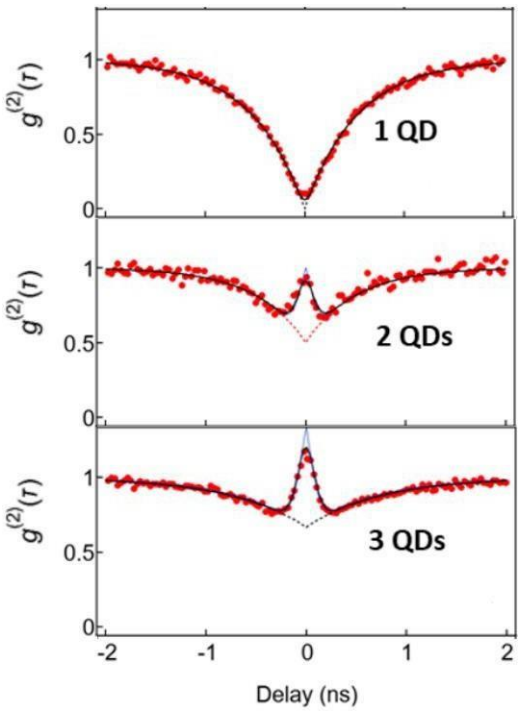

Figure 1.19. Second-order photon correlation (g2) of coupled QDs in a nanophotonic waveguide. (One QD, two coupled QDs, and three coupled QDs) [36].

Superradiance can be quantified by second-order photon correlation (g2), a statistical measure of the correlation of intensities for two different photon detectors (Figure 1.19). A single QD can only emit one photon per excitation cycle, generating photon anti-bunching, producing a dip at a time delay of zero. A resonantly coupled QD system can generate multiple photons per excitation cycle, generating photon bunching, producing a peak at a time delay of zero.

The g2 can be expressed as a normalized function of the delay between a count on one photon detector and a count on the other, written as

$$g^{(2)}(t) = \left[1 - \frac{1}{N} e^{-\gamma\tau}\right] + \frac{1}{N^2} e^{-2\Gamma\tau - 4\pi^2\sigma^2\tau^2} \sum_{i \neq j} \cos(\delta_{ij}\tau) \qquad 1.8$$

where: N is the number of coupled QDs, γ is the radiative emission rate, $\delta_{ij}$is the detuning between the QDs, Γ is the contribution to the QD linewidth from the radiative emission rate plus the pure dephasing rate, and σ is the contribution to the linewidth from spectral diffusion. The pure dephasing rate describes how quickly phase coherence is lost due to elastic exciton-acoustic phonon interactions [45]. Spectral diffusion is the broadening of the QD emission line, caused by charge trapping processes from photoionization or thermal ionization of excitons [46].

The first term of Eq. 1.8 is the independent contribution from each QD as distinguishable emitters, responsible for producing the antibunching dip of the g2. The second term of Eq. 1.8 is the interference of the QDs, responsible for producing the superposition of the coherent bunching peak with the antibunching dip. Setting $\tau = 0$, the height of the coherent bunching peak is obtained. For N = 1, $g2(\tau = 0) = 0$, as the sum in the second term equals zero, because the condition $i \neq j$ is not satisfied for a single emitter. For N = 2,

g2(τ = 0) = 1, as the sum in the second term is 2P2 = 2 for the two permutations of δ_{ij}. For N = 3, g2(τ = 0) = 4/3, as the sum in the second term is 3P2 = 6, and so on [36].

1.8 Chirality

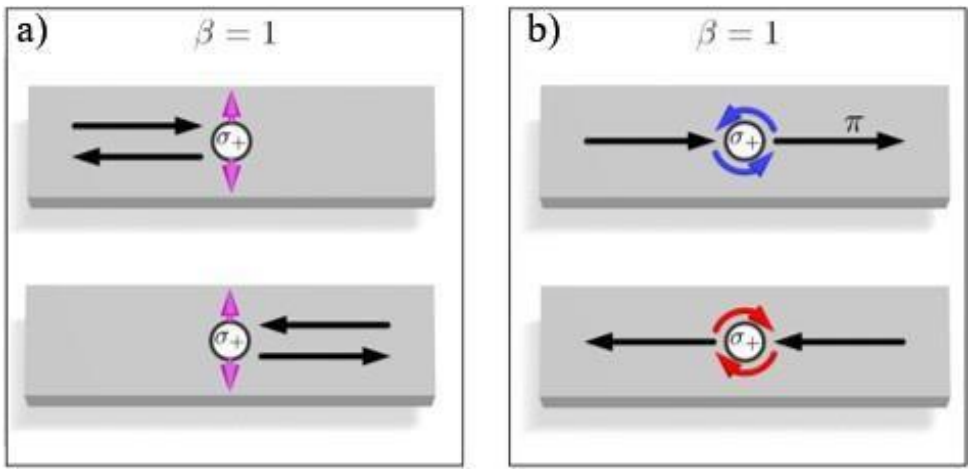

Figure 1.20. Lossless photon interaction with a waveguide embedded QD. a) symmetric coupling. b) chiral coupling. β is the coupling efficiency. σ_+ is the positive spin state. π represents a 180^o phase-shift [47].

The chirality of a QD in a waveguide determines the directionality of its emission. The efficiency of coupling to the photonic waveguide mode in a particular direction is given by the beta factor, written as

$$\beta_{L(R)} = \frac{\gamma_{L(R)}}{\gamma_L + \gamma_R + \Gamma} \qquad 1.9$$

where Γ is the decay rate for emission into free space and $\gamma_L(\gamma_R)$ is the energy constant of the left (right) propagating photon. A lossless system would give $\beta = \beta_L + \beta_R = 1$ (Figure

1.20). For lossless symmetric coupling with a photon propagating in the rightward direction, $\beta_R = 0$, as the QD becomes a perfectly reflecting mirror. For lossless chiral coupling with a photon propagating in the rightward direction, $\beta_R = 1$, as the QD becomes fully transparent, imparting a π phase shift on the photon.

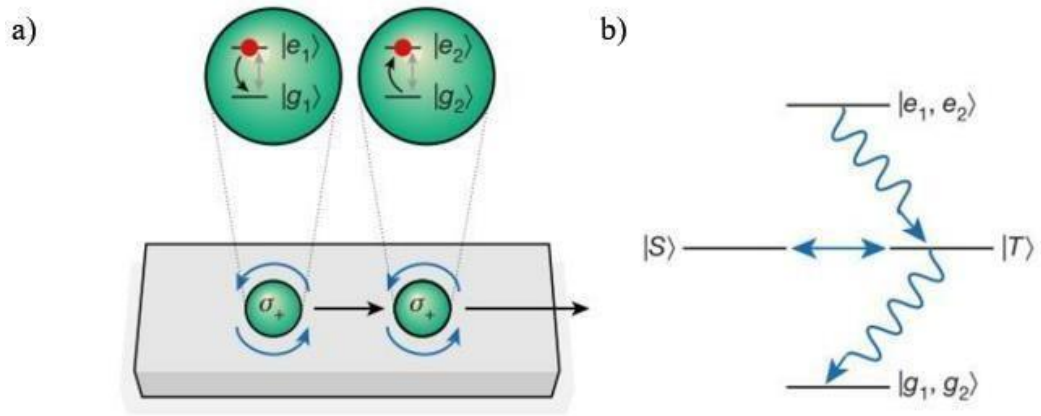

Figure 1.21. Modified superradiance. a) Two chirally coupled QDs in a waveguide, exhibiting unidirectional emission, showing the level structure for each QD. b) Level structure of the coupled QD system. S is the singlet state and T is the triplet state [47].

Positioning two QDs closer to the sides of a waveguide can enable superradiance via chiral coupling, whereby the photon to QD interaction becomes non-reciprocal, generating a cascaded quantum system without information back-flow (Figure 1.21). The left QD begins in the excited state, emits a photon by deexcitation, exciting the right QD from the ground state to the excited state, thus repeating the process for a multiple QD system. This type of chiral QD coupling is mediated by the interaction between the subradiant singlet state and the superradiant triplet state [47]. If the left QD is continuously excited by a laser, equilibrium is reached between pumping and emitting. This is superior to non-chiral

coupling, as the maximum generated spontaneous entanglement (concurrence) can be enhanced by a further 50%, with a weaker dependence on the proximity of the QDs [48].

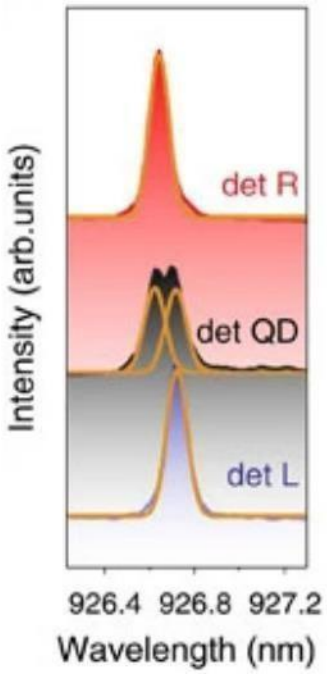

Figure 1.22. Photoluminescence spectra of an InGaAs QD with a high chiral contrast in a NBWG, subjected to a magnetic field of strength 1 T. Collection from the right outcoupler (det R), from the QD (det QD), and from the left outcoupler (det L) [49].

The chirality of a QD in a NBWG can be quantified by measuring its chiral contrast. This is revealed by applying a magnetic field to the QD, splitting the emission line into a pair of lines, as explained in Section 1.5. Emission is collected from the left outcoupler, then directly from the QD, then the right outcoupler (Figure 1.22). When collecting emission directly from the QD, there are two lines corresponding to the two spin states of the QD (spin up/spin down). The emitted photons are left-circularly polarized and right-circularly polarized (σ_+/σ_-). Collecting emission from either outcoupler, it is revealed that only the

shorter wavelength line is visible from the right outcoupler, and only the longer wavelength line is visible from the left outcoupler. Therefore, this QD is demonstrating perfect chiral contrast. It is likely that a QD will not be perfectly chiral, whereby the left outcoupler will show a taller line next to a shorter line, and the right outcoupler will show the reverse. In this case, the chiral contrast at each outcoupler is calculated as

$$C = (I_{\sigma+} - I_{\sigma-})/(I_{\sigma+} + I_{\sigma-}) \quad 1.10$$

where $I_{\sigma+}$ is the intensity of the shorter wavelength line and $I_{\sigma-}$ is the intensity of the longer wavelength line. Then, the absolute average chiral contrast can be calculated as

$$C = (|C_{LEFT}| + |C_{RIGHT}|)/2 \quad 1.11$$

where C_{LEFT} is the chiral contrast at the left outcoupler and C_{RIGHT} is the chiral contrast at the right outcoupler [49].

2 Methodology

2.1 Theoretical techniques

2.1.1 Finite-difference time-domain simulation

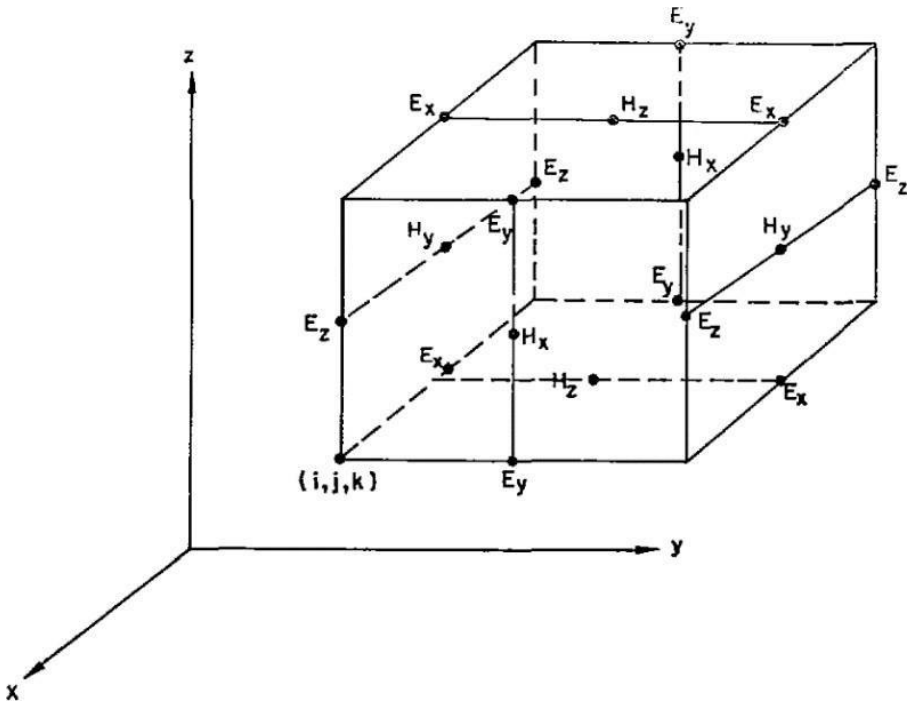

Figure 2.1. Yee grid of electric field components and magnetic field components [50].

A key theoretical technique for investigating photonic devices is finite-difference time-domain simulation (FDTD). By solving Maxwell's equations for electromagnetics, it can

model light propagation within dielectric materials. FDTD is well-tailored for electromagnetic simulations, appropriately handling pulsed, transient, and sinusoidal sources in the transverse electric or transverse magnetic modes [51].

FDTD was first introduced in 1966 by mathematician Kane Yee, with the aptly named "Yee grid": a cubic space-time mesh of electric field components (E) and magnetic field components (H), in the x, y, and z directions (Figure 2.1). The H-components are in the centre of the cube's faces, whilst the E-components are in the middle of the cube's edges, such that each H-component is surrounded by four E-components. The grid points are chosen to approximate the boundary conditions for a perfectly conducting surface, whereby both the normal component of the magnetic field and the tangential components of the electric field vanish. The length of this grid must be considerably smaller than the wavelength of the propagating light, such that the electromagnetic field changes only marginally over the volume of one grid [50].

In 1981, theoretician Gerrit Mur published work which enabled modern computational usage of FDTD. He developed highly absorbing boundary conditions for electromagnetic-field equations in both two and three dimensions. Through analysis of Yee's space grid methodology, the condition for stability in three dimensions is found to be

$$\delta t = \frac{\delta}{c_0\sqrt{3}} \qquad 2.1$$

where δt is the time increment, δ is the space increment, and c_0 is the speed of light in a vacuum. Abiding by this condition, the mesh is truncated in each coordinate direction: inside the boundary the total field is computed, whilst outside the boundary the scattered field is computed. Numerical results, in the form of radiation contour plots, confirm the

efficiency of the highly absorbing boundary conditions. The second-order and higher-order finite-difference approximations considerably reduce the reflectivity issues that hampered previous methods [52].

I use Ansys Lumerical FDTD to run simulations of photonic devices for the purpose of geometrical optimisation. A light source may be placed in a waveguide and detectors may be placed at various points within the photonic device to calculate light transmission at those points. These components function by creating tensors of material parameters at every grid point (conductivities, permeabilities, etc.), and calculating them for every time step [53]. Ansys Lumerical FDTD supports different types of FDTD. To collect results, I use 3D FDTD. However, if I am modelling a complex photonic device, I use 2.5D variational FDTD (known as varFDTD) to optimise the geometry, and then I use 3D FDTD to collect the final results. This is because varFDTD collapses a 3D geometry into a 2D set of effective indices, reducing the memory requirements of the simulations, to produce less accurate but faster results [54].

2.1.2 Curve fitting

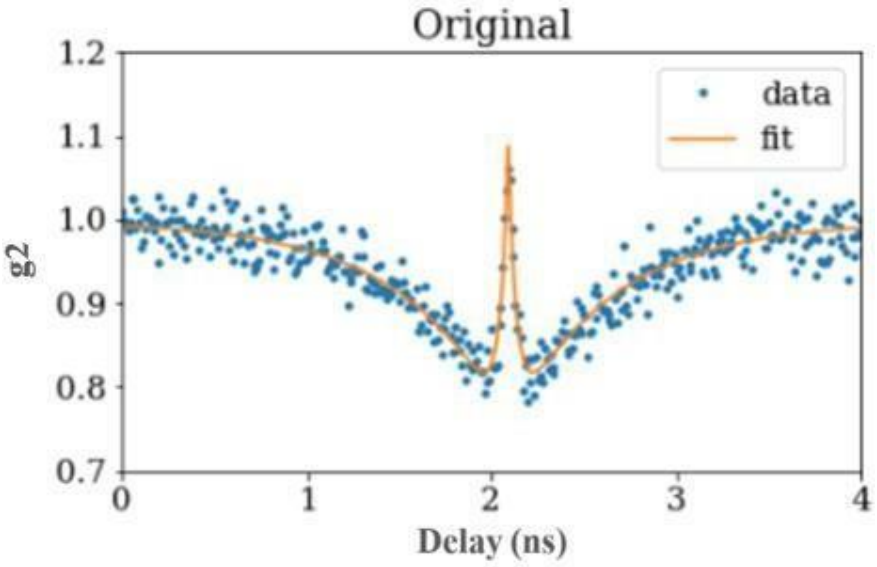

Figure 2.2. Curve fitted to g2 data in Python.

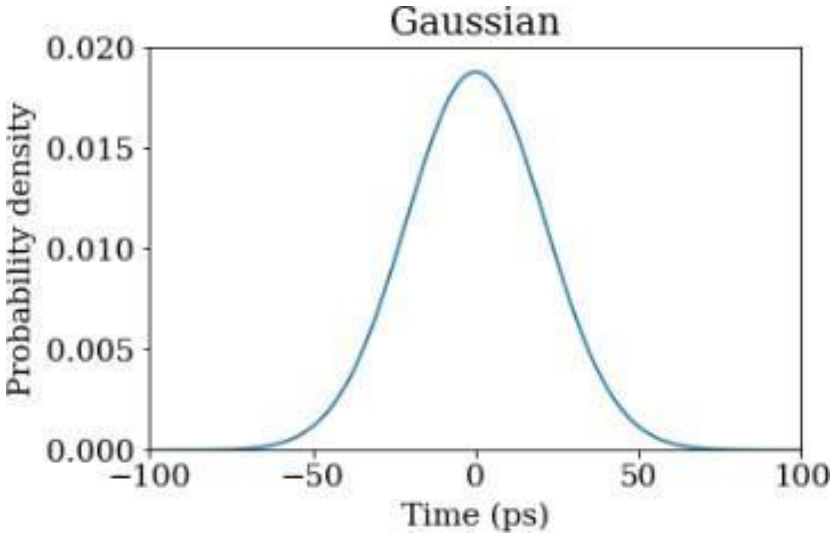

Figure 2.3. Gaussian curve, representing the time resolution of the detector.

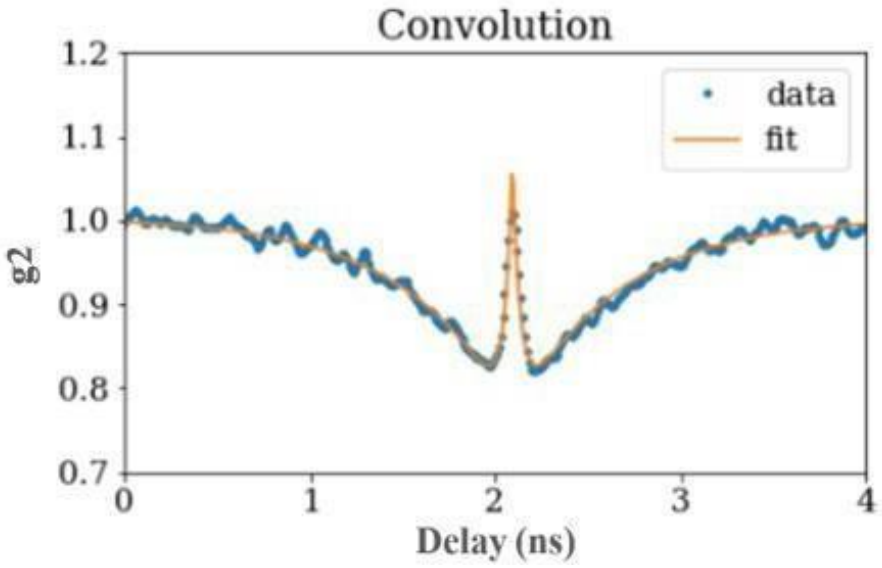

Figure 2.4. Convolution of the g2 data with the Gaussian.

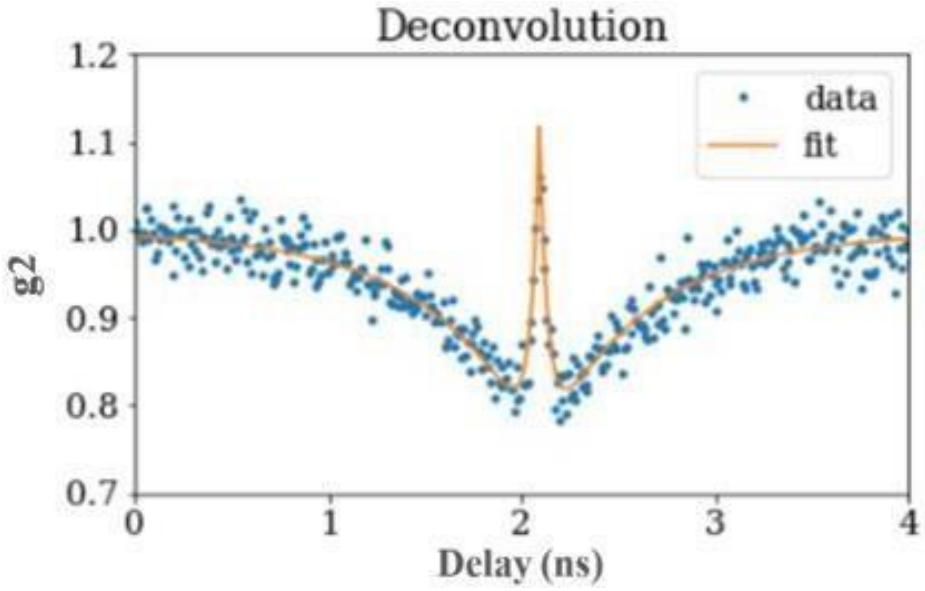

Figure 2.5. Deconvolved fit superimposed on the original data.

Within the programming language Python, the packages Numerical Python (NumPy) and Scientific Python (SciPy) are used to fit a curve to an experimentally obtained g2

measurement. First, the g2 function (Eq. 1.8) is written with eight parameters that can take any value, giving

$$a - b * \exp\left(-c * abs(t - t_0)\right) + j * exp(-k * abs(t - t_0) - l * (t - t)^2) * 2 * cos(m * abs(t - t_0)) \quad 2.2$$

where a is the shoulder height, b is the dip height, c is the dip width, j is the peak height, k is the peak width due to radiative emission plus pure dephasing, l is the peak width due to spectral diffusion, m is the oscillation strength, and t_0 is the x-axis translation.

00Next, the g2 data is imported, and a curve is fitted to this data (Figure 2.2). The least squares method determines the values of all eight parameters, minimizing the sum of the squared residuals (the differences between the y-values of the data and the y-values of the fitted curve) [55]. Finally, a deconvolution is performed, which is an attempt to undo the reduction of the peak height caused by the time resolution of the detector. This is executed in three steps. Step one: a Gaussian with a FWHM of 50 ps is generated (Figure 2.3), since this roughly simulates the time jitter of the photon detector (previous work has found the time jitter of this detector to approximate a 46 ps Gaussian [56]). Step two: the Gaussian is convolved with the original data to form the convoluted data, then a new curve is fitted to this data, giving the convolution fit (Figure 2.4). Step three: the deconvolution fit is calculated (Figure 2.5), where the new peak height parameter value is given by the following equation

$$j_{decon} = 2j_{og} - j_{con} \quad 2.3$$

where j_{decon} is the peak height parameter for the deconvolution fit, j_{og} is the peak height parameter for the original fit, and j_{con} is the peak height parameter for the convolution fit.

Post-fitting, the area of the coherent bunching peak can be extracted to compare the magnitude of superradiance across different measurements.

2.1.3 Quantum Toolbox in Python

To simulate the temporal dynamics of two QDs in a waveguide, I use a programming package known as the Quantum Toolbox in Python (QuTiP). This is an object-oriented open-source framework that can create arbitrary Hamiltonians from operators and states of a quantum object class, which can then be solved by a master equation [57]. This master equation can calculate the temporal change of each QD state: useful for investigating superradiance and subradiance generated by two-body systems.

The states of the QDs are defined, namely the basis states (excited/ground) and the superradiance states (bright/dark). The Hamiltonians are then defined: the Hamiltoninan of the system (H_S), the Hamiltonian of the reservoir (H_R), the interaction Hamiltonian between the system and its environment (H_I). These Hamiltonians combine to form the full time-dependent Hamiltonian (H_{total}). The collapse operators are then defined, providing the decay rates for each QD. The temporal change of each QD state is then solved by the Lindblad master equation, which can be simplified to

$$\partial_t \rho_t = L_t^{\dagger} \rho_t \qquad 2.4$$

where ρ_t is the density matrix and $L_t^{\dagger}$ is the Lindbladian super operator [58].

2.2 Experimental techniques

2.2.1 Micro-photoluminescence spectroscopy

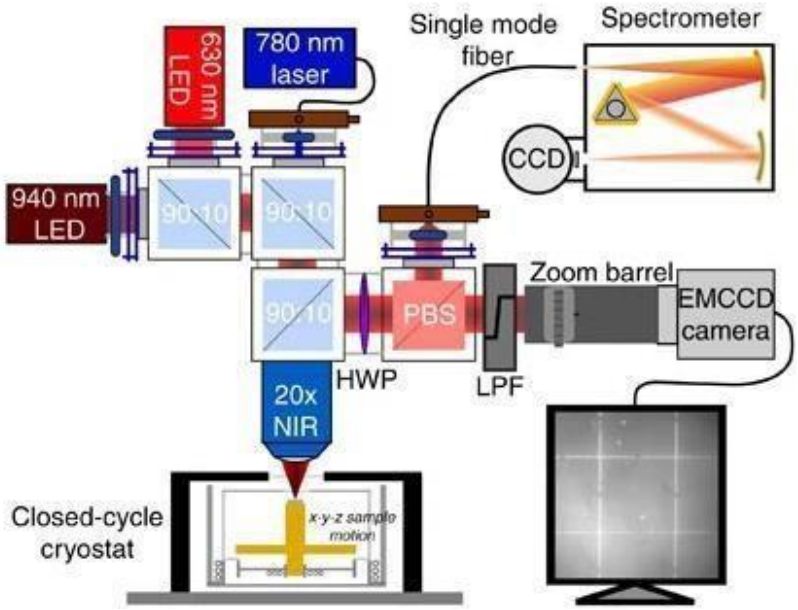

Figure 2.6. Illustration of a cryogenic photoluminescence imaging system with three different light sources. LED = light-emitting diode, NIR = near-infrared, HWP = half-wave plate, PBS = polarizing beamsplitter, LPF = low-pass filter, CCD = charge-coupled device, EMCCD = electron multiplying charge-coupled device [59].

Micro-photoluminescence spectroscopy (µ-PL) is a recurring technique in my experimental work. To describe µ-PL in one sentence: the wafer is probed by an excitation laser, generating SE from the QDs, creating a spectra of sharp emission lines, revealing the intensity and wavelength of the captured photons (Figure 2.6). The excitation energy can be resonant (matching the exciton transition energy), quasi-resonant (matching an excited

exciton state) or above-band (beyond the band gap energy of the QD) [21]. The μ-PL experiments featured in this thesis use above-band excitation. μ-PL can be used to find and record the positions of similar-energy QDs on a wafer, in a process known as QD registration. This permits the fabrication of NBWGs containing coupled QDs for superradiance experiments. This technique is appropriate for wafers with a low QD density, so the bright spots in the camera image are well-separated [60]. Etched alignment markers must be present on the wafer, typically in the form of crosses or parallel lines, to provide reliable reference points for QD coordinate determination.

As revealed in Section 1.3, spectroscopy must be performed at low temperatures. Consequently, the wafer is positioned in a vacuum cryostat, where a metal rod, cooled by liquid helium (known as a cold finger), reduces the temperature of the wafer to 4 K. The stage is moved either mechanically (for coarse adjustments) or piezoelectrically (for finer adjustments). Movement in x or y traverses the wafer, whilst movement in z brings the wafer into focus. A light-emitting diode (LED) powers the wafer, providing a longer wavelength for illumination of the GaAs alignment markers and a shorter wavelength for excitation of the InAs QDs. The LED power is increased until enough QDs are activated. A series of mirrors and beamsplitters direct SE into the appropriate channels. SE is captured by a camera, providing a fast exposure time (1 second) for searching, and a slow exposure time (10 seconds) for recording.

SE is guided through a single-mode optical fibre to a spectrometer for spectral analysis. It enters the slit of the polychromator, where it reflects off a toroidal (two-radii) mirror and is collected by a grating turret for diffraction. This spatially disperses the SE, where it reflects off a second toroidal mirror and is collected by the detector [61]. The grating turret

is blazed (jagged surface), with three different blazes: 600 lines/mm, 1200 lines/mm, and 1800 lines/mm. As the line density increases, the intensity of the spectra is attenuated but the accuracy of the spectra is improved. Hence 600 lines/mm is used for searching, and 1800 lines/mm is used for recording.

The detector is a PyLoN 100BR CCD (charge-coupled device) camera. It requires daily cooling to around 150 K by liquid nitrogen, eliminating dark current that could generate false counts, thus increasing the reliability of the spectral data. “100” refers to the array size of the CCD: 1340 x 100 pixels. Since the CCD provides spectral information rather than spatial information, the energy lies on a single axis, with the resolution given by the former dimension. “BR” refers to the sensor type B/I DD, which is a back-illuminated sensor with a deep depletion CCD. The deeper depletion region improves the efficiency of light collection in the near-infrared [62].

Preceding a μ-PL experiment, spatial-spectral calibration is performed, whereby the collection path is matched with the live-feed streamed by the camera. This is done by sending a laser through the collection path and drawing a circle around the resulting beam on the feed, synchronising the spectral data with the spatial data.

Post-spectroscopy, QD coordinates are determined using the programming language MATrix LABoratory (MATLAB). Within MATLAB, maximum likelihood estimation (MLE) is used, which fits a 2D Gaussian point-spread function (PSF) to the centre of the QD emission [63].

2.2.2 Hanbury Brown-Twiss interferometry

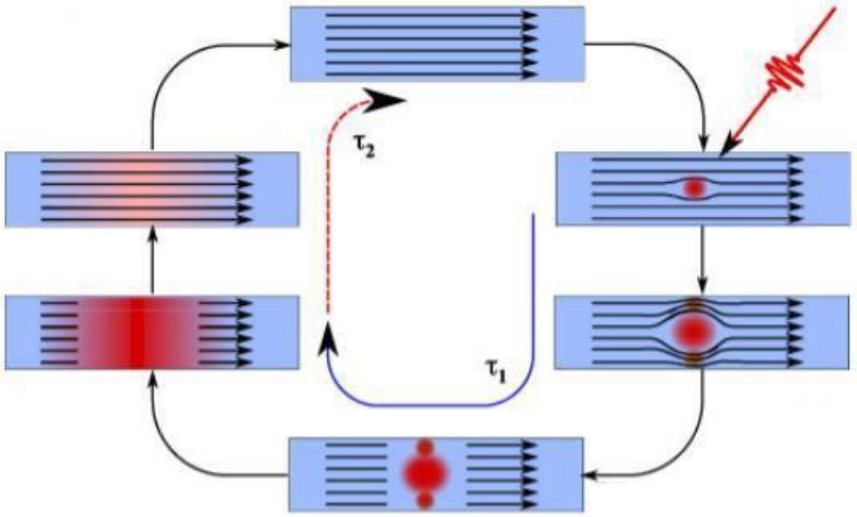

Figure 2.7. The detection cycle of a superconducting nanowire single-photon detector (SNSPD). The blue material is the nanowire, the black arrows show the current flow, and the red arrow is an incoming photon. τ_1, τ_2 are the contributions to the dead time of the system [64].

Hanbury Brown-Twiss interferometry (HBT) can be performed to assess the quality of superradiant emission from coupled QDs in NBWGs. This is a type of time-correlated single photon counting (TCSPC) for two channels of photons from the same output coupler of the photonic device, recording the g2 of the signal.

A two-channel superconducting nanowire single photon detector (SNSPD) is used to detect the photons, cooled to 4K with liquid helium (Figure 2.7). A photon is absorbed by the nanowire, creating a small resistive hotspot in the nanowire. The current is then forced to navigate around the hotspot, which increases the local current density surrounding it,

forming a resistive barrier as the superconducting critical current density is exceeded. Joule heating expands the barrier until current flow is blocked, dissipating the barrier, and the nanowire is now in its original state, ready to accept another photon. The period for this cycle is known as the dead time, as during this process, photons cannot be absorbed. The dead time can be as low as 30 ps [65].

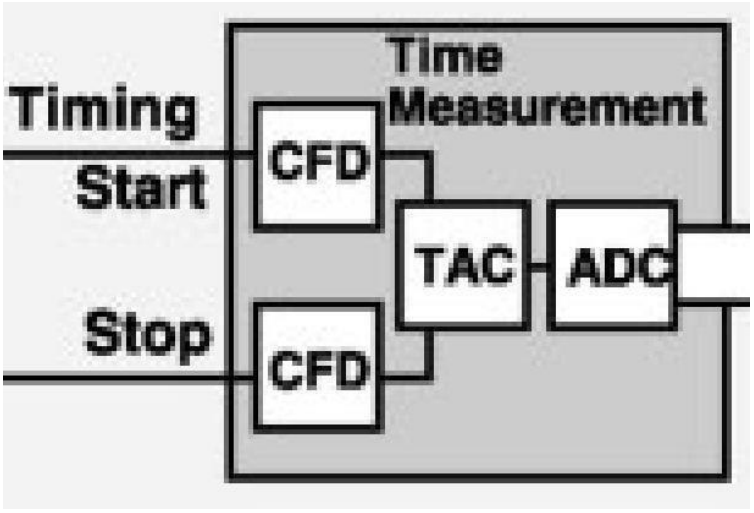

Figure 2.8. Principle of time-correlated single-photon counting (TCSPC), utilizing a pair of constant fraction discriminators (CFDs), a time-to-amplitude converter (TAC) and an analog-to-digital converter (ADC) [66].

TCSPC requires two signal pulses (Figure 2.8). This could be two channels of photons, or a single channel of photons with a reference voltage pulse. Signal pulses are received by a pair of constant fraction discriminators (CFDs) to find the centre of the pulses, which is the time point where the slope of the pulse is zero. Next, a time-to-amplitude converter (TAC) measures the difference in arrival time between the primary and the secondary pulses. Finally, the output is passed through the analog-to-digital converter (ADC), which converts

the output voltage into an address for the memory. Each start-stop cycle takes around 50 ps: the time resolution of the detector. Over time, the memory builds up, generating a histogram of the photon distribution [66].

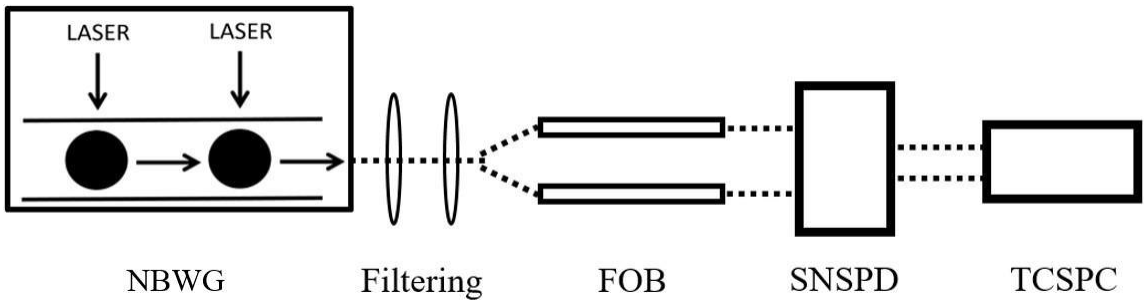

Figure 2.9. Diagram of Hanbury Brown-Twiss interferometry (HBT), where NBWG is a nanobeam waveguide containing two QDs, FOB is a fibre-optic splitter, SNSPD is a superconducting nanowire single-photon detector, and TCSPC is time-correlated single-photon counting. The dashed lines represent a stream of single photons.

I will now describe how HBT is used to measure superradiance from coupled QDs in a NBWG (Figure 2.9). The sample is placed inside a helium bath cryostat, cooling it down to 4 K. It is surrounded by a magnet that is built-in to the cryostat. Two continuous wave (CW), monochromatic lasers, of 808 nm wavelength, induce above-band excitation of the QDs, generating SE of single photons. The laser power is adjusted by a rotatable filter, so the weakest QD is at saturation intensity and the other QD matches this intensity. The saturation power is determined by the behaviour of the emission line on the spectra as the laser power is increased: once the intensity lowers and the line broadens, saturation power

is surpassed. Operating at saturation power ensures that the highest possible signal-to-noise ratio is obtained for TCSPC.

Magnetic field tuning of the QD pair is performed. The magnetic field is adjusted to ensure the lines are spectrally matched by minimising the linewidth of the resonance line. A pair of band-pass filters (0.5 nm) are used to filter out background emissions. The filtered signal is sent to a 1x2 fibre-optic splitter (FOB), then into a two-channel SNSPD linked to a monitor which displays the counts in each channel. The polarization of the FOB is adjusted to maximise the counts, then the output is measured by TCSPC over a period of approximately 5 hours.

2.2.3 Fabry-Pérot interferometry

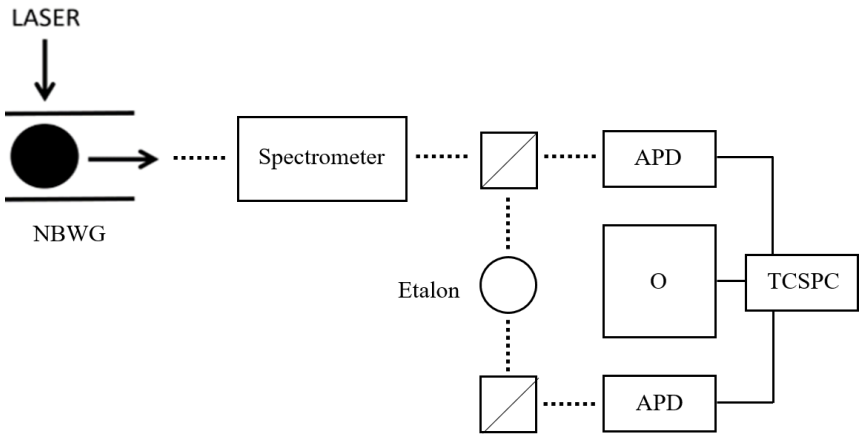

Figure 2.10. Diagram of Fabry-Pérot interferometry (FPI), where NBWG is a nanobeam waveguide containing one QD, APD is an avalanche photodiode, O is an oscilloscope, and TCSPC is time-correlated single-photon counting. The dashed lines represent a stream of single photons, the solid lines represent electrical connections and the squares containing diagonal lines are moveable mirrors.

When studying QDs, it is important to know their linewidths, particularly for tuning experiments, so the relative detuning of the QD emission lines can be determined. However, the spectrometer has a spectral resolution of roughly 13 pm [67], which is not precise enough for narrow-linewidth QDs. Instead, the linewidth can be determined using Fabry-Pérot interferometry (FPI), illustrated in Figure 2.10. A passive optical resonator (etalon), formed by placing two partially-reflective glass plates close together, can generate interference fringes from a QD signal, revealing the QD linewidth. FPI can achieve a spectral resolution as low as 0.5 pm [68]. An 808 nm CW laser excites the QD, with the SE sent to the spectrometer. It exits the spectrometer, with the spectrometer's filter sweeping through a narrow wavelength range around the recorded central emission wavelength of the QD. The emission is coupled to an avalanche photodiode (APD) by a multimode optical fibre, converting it to an electrical signal. TCSPC finds its precise wavelength, where the primary input is the APD output and the secondary input is a reference voltage pulse from an oscilloscope. After this step, the spectrometer is set to filter out all wavelengths besides the chosen wavelength, sending the emission through an etalon. This generates light interference, with the output collected by a second APD for TCSPC. Several interference fringes are formed, with equal separation along a time axis, and are then fitted with Gaussian curves, revealing the Gaussian width. The FWHM in milliseconds is then

$$FWHM\ (ms) = w\sqrt{ln4} \tag{2.5}$$

where w is the Gaussian width. The FWHM in gigahertz is then

$$FWHM\ (GHz) = \frac{10n * FWHM(ms)}{t_f - t_i} \tag{2.6}$$

where n is the number of fringes, t_f is the time value of the final fringe, and t_i is the time value of the initial fringe. Both the mean and the standard deviation of the FWHM in gigahertz is calculated, then the values are inputted to an online bandwidth calculator [69]. This converts the FWHM into picometres, obtaining the linewidth of the QD.

3 Circular Grating Outcouplers for Efficient Light Collection

3.1 Outcoupler simulation

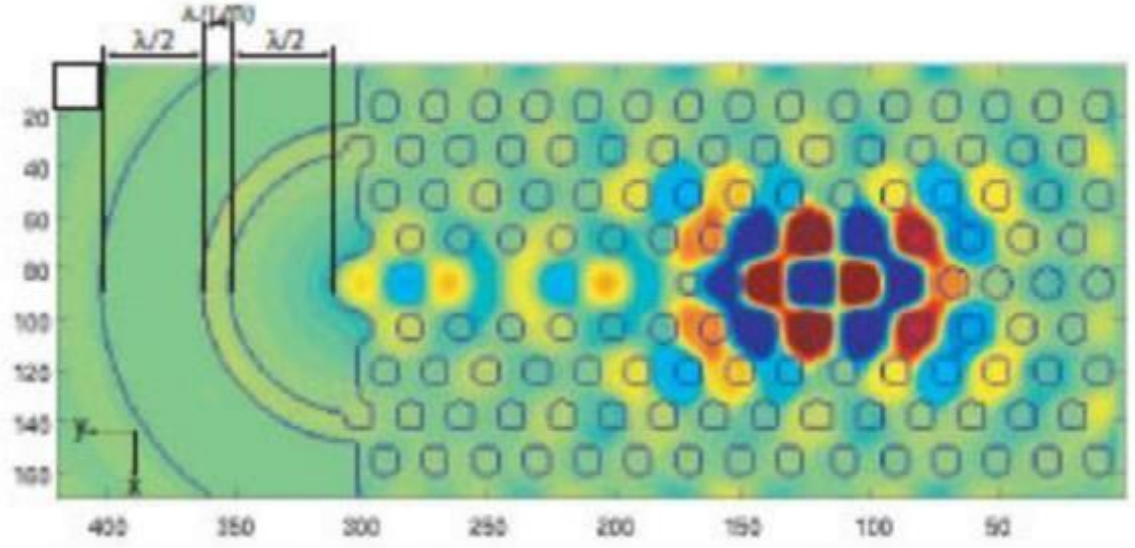

Figure 3.1. Magnetic field distribution for a propagating mode in a photonic crystal coupled to a circular grating outcoupler. Viewed in the x-y plane, where the units are in tens of nanometres [70].

Photonic devices use outcouplers to direct light into optical fibres for single-photon counting. They are often positioned at both ends of the waveguide to collect light in either direction. Circular grating outcouplers consist of periodically spaced air rings where the GaAs wafer is etched away (Figure 3.1). When light reaches the grating, destructive interference occurs in the forward propagation direction, scattering light upwards into an

overhead collection fibre. The required width of the air rings and their separation can be theoretically determined, if both the refractive index of the substrate material and the wavelength of incident light is known. The width is given by

$$w = \lambda/2 \tag{3.1}$$

where λ is the wavelength of light incident on the grating. The separation is then given by

$$s = \lambda/2n \tag{3.2}$$

where n is the refractive index of the grating material [70]. The refractive index of GaAs at a wavelength of 925 nm and a temperature of 4 K is approximately 3.4 [71], giving a theoretical width of 462.5 nm and a theoretical separation of 135 nm.

The circular grating design can be optimised for maximal light transmission into the collection fibre, minimal reflection of light back into the input waveguide and a focused collection region. Using 3D FDTD, I take an old outcoupler design and improve it for better light collection.

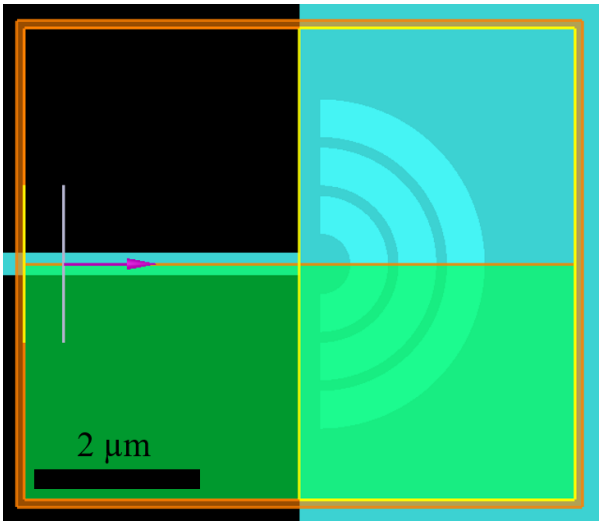

Figure 3.2. Top-down view of the original outcoupler design in FDTD. The darker blue material is the waveguide. The lighter blue material is the etch. The purple arrow is the input light source. The yellow lines are the light detectors. The orange rectangle is the simulation region. The green area is the region of anti-symmetry.

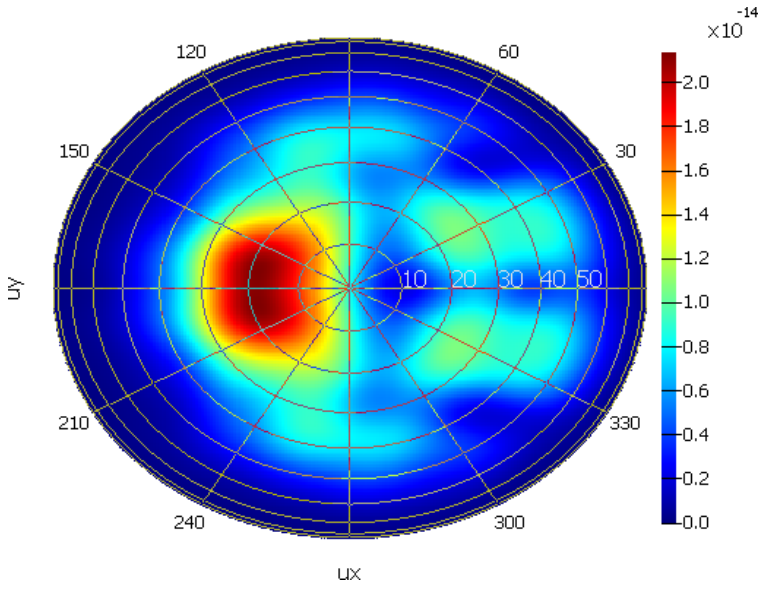

Figure 3.3. Far-field profile at λ = 925 nm, in polar coordinates. The colour gradient represents the normalized field density.

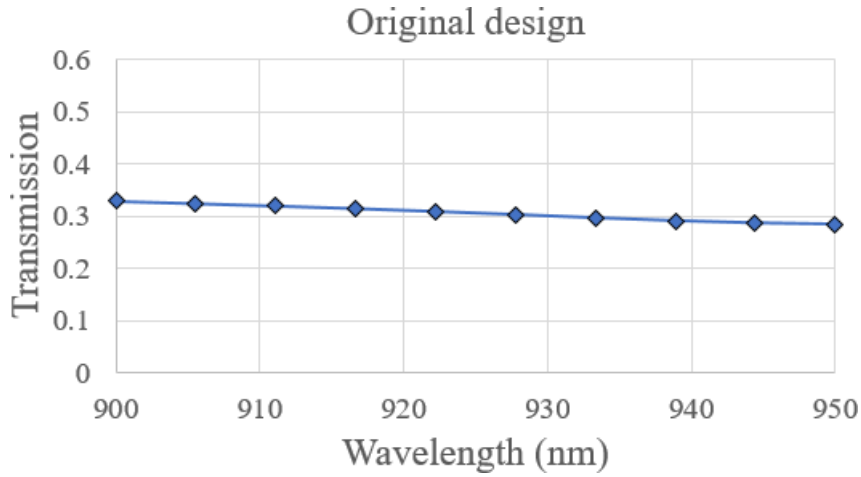

Figure 3.4. Transmission versus wavelength of input light.

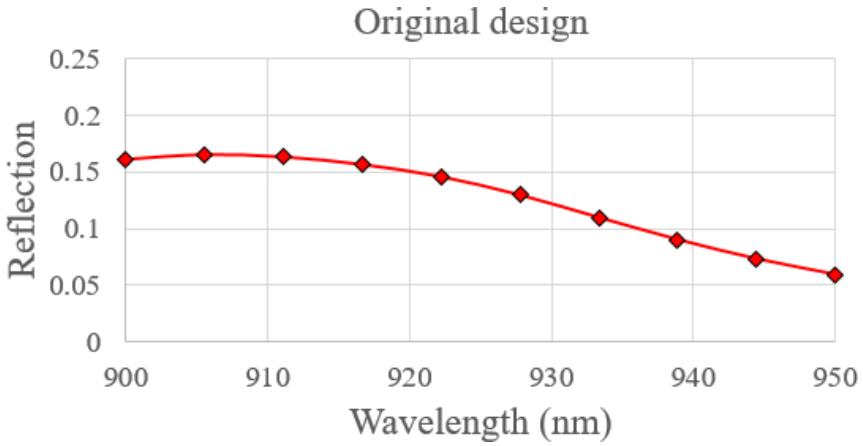

Figure 3.5. Reflection versus wavelength of input light.

My outcoupler simulations use an input source inside a waveguide that emits light from 900 nm to 950 nm (Figure 3.2). Light detectors are placed above, behind, to the left, and to the right of the outcoupler. The detector above the outcoupler determines how much light can be coupled into a collection fibre positioned above the outcoupler. It facilitates the viewing of the far-field profile, a colour map of the electromagnetic field, calculating scattering amplitudes and phases of the electromagnetic field for all scattering angles [72].

There is a detector placed behind the input source, determining the quantity of light that reflects off the outcoupler and back into the input waveguide. The sum of all light detected from all the detectors is approximately 100%, as expected. The outcoupler design is symmetrical in the z direction (waveguide depth) and anti-symmetrical in the y direction (waveguide width), so regions of symmetry/anti-symmetry are added to lower memory consumption, for fast simulation.

The original circular grating outcoupler design uses three air rings, spaced by the theoretical ideal separation, with a width slightly higher than the theoretical ideal width. The far-field profile should be a centred circle for best coupling to an overhead collection fibre, but here it is off-centre and badly focused (Figure 3.3). The transmission over the full wavelength range is consistently good (Figure 3.4). However, the reflection back into the waveguide is excessive and is particularly high at shorter wavelengths (Figure 3.5).

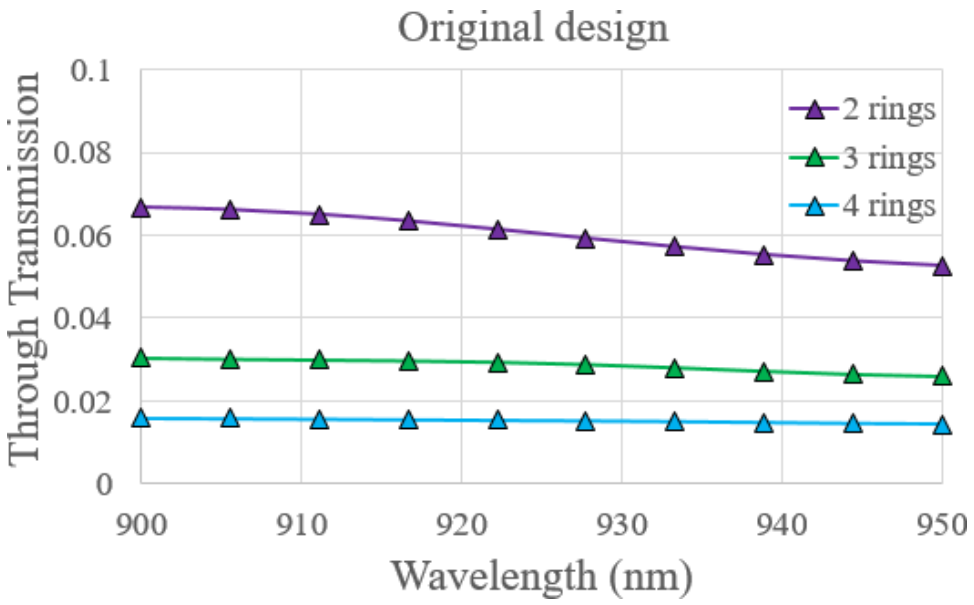

Figure 3.6. Through-transmission versus wavelength for different numbers of rings.

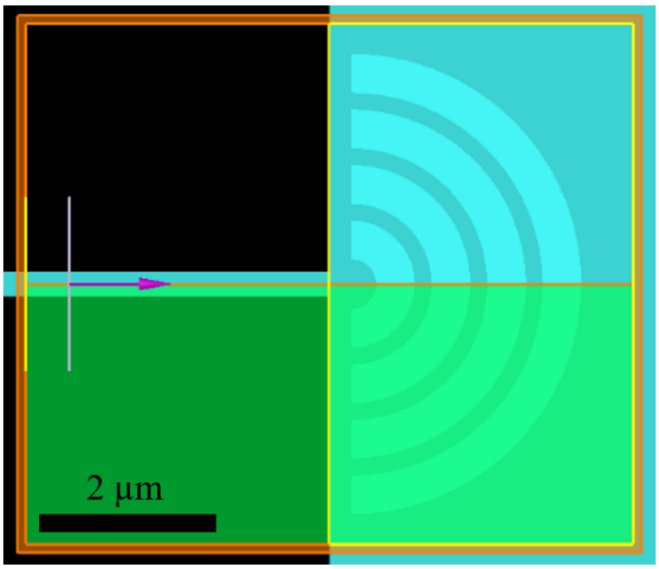

Figure 3.7. Top-down view of my outcoupler design in FDTD.

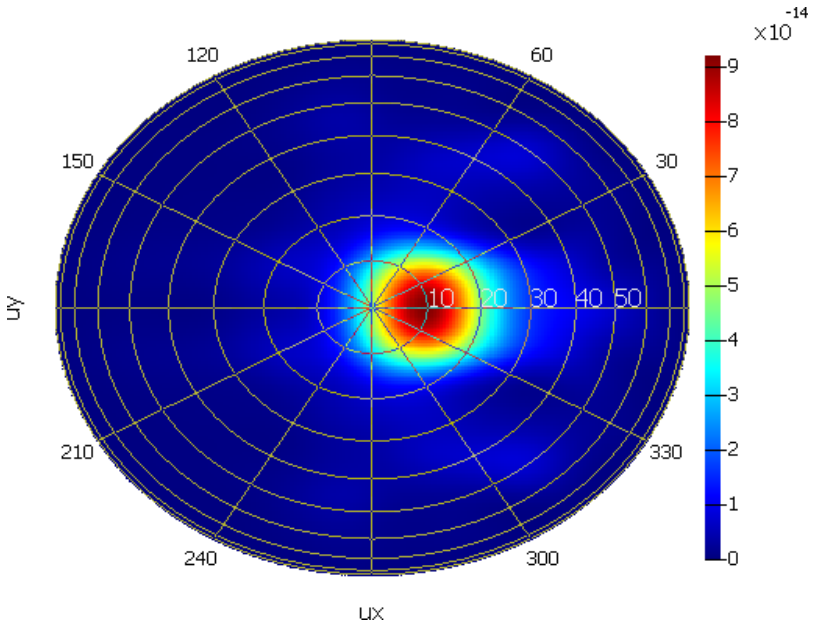

Figure 3.8. Far-field profile of my design at λ = 925 nm.

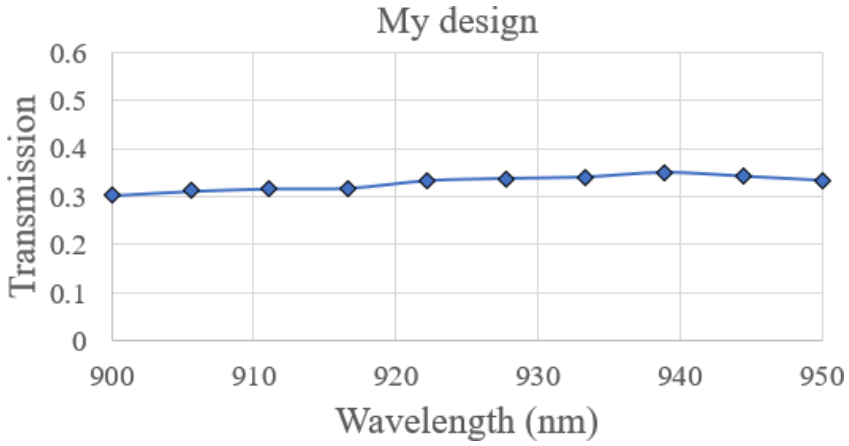

Figure 3.9. Transmission versus wavelength of input light for my design.

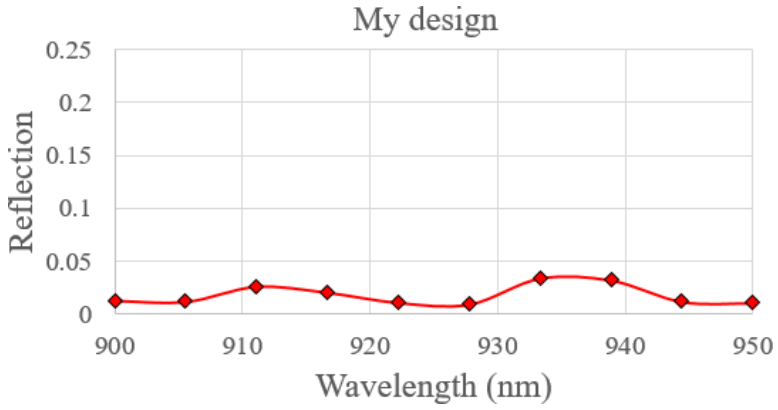

Figure 3.10. Reflection versus wavelength of input light for my design.

	Rings	r1 (nm)	w (nm)	s (nm)	g (nm)	Mean T	Mean R	NA (%)
Original design	3	625	480	135	260	0.31	0.12	44
My design	4	510	450	190	250	0.33	0.02	69

Table 3.1. Comparison between the original outcoupler design and my design. r1 is the radius of the first ring. w is the width of each ring. s is the separation of the rings. g is the gap between the end of the waveguide and the outcoupler. T/R is the transmission/reflection within a 900 to 950 nm wavelength. NA is the 0.5 numerical aperture value.

Each added air ring reduces the light that escapes behind the outcoupler, also known as the through-transmission (Figure 3.6). Using many air rings would make the outcoupler too large and it would be more difficult to fabricate, therefore using four air rings is a good compromise. My improved outcoupler design is shown in (Figure 3.7). The geometry of the outcoupler is adjusted: air ring radius (decreased), air ring width (slightly decreased), the separation of the air rings (significantly increased) and the distance of the first air ring from the end of the waveguide (about the same).

The far-field profile is better centred and more circular (Figure 3.8). The transmission sees a slight improvement, particularly for longer wavelengths (Figure 3.9). The reflection back into the waveguide is now consistently low throughout the entire wavelength range (Figure 3.10). The 0.5 numerical aperture value (0.5 NA) measures how efficiently light can be coupled to a collection fibre. A 0.5 NA of 69% is obtained at the central wavelength of 925 nm, meaning that this percentage of light is contained within a 30^0 cone of the far-field. For the original outcoupler design, this value is only 44%. The differences between the original design and my design are noted in Table 3.1.

When fabricating outcouplers for photonic devices, it is highly likely that the dimensions will be slightly different than intended due to the accuracy limitations of the patterning process. Therefore, the four main parameters of the outcoupler design are shifted by ± 20 nm to investigate the impact of fabrication inaccuracies on transmission/reflection.

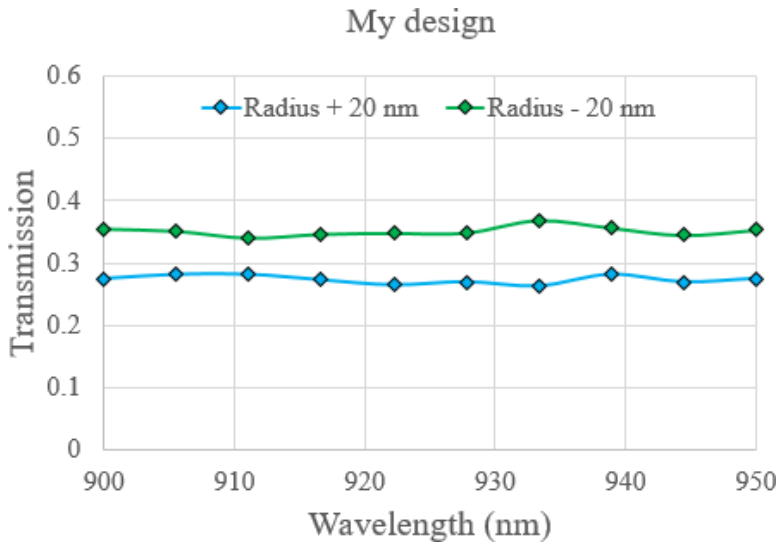

Figure 3.11. Transmission versus wavelength of input light for a radius shift.

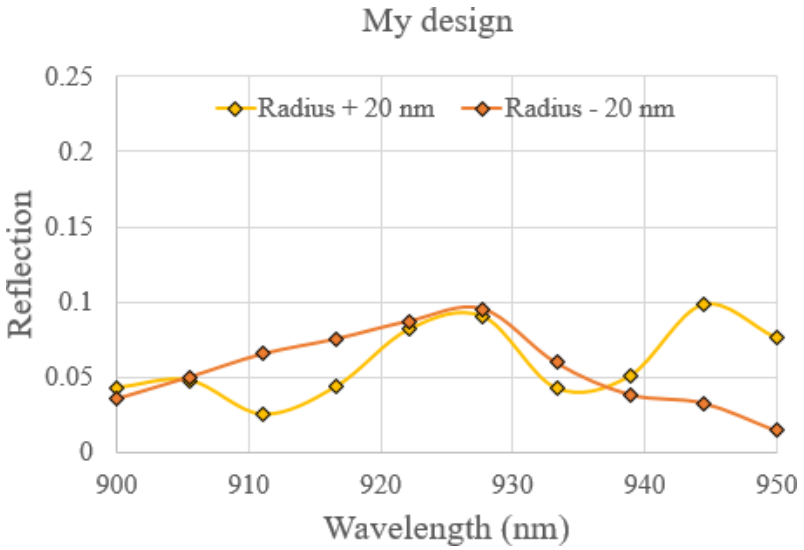

Figure 3.12. Reflection versus wavelength of input light for a radius shift.

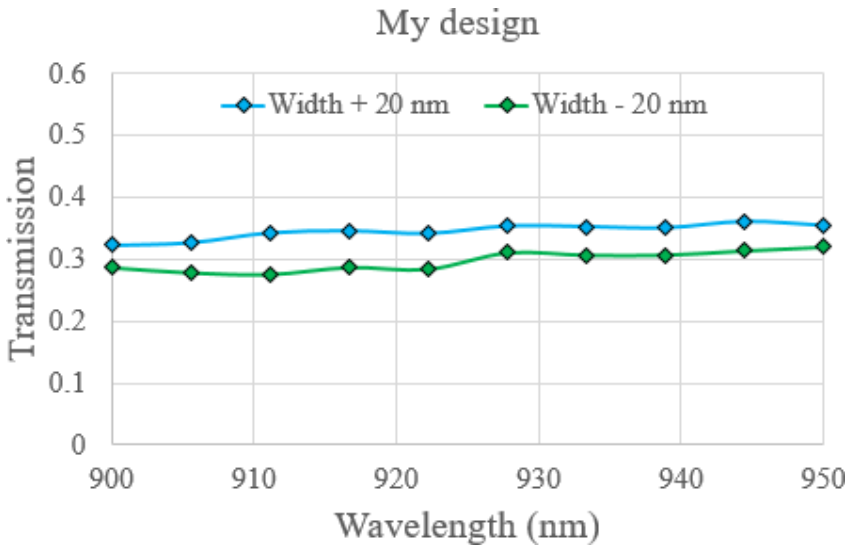

Figure 3.13. Transmission versus wavelength of input light for a width shift.

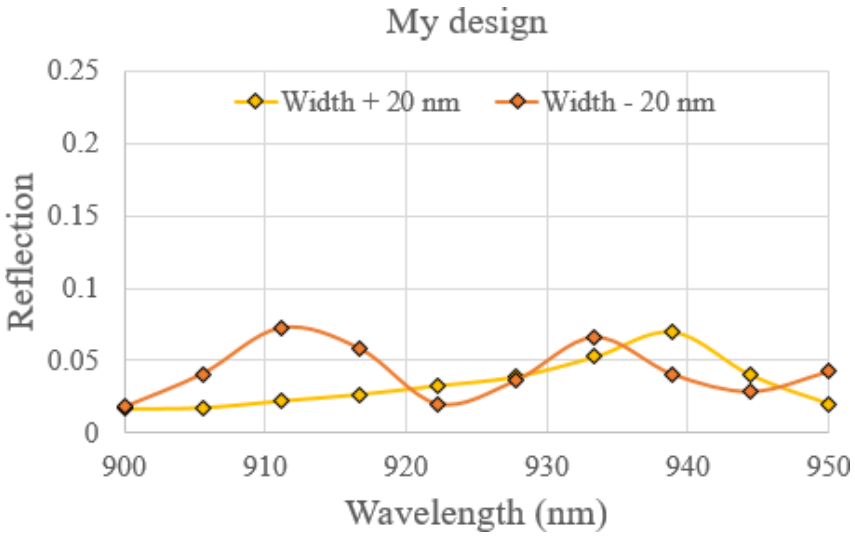

Figure 3.14. Reflection versus wavelength of input light for a width shift.

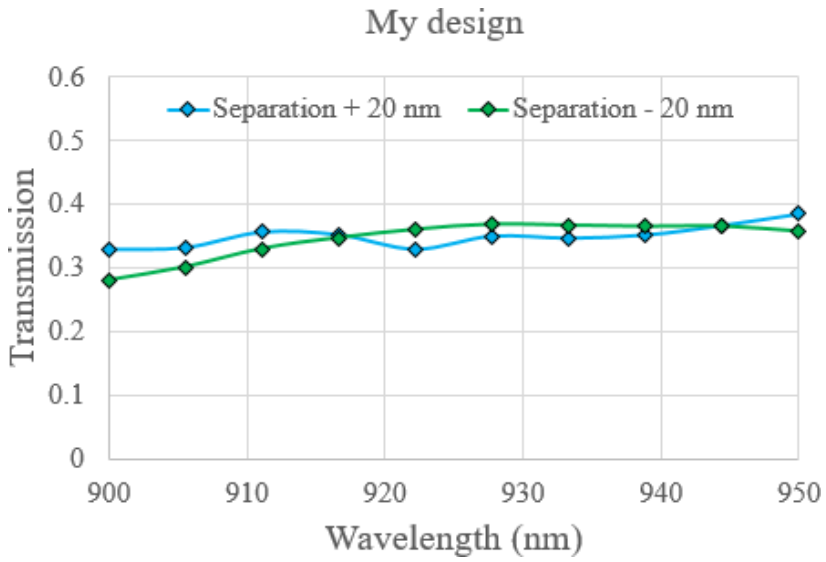

Figure 3.15. Transmission versus wavelength of input light for a separation shift.

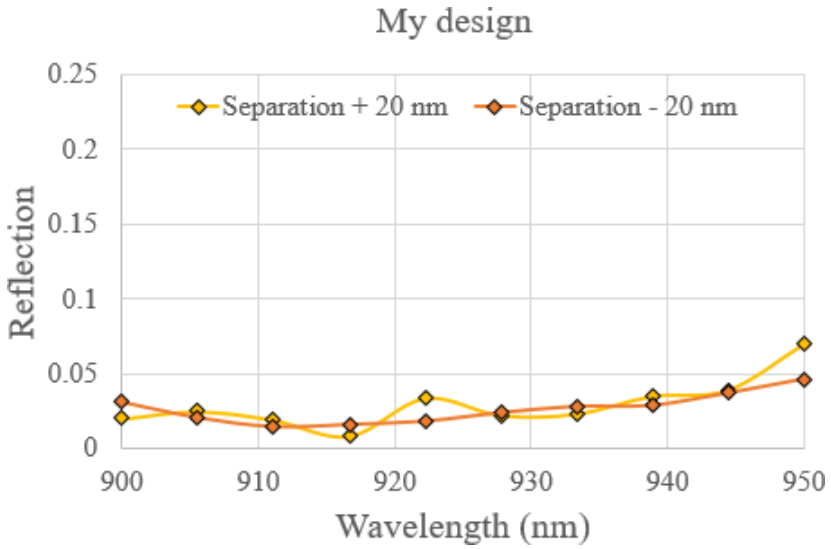

Figure 3.16. Reflection versus wavelength of input light for a separation shift.

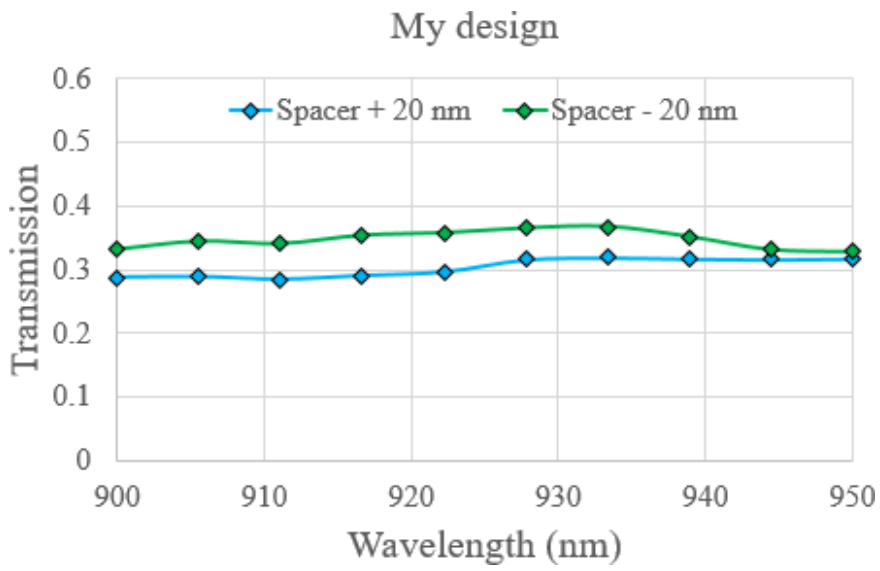

Figure 3.17. Transmission versus wavelength of input light for a spacer shift.

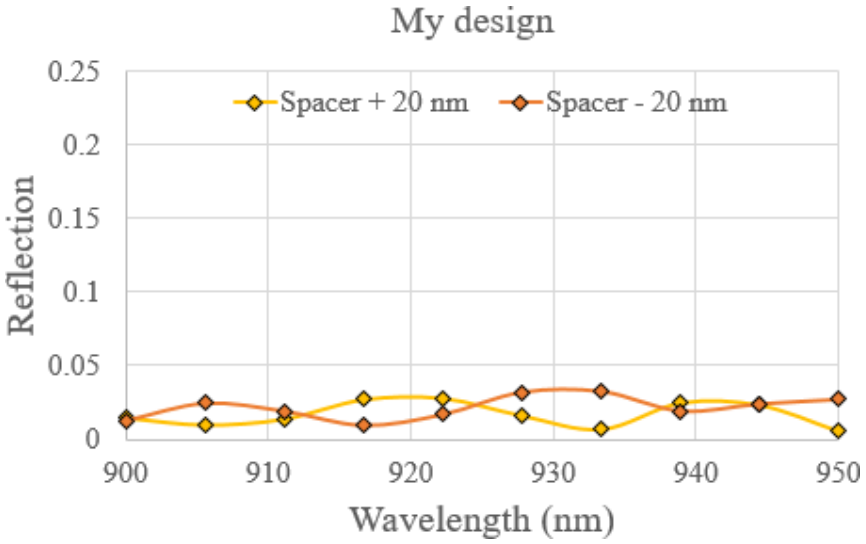

Figure 3.18. Reflection versus wavelength of input light for a spacer shift.

Parameter perturbations are performed for my improved outcoupler design: air ring radius, transmission (Figure 3.11) and reflection (Figure 3.12); air ring width, transmission (Figure 3.13) and reflection (Figure 3.14); separation between the air rings, transmission (Figure 3.15) and reflection (Figure 3.16); the distance of the first air ring from the end of the

waveguide, transmission (Figure 3.17) and reflection (Figure 3.18). Of all four parameters, a 20 nm shift in ring-radius has the biggest impact on transmission and reflection. Reflection back into the input waveguide still remains below 10% throughout.

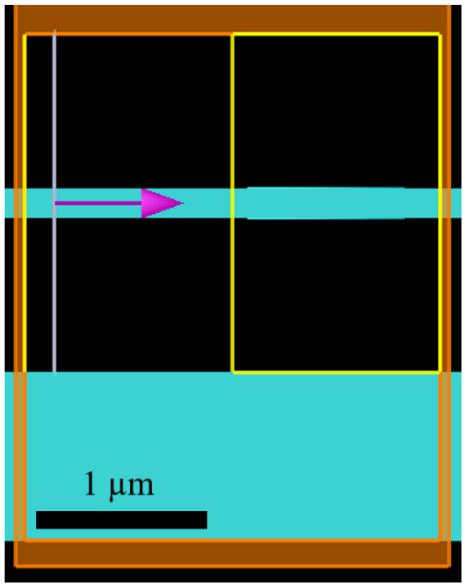

Figure 3.19. Side view of the outcoupler-wafer design in FDTD. The upper blue slab is the waveguide, and the lower blue slab is the wafer.

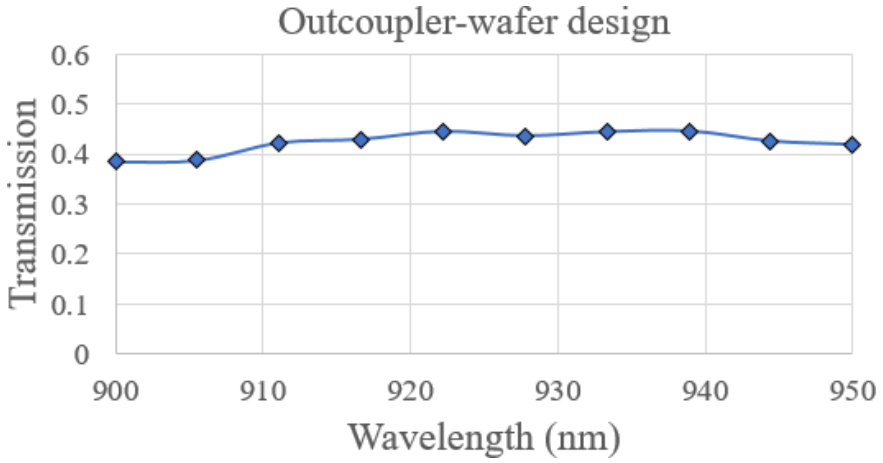

Figure 3.20. Transmission versus wavelength of input light for the outcoupler-wafer design.

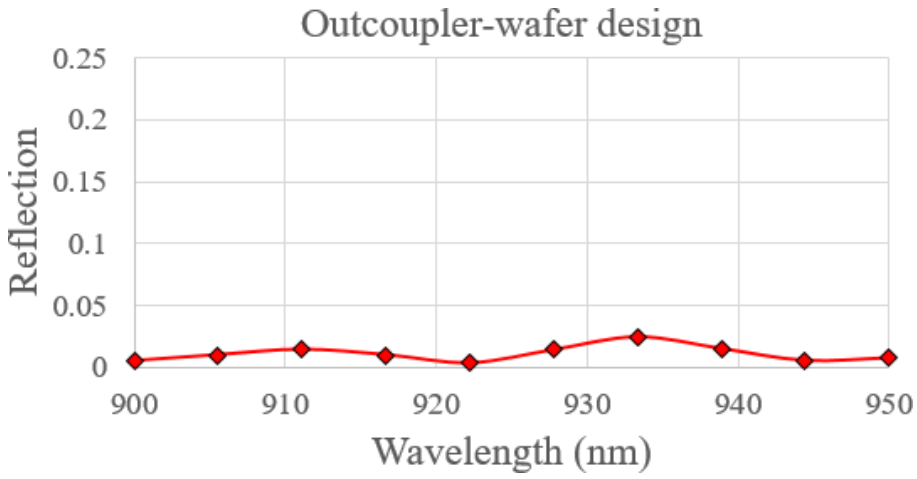

Figure 3.21. Reflection versus wavelength of input light for the outcoupler-wafer design.

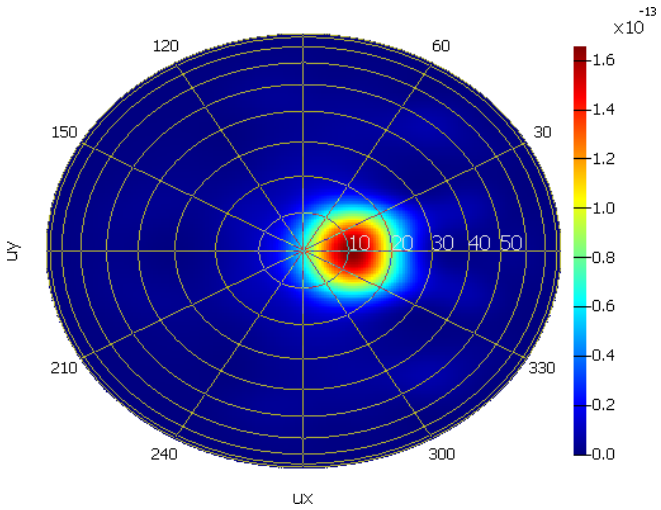

Figure 3.22. Far-field profile of the outcoupler-wafer design at λ = 925 nm.

So far, my simulations have considered the outcoupler in isolation. In reality, the outcoupler has a thick layer of material situated beneath it: the GaAs wafer. Adding a 1 µm layer of GaAs material to the simulation region, 1 µm below the waveguide (Figure 3.19), I regathered transmission, reflection and far-field data. The transmission increases (peaking at 45% rather than 35%), thanks to light reflecting off the wafer and into the

overhead detector (Figure 3.20). Reflection properties are improved, peaking at 2.5% rather than 3.5% (Figure 3.21). The far-field also sees some improvement, with a 0.5 NA of 77% (Figure 3.22).

3.2 Broadband light transmission

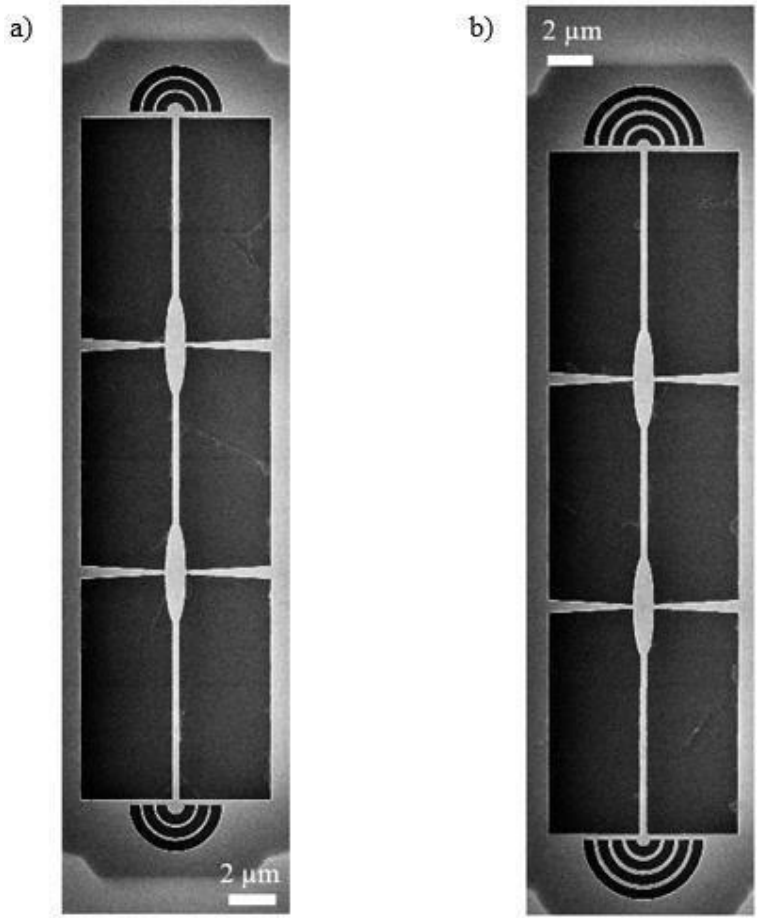

Figure 3.23. SEMs of 30 µm long NBWGs. a) equipped with the original outcoupler design. b) equipped with my outcoupler design.

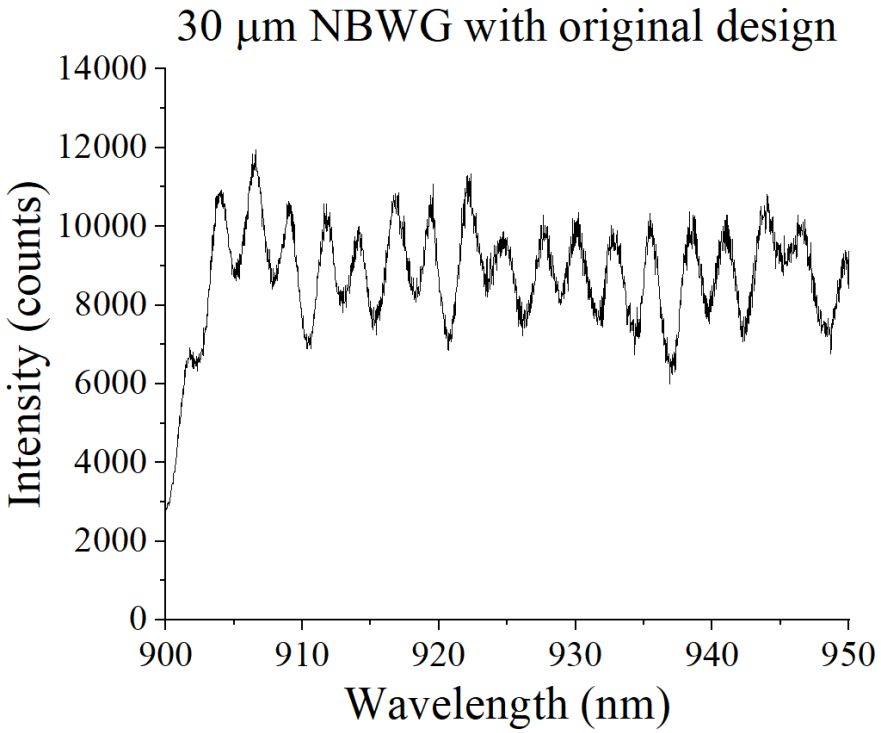

Figure 3.24. broadband light transmission for the original design.

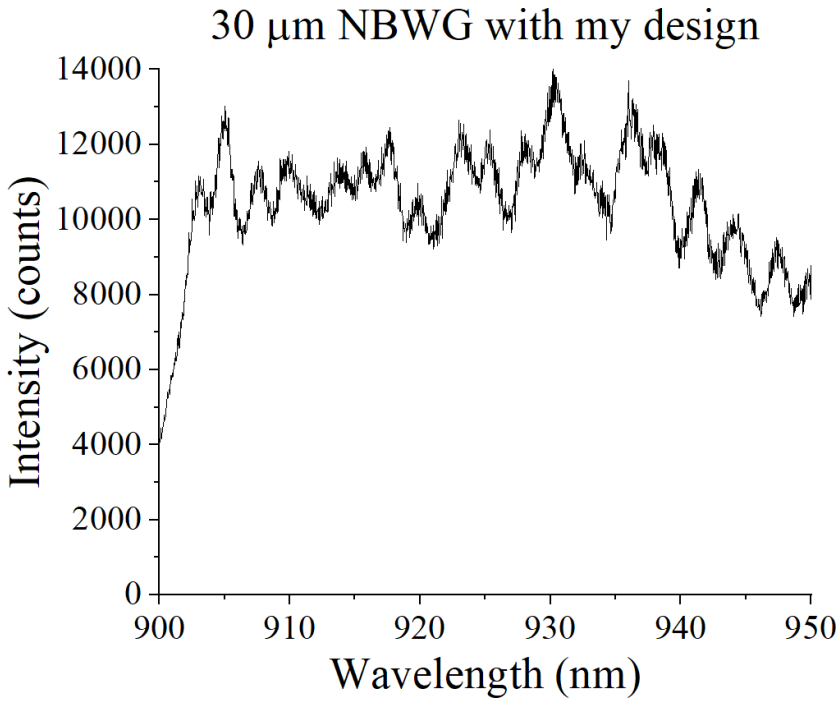

Figure 3.25. broadband light transmission for my design.

NBWGs are fabricated on a GaAs wafer to compare my outcoupler design with the original outcoupler design (Figure 3.23). They are 30 μm long, with support structures to prevent the waveguide from collapsing during fabrication. Testing is done at room temperature with a broadband light source, filtered for 900 nm to 950 nm wavelengths. To evaluate the efficiency of the outcouplers, an optical fibre directs the light onto the bottom outcoupler. The light travels through the waveguide, and a second optical fibre collects the light from the top outcoupler, sending the light to a spectrometer, recording its intensity and wavelength. Results are presented for the best devices of each type (Figure 3.24 and Figure 3.25). For the original outcoupler design, the mean transmission is 10,600 counts. For my outcoupler design, the mean transmission is 12,300 counts, an increase of 14%. To compare the magnitude of reflection, the visibility of each spectrum is determined using the peak analyser in the data analysis software Origin. The intensity of each peak and corresponding dip is recorded, the visibility equal to the mean peak height when the maximum intensity is normalized to a value of one (Section 1.6, Eq. 1.5). For the original outcoupler design, the visibility is 0.25. For my outcoupler design, the visibility is 0.18, a reduction of 28%. As predicted by my simulations, my design achieves higher mean transmission and lower mean reflection for the target wavelength region.

To conclude, my 4-ring outcoupler design increased broadband light transmission into the collection fibre (14%) and reduced reflection back into the waveguide (28%) compared to the original 3-ring outcoupler design, for the target wavelength region of 900-950 nm. This is thanks to parameter tweaks (radius of the first ring (625 nm to 510 nm), width of the rings (480 nm to 450 nm), and ring separation (135 nm to 190 nm)), combined with the extra ring to reduce through-transmission.

4 Beamsplitters for Interference of Light

4.1 Directional coupling

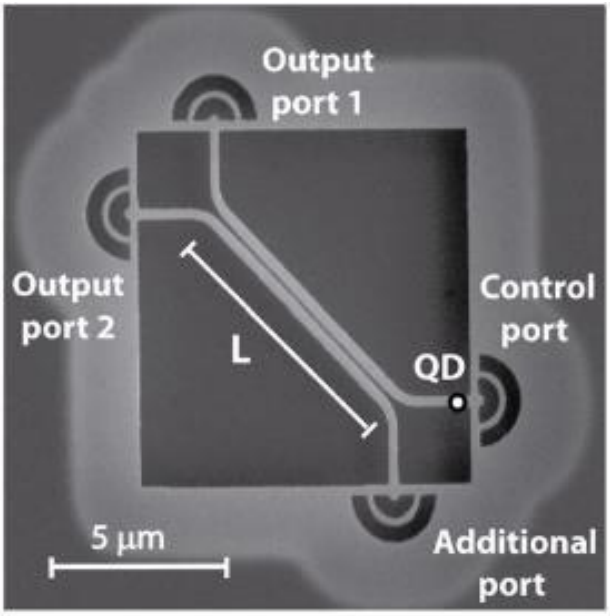

Figure 4.1. SEM of an air-clad, free-standing directional coupler (DC), used for beam-splitting of single photons from an InGaAs QD [73].

The directional coupler (DC) is a type of beamsplitter that can transfer light from a waveguide to a nearby waveguide (Figure 4.1). It can be used as a component in a photonic circuit for classical interference of light or quantum interference of photons. These photonic devices rely on weak coupling of light in the transverse electric polarization, produced by

the superposition of individual waveguide eigenmodes, creating super modes. The splitting ratio of the DC is defined as the portion of light exiting the upper waveguide (known as the cross waveguide) over the sum of light exiting both waveguides. It is vital to obtain a splitting ratio close to 0.5, meaning that roughly the same amount of input light exits through each waveguide, starting with light injected exclusively into the lower waveguide. Splitting ratio deviations from the ideal value of 0.5 have been shown to decrease the visibility of Hong-Ou-Mandel interference [74]. Another requirement for high performance beam-splitting is the minimization of light lost into free space, achieved through dimensional optimisation. The coupling length required to obtain any splitting ratio is defined by

$$L = \frac{\lambda_0}{\pi \Delta n} arcsin(s) \qquad 4.1$$

where λ_0 is the wavelength of input light, s is the splitting ratio, and Δn is the effective index difference between the fundamental and the first-order propagating modes [73].

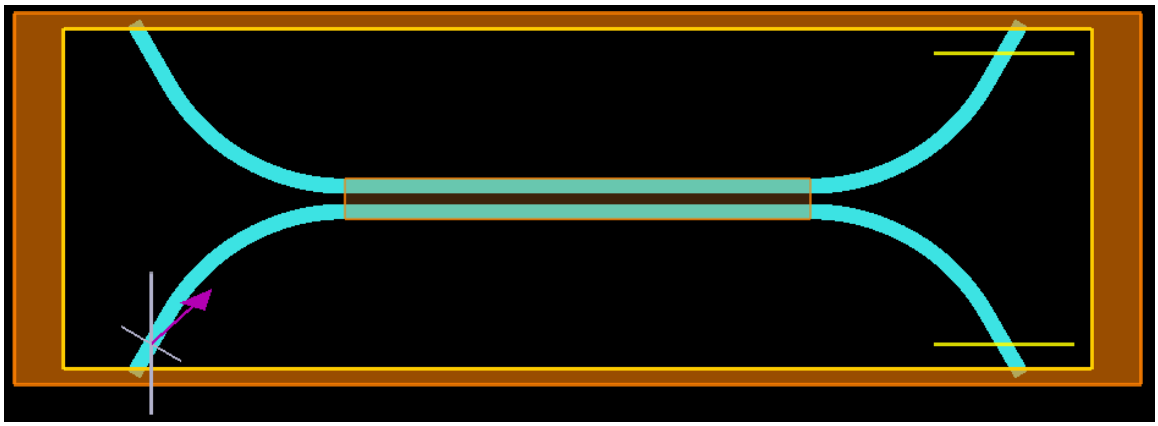

Figure 4.2. DC in FDTD. The blue material is the waveguide, the orange rectangle is the simulation region, the purple arrow is the input source, and the yellow lines are the detectors (y-normal cross transmission (upper right), y-normal parallel transmission (lower right) and z-normal field profile around the entire structure). The smaller orange rectangle around the coupling region is a higher-resolution mesh.

Previous DCs have been designed with small waveguide separations, as low as 70 nm [75]. A smaller waveguide separation would speed up the transfer of light, shortening the device. However, this increases the probability of waveguides fusing together during fabrication, rendering the device unusable. Even if the fabrication was successful, any small deviation from the intended separation would drastically change the splitting ratio of the device. Therefore, I aim to design a DC that can evenly split light, with waveguides that are further apart, all the while still retaining its compactness.

When constructing a DC, parameters such as coupling length, waveguide width and waveguide separation must be optimised to obtain a splitting ratio of 0.5 with minimal transmission loss. I again use 3D FDTD, with my final design shown in Figure 4.2. The

waveguides begin far apart, and are brought into a closer distance by bends of 3 µm radii (previous work has found that propagation losses caused by waveguide bending become negligible with radii > 2 µm [73]). Perfectly matched layer boundary conditions are selected to absorb the light at the interfaces of the waveguides. I enable z symmetry to reduce memory requirements for faster simulations, which is suitable as the DC is symmetric in this axis but not in any other axes. A high-resolution grating mesh is placed around the coupling region for high-accuracy mode coupling. A source is positioned in the bottom waveguide emitting light from 900 nm to 950 nm. Detectors are placed at the exits of the top and bottom waveguides, collecting the data which determines the transmission loss and splitting ratio of the device.

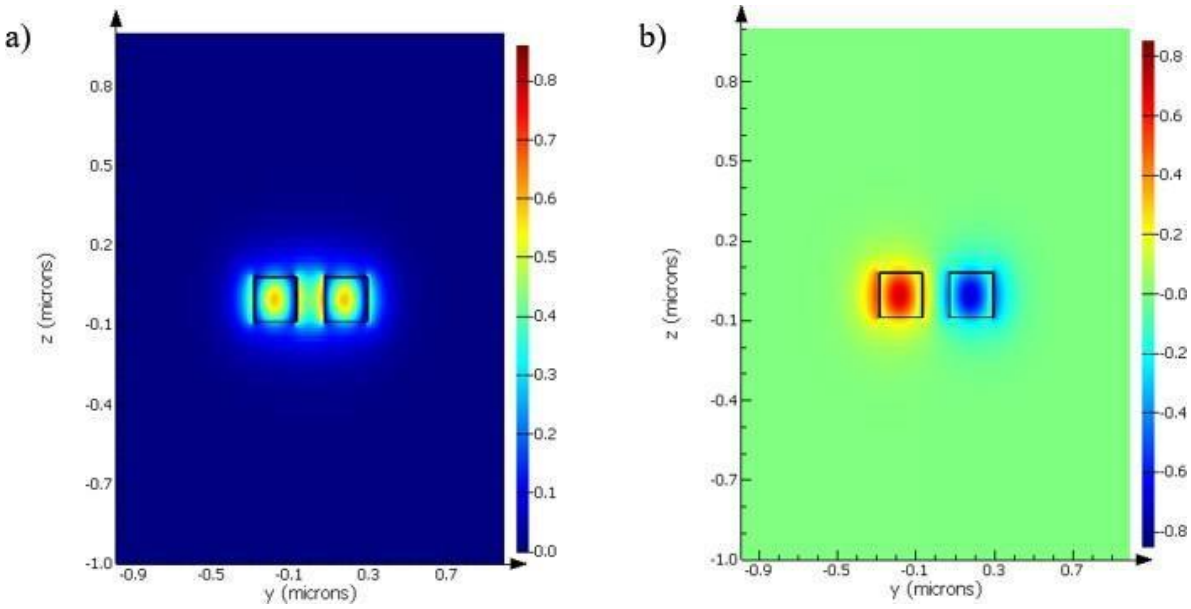

Figure 4.3. Modal fields for the two closely spaced waveguides (black rectangles) of the DC, in 3D FDTD. Colour chart shows the field density. a) Fundamental modal field. b) First-order modal field.

To find the coupling length that will produce a certain splitting ratio for a given DC, a source is placed at the centre of the coupling region, for modal calculations. The resulting modal fields are shown in Figure 4.3, from which the effective index difference can be calculated. Displayed is the real part of the y-component of the electric field for the fundamental and the first-order propagating modes. It can be clearly seen from Figure 4.3 that the fundamental propagating mode is symmetric, and the first-order propagating mode is antisymmetric, as expected. The waveguide width, waveguide separation, and wavelength of input light are parameters which combine to determine the effective indices of the two modes.

For maximum interference visibility, the DC must be low-loss, meaning that a high percentage of input light is collected at the two output detectors of the DC. Losses typically arise from waveguide bending, light propagation and mode conversion [76]. The loss of the DC in decibels is calculated by

$$Loss_{dB} = 10log\left(\frac{1}{T_c+T_p}\right) \qquad 4.2$$

where T_c is the transmission collected at the cross detector (upper right of the device) and T_p is the transmission collected at the parallel detector (lower right of the device). The transmission is given as a value between zero (no light detected) and one (all light detected).

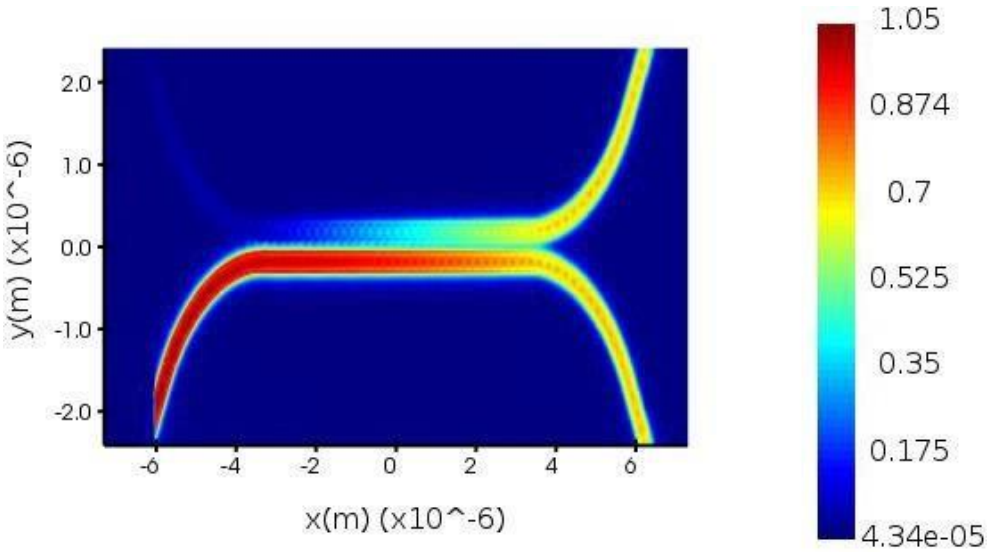

Figure 4.4. Electric field profile of the DC.

Although light transfer is intended to take place within the coupling region, it will also arise before and after this segment, due to the proximity of the waveguides. This means that the coupling length calculated using Eq. 4.1 will always be an overestimate. To compensate for this, the simulation is initiated with the coupling length acquired from Eq. 4.1, then the simulated splitting ratio is fed back into Eq. 4.1 to calculate the required coupling length. The extra coupling length due to input/output waveguide proximity was found to be 1.5 µm (23% of the final coupling length).

With a sufficiently high waveguide width and waveguide separation of 220 nm and 140 nm respectively, the optimal coupling length is found to be 6.7 µm. This gives a splitting ratio of 0.502, with the transmission loss calculated to be 0.18 dB (Eq. 4.2). The even splitting of light is visually represented by the electric field profile of the DC (Figure 4.4).

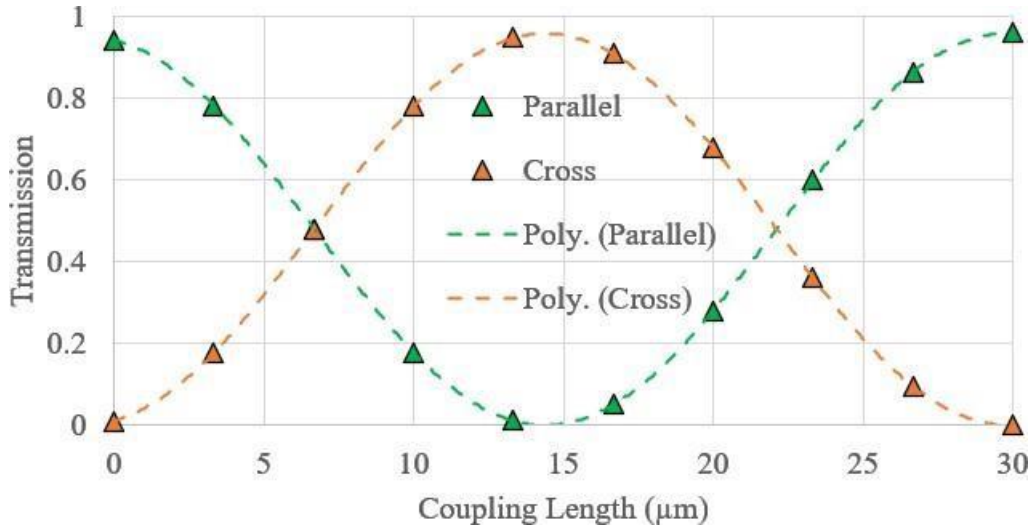

Figure 4.5. DC transmission versus coupling length for the parallel (lower right) and cross (upper right) detectors, with sixth-order polynomial fits.

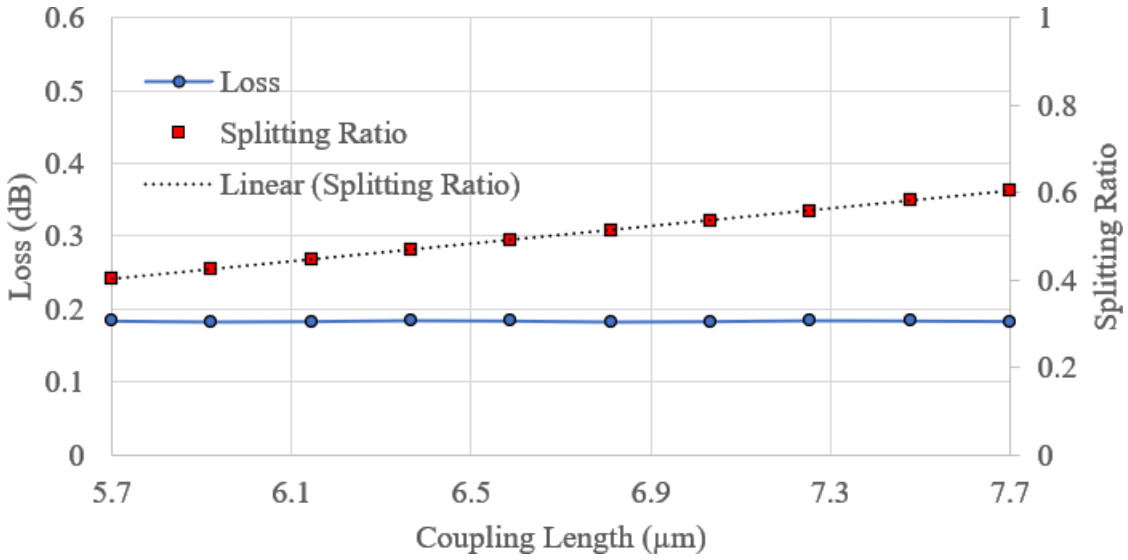

Figure 4.6. DC splitting ratio (with linear fit) and loss versus coupling length.

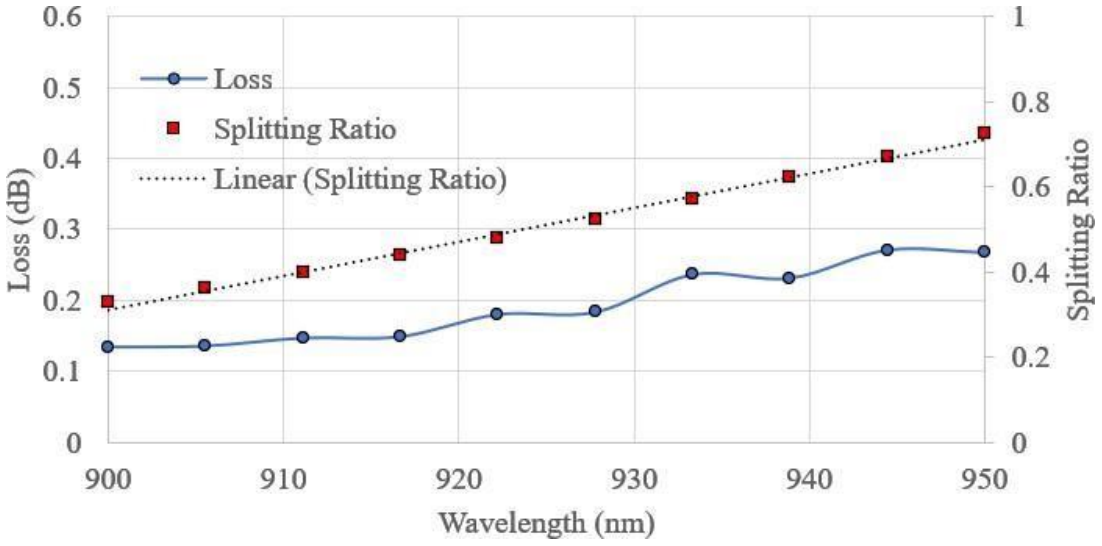

Figure 4.7. DC splitting ratio (with linear fit) and loss versus wavelength of input light.

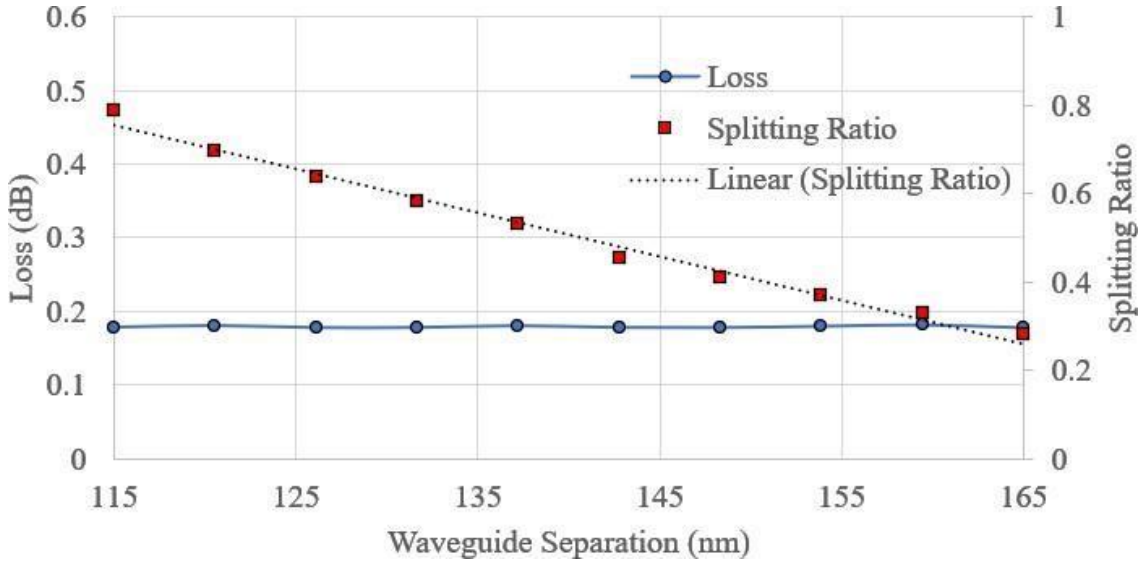

Figure 4.8. DC splitting ratio (with linear fit) and loss versus waveguide separation.

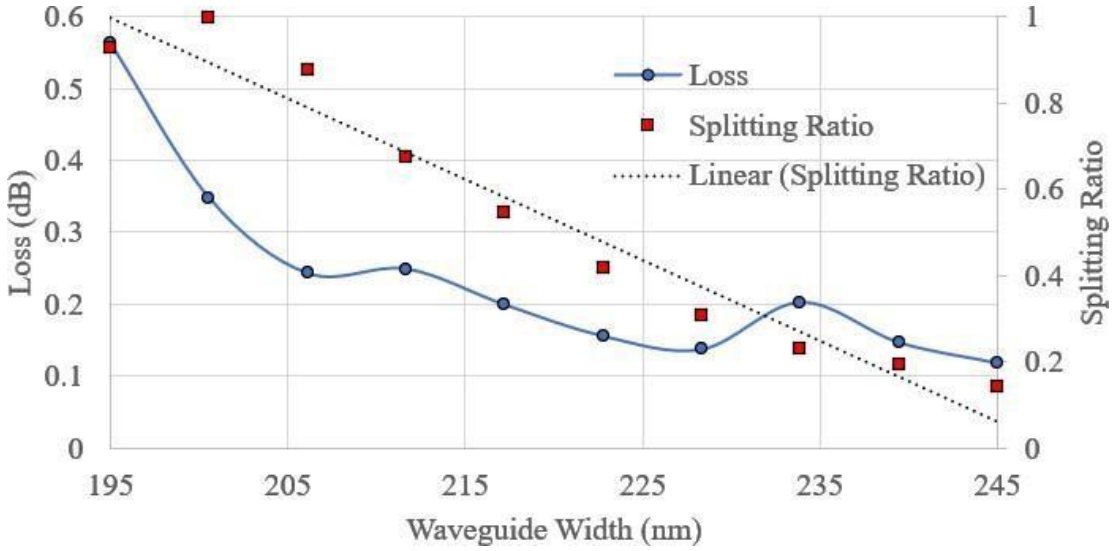

Figure 4.9. DC splitting ratio (with linear fit) and loss versus waveguide width.

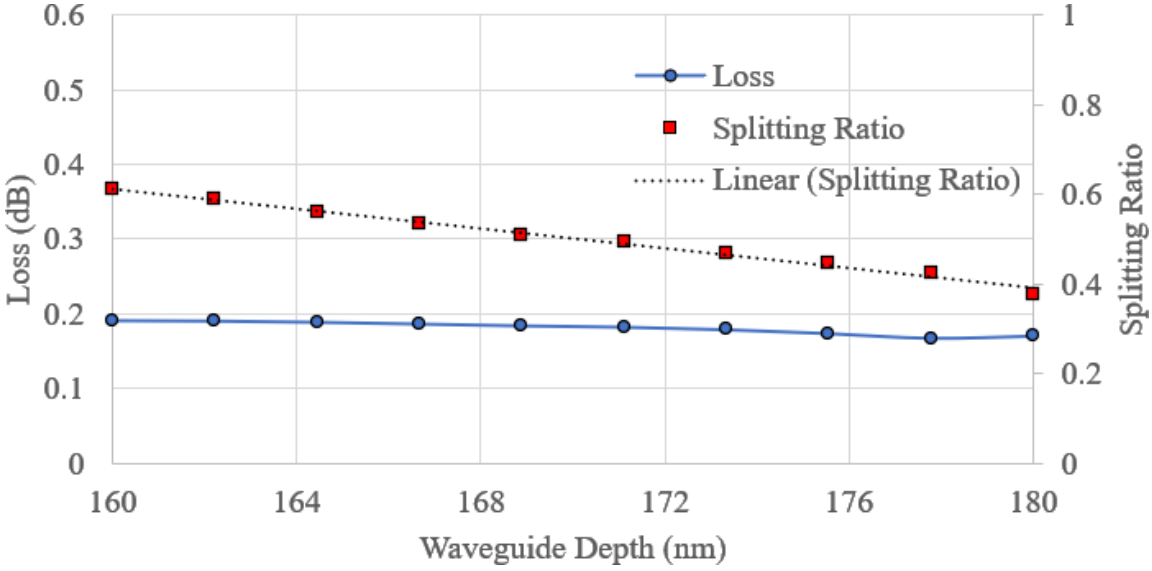

Figure 4.10. DC splitting ratio (with linear fit) and loss versus waveguide depth.

For figures 4.6 to 4.10, the central values are the constants (coupling length = 6.7 μm, wavelength = 925 nm, waveguide separation = 140 nm, waveguide width = 220 nm, waveguide depth = 170 nm). At a coupling length of zero, all the input light from the left of the bottom waveguide propagates to the right of the bottom waveguide, where it passes through the parallel detector. If the coupling length becomes non-zero, light is transferred from the bottom waveguide to the top waveguide, whereby light propagates to the right of the top waveguide and passes through the cross detector. As this length increases, more light is transferred to the top waveguide, until even splitting of light is achieved at a coupling length of around 6.7 μm. If the coupling length is increased beyond this point, light is transferred back and forth between the top and bottom waveguides. The transmission changes sinusoidally with coupling length, verified by plotting a sixth-order polynomial trendline to each set of data points (Figure 4.5). For a much smaller manipulation of the coupling length, the splitting ratio changes linearly, and the transmission loss remains stable at a low level (Figure 4.6). Sweeping through the wavelength range, the splitting ratio again changes linearly but the transmission loss increases as the wavelength of input light increases (Figure 4.7). Rather confusingly, decreasing the wavelength of input light increases the required length of the DC, as changing the wavelength of input light also changes the effective index difference used in Eq. 4.1. Therefore, a longer wavelength induces stronger mode confinement of the light within the waveguide.

As the waveguides are moved further apart, the coupling of the light is slower, increasing the required coupling length for a splitting ratio of 0.5 (Figure 4.8). As was the case when varying the coupling length, the transmission loss remains stable at a low level. For wider

waveguide widths, there is slower coupling of light due to stronger mode confinement, also increasing the required coupling length for a splitting ratio of 0.5 (Figure 4.9). Transmission loss increases quite significantly as the waveguides become narrower. Furthermore, t he splitting ratio varies more strongly with a change in waveguide width than with a comparable change in waveguide separation, varying non-linearly when approaching a splitting ratio of zero or one. The depth of the waveguides should be 170 nm (as this is the typical thickness for GaAs waveguides), but this is prone to slight variation during the fabrication process. Similarly with increasing the waveguide width, increasing the waveguide depth results in stronger mode confinement and thus slower coupling, indicated by the splitting ratio trend of Figure 4.10. The transmission loss remains stable at a low level, hence out of all the parameters, a change in waveguide width has the biggest impact on the performance of the DC.

4.2 Multimode interferometry

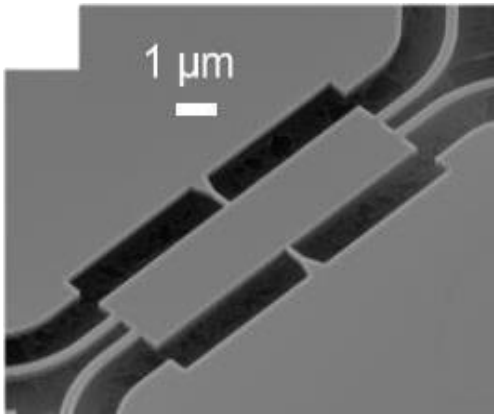

Figure 4.11. SEM of a 2x2 multimode interferometer (MMI) used for electro-optical switching of photons from an InAs QD in AlGaAs waveguides [77].

An alternative beamsplitter is the multimode interferometer (MMI). Using this photonic device, the two different polarization states of light (transverse electric/transverse magnetic) can be split and recombined, potentially doubling the capacity of optical transmission systems [78]. The MMI has input waveguides and output waveguides, between which is a wide waveguide known as the multimode waveguide (Figure 4.11). There can be numerous iterations of input waveguides N and output waveguides M, but it is required that $M \geq N$. This is proven by applying the rank-nullity theorem of linear algebra to a matrix interpretation of a lossless MMI, asserting the dimension of a mapping vector space is equal to the sum of the kernel dimension and the image dimension [79].

The MMI operates according to the Talbot effect, dictating if a monochromatic optical plane wave is incident on a periodic diffraction grating, the image of the grating will repeat itself at a certain distance along the grating. This happens because incoming light exits the narrow input waveguide into the wide multimode waveguide of the MMI, whereby propagating modes interfere constructively and destructively to form multiple images along the multimode waveguide [80].

The splitting ratio of the MMI is defined as the portion of light exiting the lower right output waveguide (known as the cross waveguide) over the sum of light exiting both output waveguides. A 1x2 MMI has one input waveguide and two output waveguides. Due to its symmetrical design about the axis of light propagation, the splitting ratio will always be 0.5, no matter the length of the multimode waveguide. A 2x2 MMI has two input waveguides and two output waveguides, with light injected exclusively into the upper left input waveguide. This design is asymmetrical about the axis of propagation, so the splitting ratio changes as the coupling length changes.

There are two methods for calculating the coupling length required to give a splitting ratio of 0.5 for a 2x2 MMI. The first method determines how an input field profile $E(x, z)$ will excite all the guided modes of a multimode waveguide along a propagation distance z. Its equation is

$$E(x,z) = e^{-jk_0 n_1 z} \cdot \sum_{m=0}^{M-1} a_m U_m(x) \cdot e^{2j\pi(m+1)^2 \cdot \left(\frac{z}{L_{si}}\right)} \qquad 4.3$$

where k_0 is the free-space wavenumber, n_1 is the waveguide transverse effective index, m is the number of lateral modes, a_m are the modal excitation factors, U_m are the vector fields, and L_{si} is the self-image length. The final term of Eq. 4.3 is the mode phase factor, which equals one when $z = L_{si}$, producing an image identical to the input field. Therefore, designing the 2x2 MMI to have a multimode waveguide length equal to L_{si} will achieve a splitting ratio of 0.5. The self-image length can be extracted from Eq. 4.3 to give

$$L_{si} = \frac{\lambda}{4\Delta n} \qquad 4.4$$

where λ is the wavelength of input light, and Δn is the effective index difference between the fundamental/first-order propagating modes within the multimode waveguide [81]. The second method uses the effective width of the multimode waveguide: this is the sum of the Goos-Hänchen width and the physical width of the multimode waveguide. The Goos-Hänchen width accounts for the lateral shift experienced by the propagating light when it reflects off the side of the multimode waveguide. The formula for the Goos-Hänchen width of a multimode waveguide is

$$W_g = \frac{\lambda}{\pi}(n_1{}^2 - n_0{}^2)^{-1/2} \qquad 4.5$$

where λ is the wavelength of input light, n_1 is the refractive index of the waveguide material, and n_0 is the refractive index of the cladding material. Therefore, a larger refractive index difference between the waveguide material and the cladding material produces a smaller effective width. For my MMI devices, the cladding is air (n = 1), giving an effective width roughly 5% greater than the physical width of the multimode waveguide. The final equation for the self-image length is then given by

$$L_{si} = \frac{n_1 W_e^2}{2\lambda} \qquad 4.6$$

where n_1 is the refractive index of the waveguide material, W_e is the effective width of the multimode waveguide, and λ is the wavelength of input light. Observing Eq. 4.6, it becomes apparent that decreasing the width of the multimode waveguide will decrease the required length of the multimode waveguide. But the multimode waveguide must be wide enough to both facilitate light interference and to accommodate the wide tapered waveguides [82].

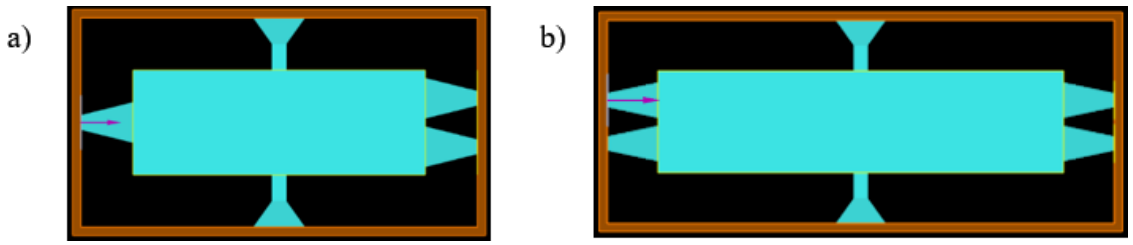

Figure 4.12. MMI designs in FDTD. a) 1x2 MMI. b) 2x2 MMI. The blue material is the waveguide, the orange rectangle is the simulation region, the purple arrow is the input light source, and the yellow lines are the light detectors (x-normal transmission at the output waveguides and z-normal field profile around the multimode waveguide).

I intend for my MMI devices to be compact with minimal transmission loss for the purpose of evenly splitting input light, therefore I again use FDTD for geometrical optimisation. However, because my MMI devices are complex and consequently require many test simulations to find the best designs, I use varFDTD to optimise the geometry. Then I use 3D FDTD to determine the transmission loss and the splitting ratio with higher accuracy. I decided to focus on two types of devices: a 1x2 MMI and a 2x2 MMI (Figure 4.12). The input waveguides and output waveguides are tapered, meaning that the waveguides widen as they approach the multimode waveguide. Previous work has shown that insertion loss is reduced for MMI designs with tapered waveguides, improving its performance when used as a component in a photonic circuit [83]. The tapered waveguides for the 1x2 MMI are made to be as wide as possible, whilst maintaining a 150 nm minimum separation between them. The separation must be sufficiently high to reduce unwanted light transfer between the waveguides and to prevent the waveguides from fusing together during fabrication. Support beams are placed at the centre of the multimode waveguide to prevent the device from collapsing during fabrication. The support beams start at 1 μm and then narrow to 280 nm (the waveguide width) to prevent excessive transmission loss. Roughly 1% of the total transmission is lost into the support waveguides. A source is placed within the multimode waveguide to calculate the effective indices of the propagating modes.

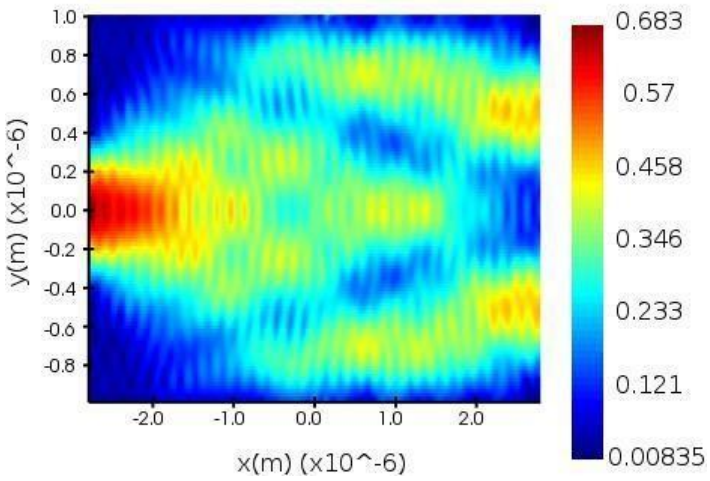

Figure 4.13. Electric field profile of the 1x2 MMI.

The electric field profile of the 1x2 MMI reveals the symmetry of the design about the x-axis (Figure 4.13). The splitting ratio is always 0.5, so the purpose of geometrical optimisation is to reduce transmission loss, and to reduce the variation in transmission loss under perturbations in the geometry of the device. The best multimode waveguide length for the 1x2 MMI is found to be 5.6 µm, with a transmission loss of 0.11 dB (Eq. 4.2).

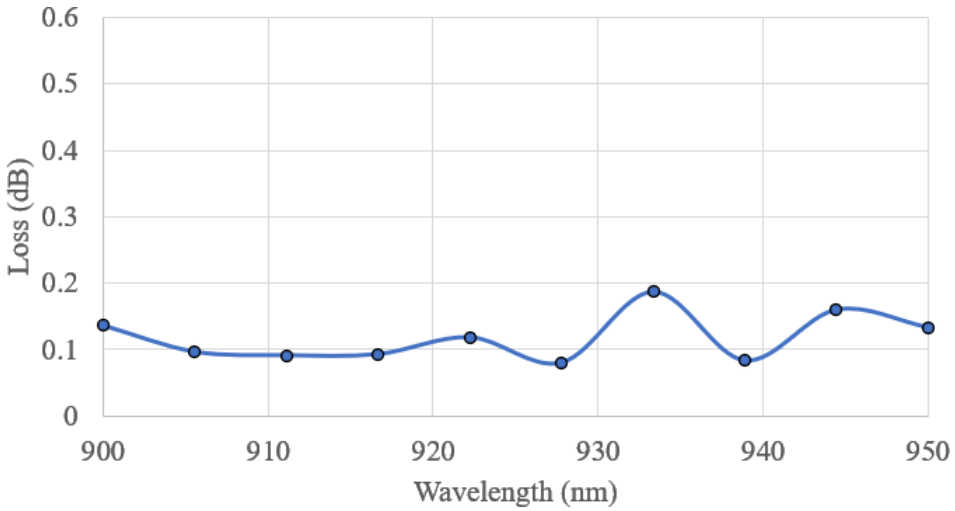

Figure 4.14. 1x2 MMI transmission loss versus wavelength of input light.

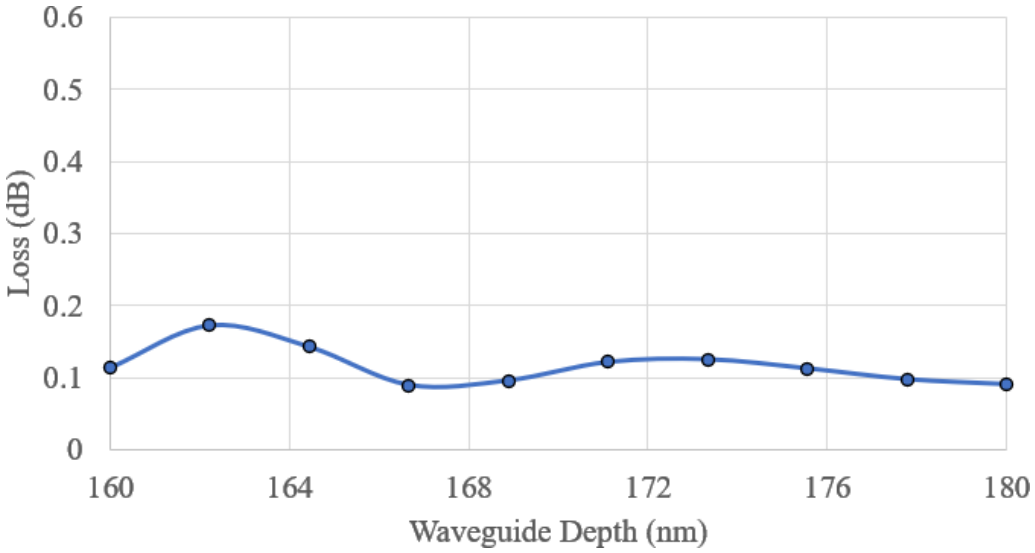

Figure 4.15. 1x2 MMI transmission loss versus waveguide depth.

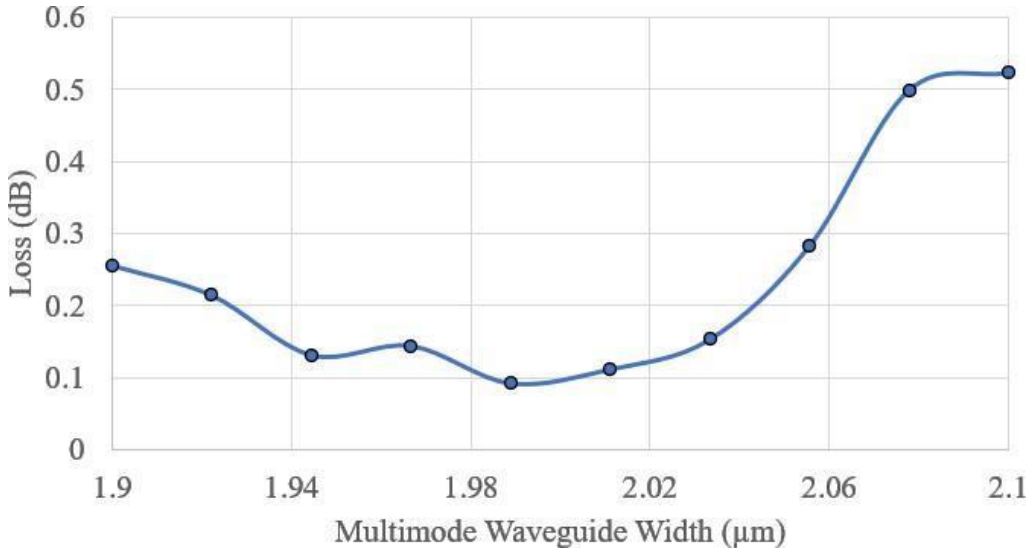

Figure 4.16. 1x2 MMI transmission loss versus multimode waveguide width.

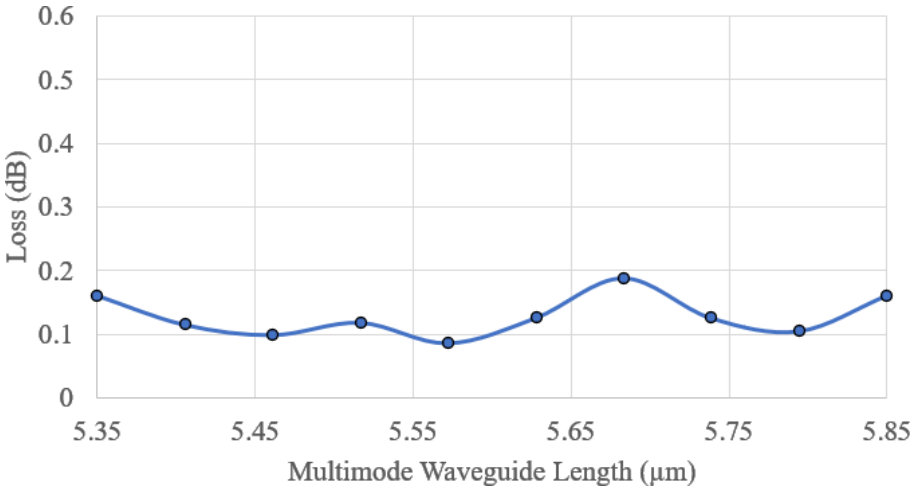

Figure 4.17. 1x2 MMI transmission loss versus multimode waveguide length.

For figures 4.14 to 4.17, the central values are the constants (wavelength = 925 nm, waveguide depth = 170 nm, multimode waveguide width = 2.0 µm, multimode waveguide length = 5.6 µm). Sweeping through the wavelength range, the transmission loss of the 1x2 MMI remains below 0.2 dB (Figure 4.14). The same is true for subtle changes in the waveguide depth (Figure 4.15). A 5% change in the multimode waveguide width (Figure 4.16) sees a more significant increase in transmission loss than a similar percentage change in the multimode waveguide length (Figure 4.17).

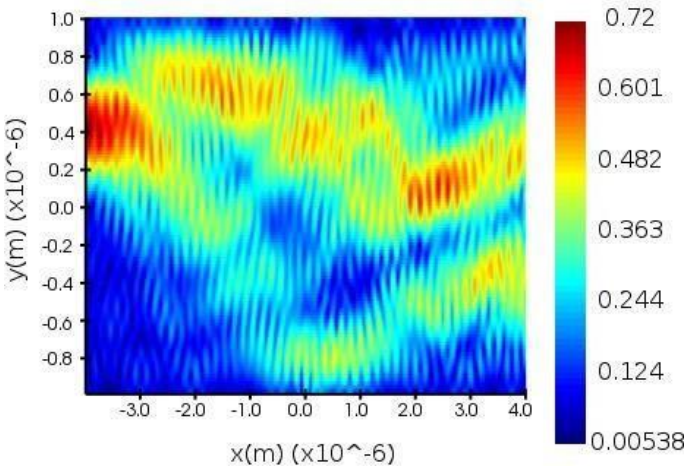

Figure 4.18. Electric field profile of the 2x2 MMI.

Unlike the 1x2 MMI, the electric field profile of the 2x2 MMI is asymmetrical about the x-axis. Consequently, both the splitting ratio and the transmission loss should be carefully considered when designing the device (Figure 4.18). The tapers are slightly narrower for the 2x2 MMI, as this reduces transmission loss. The best multimode waveguide length for the 2x2 MMI is found to be 8 µm, with a splitting ratio of 0.51 and a transmission loss of 0.40 dB (Eq. 4.2). The transmission loss is higher for the 2x2 MMI than for the 1x2 MMI, because it is difficult to balance an even splitting ratio with good transmission. The self-image length is calculated to be 8.37 µm (using Eq. 4.4) and 8.04 µm (using Eq. 4.6). Therefore, calculating the effective width of the multimode waveguide provides a more accurate prediction of the self-image length, giving an overestimate of just 0.5%.

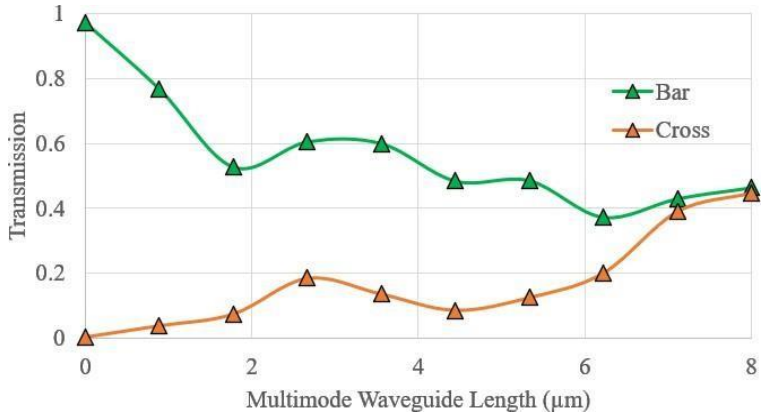

Figure 4.19. Transmission versus wavelength for the upper right (bar) and lower right (cross) output waveguides of the 2x2 MMI.

At a multimode waveguide length of zero, the light travels from the upper left input waveguide to the upper right output waveguide. If this length becomes non-zero, the light interference within the multimode waveguide causes the light to split into two channels. As this length increases, a greater portion of input light is transferred to the lower right output waveguide, until the light is split evenly at the self-image length of 8 µm (Figure 4.19).

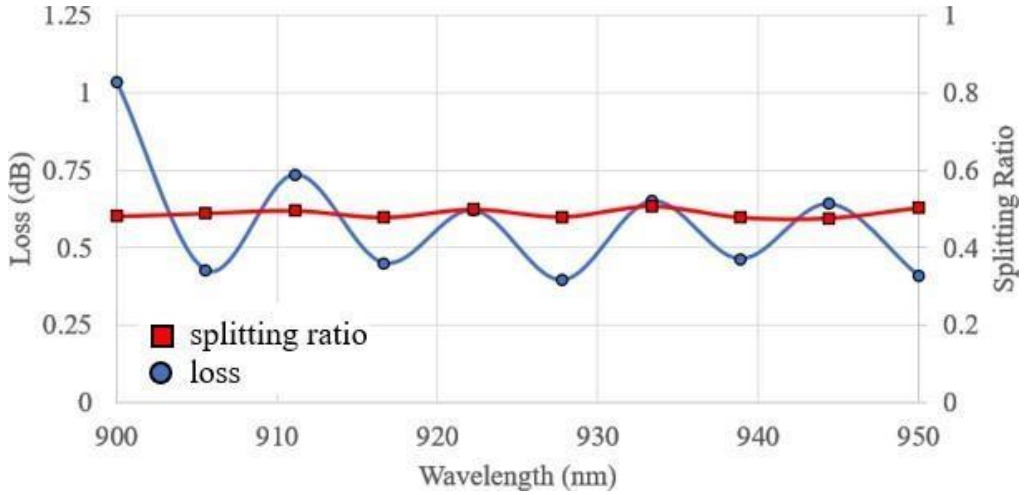

Figure 4.20. 2x2 MMI splitting ratio and transmission loss versus wavelength.

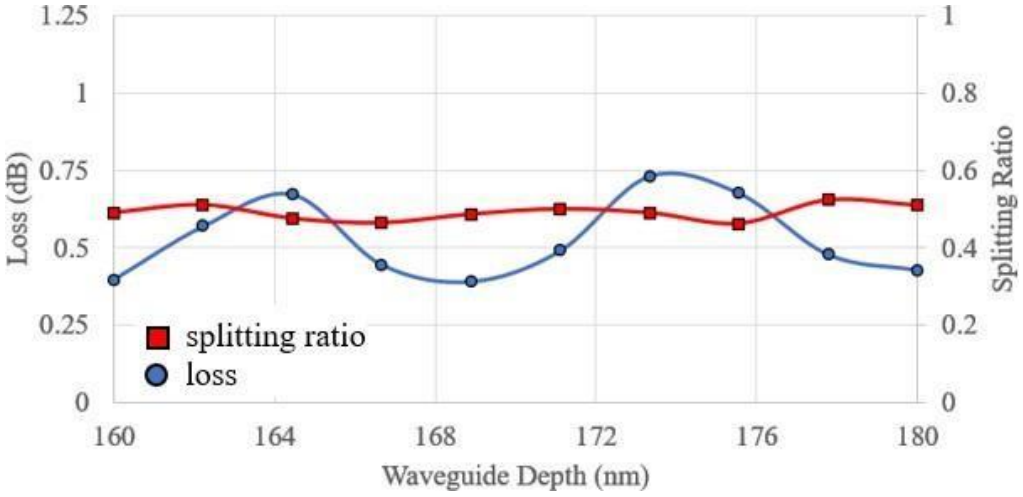

Figure 4.21. 2x2 MMI splitting ratio and transmission loss versus waveguide depth.

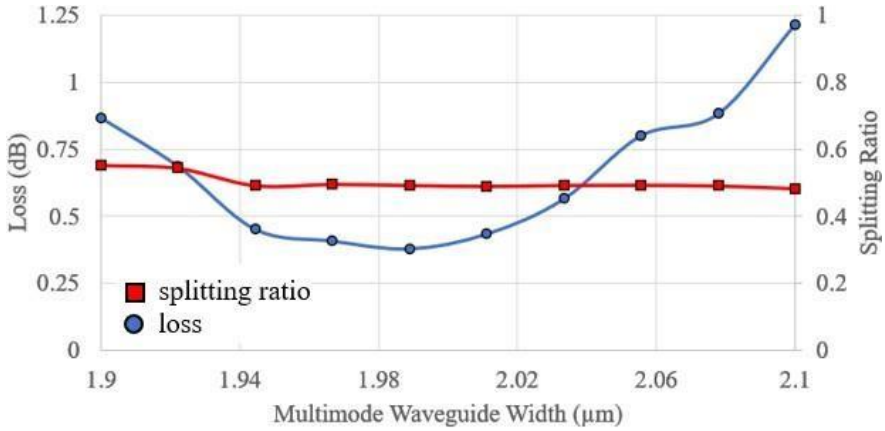

Figure 4.22. 2x2 MMI splitting ratio/transmission loss over multimode waveguide width.

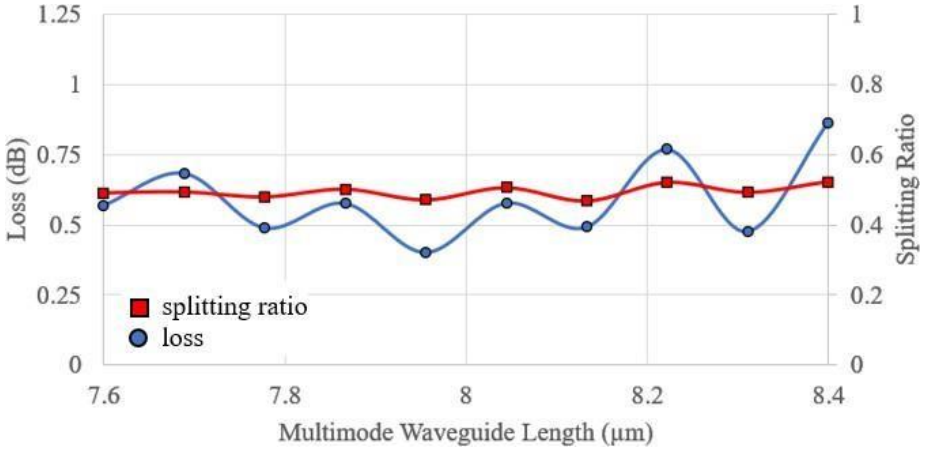

Figure 4.23. 2x2 MMI splitting ratio/transmission loss over multimode waveguide length.

For figures 4.20 to 4.23, the central values are the constants (wavelength = 925 nm, waveguide depth = 170 nm, multimode waveguide width = 2.0 µm, multimode waveguide length = 8.0 µm). Results are presented for parameter variations of the 2x2 MMI: wavelength of input light (Figure 4.20), waveguide depth (Figure 4.21), multimode waveguide width (Figure 4.22), multimode waveguide length (Figure 4.23). Although the transmission loss increases as the parameters are varied, the splitting ratio remains close to 0.5 throughout all the changes. Altering the multimode waveguide width has the biggest impact on transmission.

		W (nm)	S (nm)	L_{DC} (µm)	Loss (dB)	SR
DC		220	140	6.7	0.18	0.502
	W_{MMW} (µm)	W_T (nm)	S_T (nm)	L_{MMW} (µm)	Loss (dB)	SR
1 x 2 MMI	2	775	150	5.6	0.11	0.500
2 X 2 MMI	2	700	150	8.0	0.40	0.492

Table 4.1. Transmission loss and splitting ratio of the beamsplitter devices. W is the waveguide width of the DC. S is the waveguide separation of the DC. L_{DC} is the length of the DC. Loss is the transmission loss at a wavelength of 925 nm. SR is the splitting ratio at a wavelength of 925 nm. W_{MMW} is the width of the multimode waveguide. W_T is the maximum width of the tapered waveguides. S_T is the minimum separation between the tapered waveguides. L_{MMW} is the length of the multimode waveguide.

The properties of the beamsplitter devices are summarised in Table 4.1. Both DCs and MMIs are suitable for photonic applications, each having their benefits and shortcomings which will influence their selection. DCs have a simpler geometry and do not require waveguide tapering, making the fabrication process easier. However, the splitting ratio is highly sensitive to changes in coupling length, wavelength, waveguide width, waveguide separation, and waveguide depth. Therefore, it is wise to operate a DC using a narrow bandwidth source, keeping in mind that slight fabrication inaccuracies will impact the performance. The symmetry of the 1x2 MMI gives a guaranteed splitting ratio of 0.5, combined with low transmission loss comparable to the DC. Although the 2x2 MMI suffers higher transmission loss due to being the most difficult design to optimise, it is more robust to parameter variations than the DC, indicated by the stability of the splitting ratio.

4.3 Characterisation with broadband light

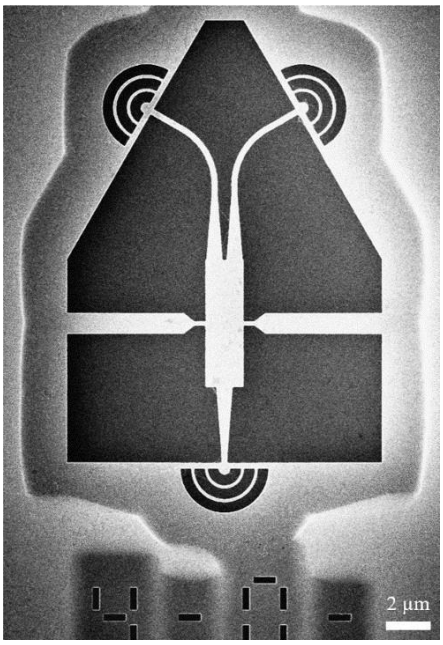

Figure 4.24. SEM of a 1x2 MMI with circular grating outcouplers. Each device is labelled by two etched digits as row-column.

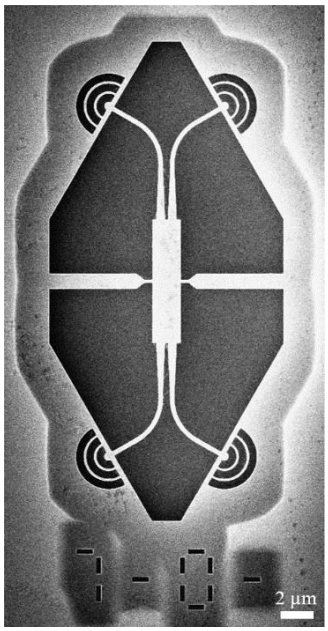

Figure 4.25. SEM of a 2x2 MMI with circular gating outcouplers.

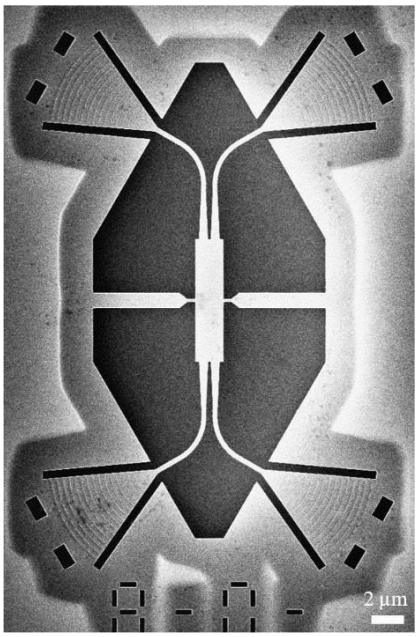

Figure 4.26. SEM of a 2x2 MMI with shallow-etched grating outcouplers.

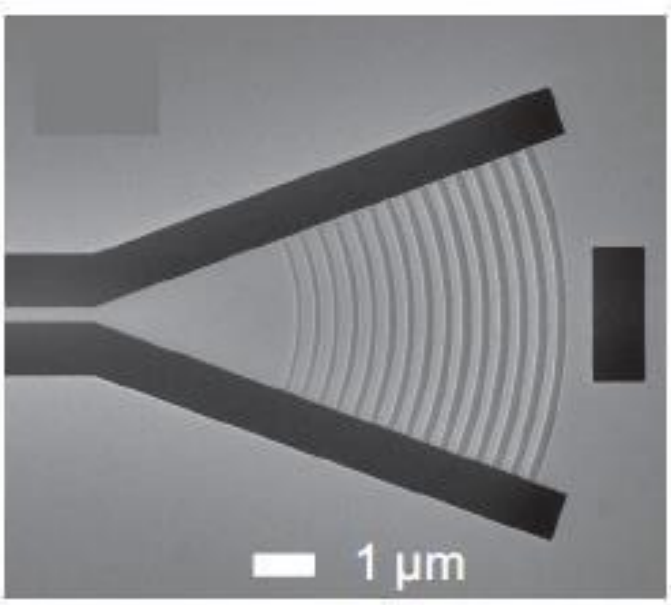

Figure 4.27. SEM of a shallow-etched grating outcoupler [84].

After completing the optimization of the MMI devices using FDTD, I use Python to create the final devices ready for patterning with EBL. I write a script that combines various geometrical objects to form these structures. Next, arrays of duplicates are created with subtle parameter deviations to account for fabrication inaccuracies. This final script is exported to VOYAGER (the software used for EBL), providing a visual display of all the devices, ready for patterning.

The sample is fabricated on a GaAs wafer, with SEMs taken of the three different types of MMI devices: a 1x2 MMI with circular grating outcouplers (Figure 4.24), a 2x2 MMI with circular grating outcouplers (Figure 4.25) and a 2x2 MMI with shallow-etched grating outcouplers (Figure 4.26). Shallow etched grating outcouplers have previously been implemented on GaAs nanomembranes, demonstrating high fibre-coupling efficiency with greatly suppressed back-reflection (Figure 4.27). They use fine ridges to diffract the waveguide propagating mode upwards at an angle close to vertical [84].

Each type of MMI device is repeated in 5x5 arrays with different parameters. Horizontally, the multimode waveguide width (W_{MMW}) changes by a maximum of ± 0.4 μm in steps of 0.2 μm. Vertically, both the taper width (W_T) and the taper separation (S_T) change by a maximum of ± 10 nm in steps of 5 nm, so maximum W_T is combined with minimum S_T. The experimental setup is the same as Section 3.3, but with the broadband light source filtered for 800 nm to 1 μm wavelengths. An optical fibre directs the light onto the bottom outcoupler of the 1x2 MMI, or the bottom left outcoupler of the 2x2 MMI. The light travels through the input waveguide, reaching the multimode waveguide, where interference occurs, splitting the light into two output waveguides. Optical fibres collect the light from

the top left and the top right outcouplers, sending the light to a spectrometer, recording its intensity and wavelength.

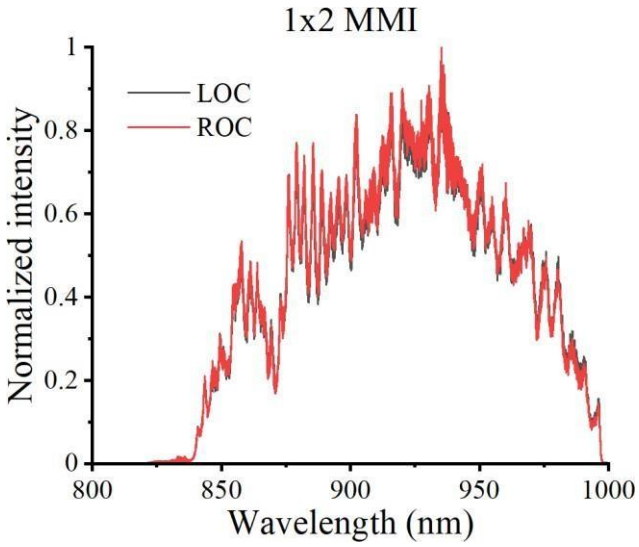

Figure 4.28. Intensity versus wavelength of broadband light transmission through a 1x2 MMI with circular grating outcouplers, where LOC is collection from the left outcoupler, and ROC is collection from the right outcoupler.

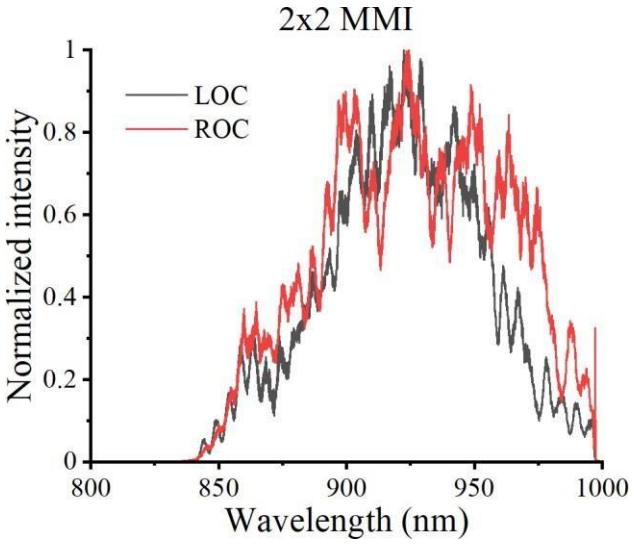

Figure 4.29. Intensity versus wavelength of broadband light transmission through a 2x2 MMI with circular grating outcouplers.

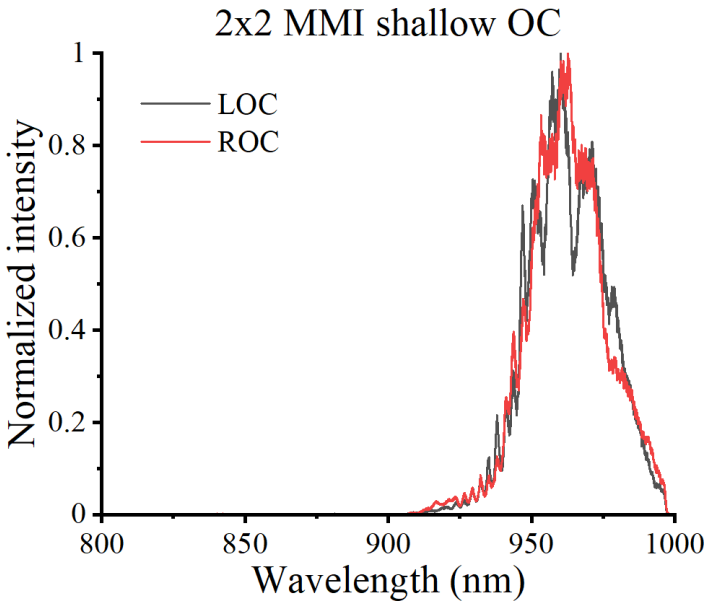

Figure 4.30. Intensity versus wavelength of broadband light transmission through a 2x2 MMI with shallow-etched grating outcouplers.

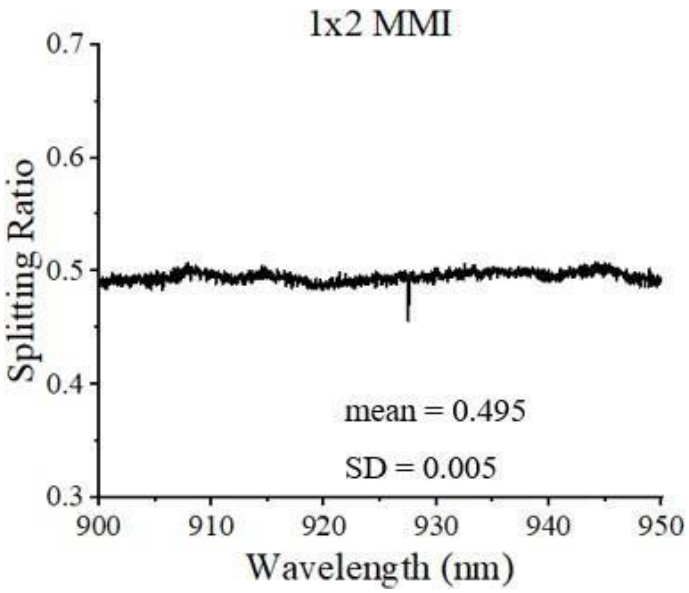

Figure 4.31. Splitting ratio versus wavelength of broadband light transmission through a 1x2 MMI with circular grating outcouplers, showing the mean splitting ratio and standard deviation of the splitting ratio.

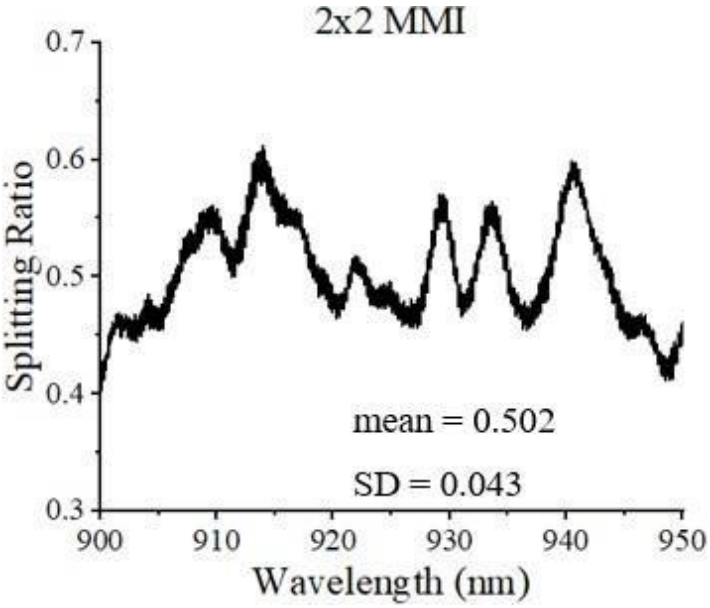

Figure 4.32. Splitting ratio versus wavelength of broadband light transmission through a 2x2 MMI with circular grating outcouplers.

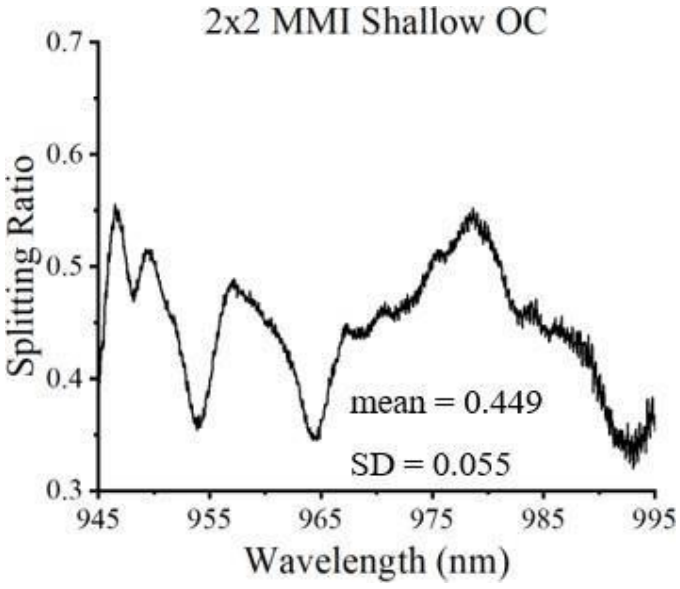

Figure 4.33. Splitting ratio versus wavelength of broadband light transmission through a 2x2 MMI with shallow-etched grating outcouplers.

Results are presented for the best devices, using normalized intensity to account for differences in power and exposure time across the measurements. Both the 1x2 MMI (Figure 4.28) and the 2x2 MMI (Figure 4.29) operate at the same wavelength region: centred on 925 nm, with good transmission between 875 nm to 975 nm. The 2x2 MMI with shallow-etched grating outcouplers has a much narrower operating region, that is red-shifted: 945 nm to 995 nm, centred on 970 nm (Figure 4.30).

A MATLAB script is used to calculate the splitting ratio at each wavelength, alongside the mean splitting ratio and the standard deviation in the splitting ratio. The 1x2 MMI has by far the smallest standard deviation in the splitting ratio, expected since the symmetry of the device should guarantee even splitting of light (Figure 4.31). For the 2x2 MMI, the splitting ratio remains between 0.4 and 0.6 throughout the target wavelength region of 900 to 950 nm, with a mean splitting ratio very close to even at 0.502 (Figure 4.32). When equipped with shallow-etched grating outcouplers, the transmitted wavelengths are red-shifted, with the splitting ratio in this new wavelength region becoming less even (0.502 to 0.449), and the standard deviation increasing (0.043 to 0.055) (Figure 4.33).

In conclusion, a low-loss directional coupler (0.18 dB) was simulated with increased waveguide separation, for better fabrication tolerance, demonstrating even splitting (0.502). A low-loss 1x2 multimode interferometer (0.11 dB) was simulated, demonstrating perfect splitting (0.500), and a low-loss 2x2 multimode interferometer (0.40 dB) was simulated, demonstrating even splitting (0.492). The multimode interferometers were fabricated and tested with broadband light, achieving even splitting for the target wavelength region of 900-950 nm with circular grating outcouplers (1x2 MMI: mean = 0.495, SD = 0.005. 2x2 MMI: mean = 0.502, SD = 0.043).

5 Coupling of Quantum Dots for Superradiance

5.1 Quantum dot registration

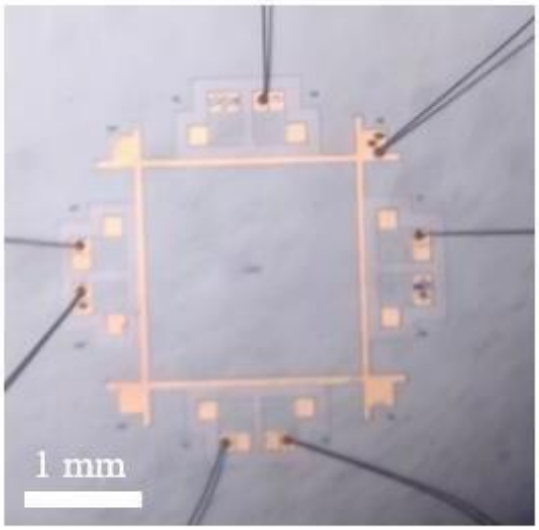

Figure 5.1. Microscope image of the chip used for QD registration. The grey surface is the GaAs wafer, the orange material is the gold contact, and the black wires are the electrical bonds (six diodes and one ground).

As discussed in Section 1.4, deterministic positioning of QDs inside a NBWG is crucial, particularly for experiments that involve coupling of QDs, therefore spectral and spatial matching of QD pairs must be performed with μ-PL (Section 2.2.1). After the best QD pairs have been located, NBWGs can be fabricated around them.

QD registration is performed on a diode chip consisting of a GaAs wafer with InAs QDs (Figure 5.1). The wafer is SF1100, which uses low-growth-rate InAs QDs in a 170 nm depth GaAs waveguide p-i-n structure on an AlGaAs sacrificial layer. The chip has eight diodes around the circumference, two on each side, and six are connected to an external power supply to enhance QD emission. Two of these six diodes are unsuitable for QD registration as the QD emission is too weak. The aim is to pair nearby QDs that have similar emission energies.

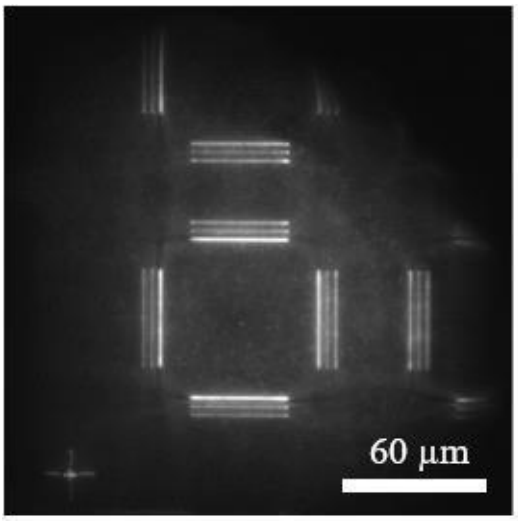

Figure 5.2. µ-PL camera image of a diode, showing the illuminated reference markers and the QDs (tiny white dots).

Each diode has four regions that contain QDs. These are square regions, with markers in the form of three etched lines on each side, enclosing a 60 x 60 µm area of QDs (Figure 5.2). A 10 x 10 µm area is selected for a line scan, revealing the positions of compatible QD pairs. Whether a QD pair is compatible is determined by the proximity of the QDs,

their emission wavelengths, and their linewidths. Compatible QD pairs typically have wavelength differences of 0.1 meV (70 pm) and linewidths of 20 μeV (14 pm).

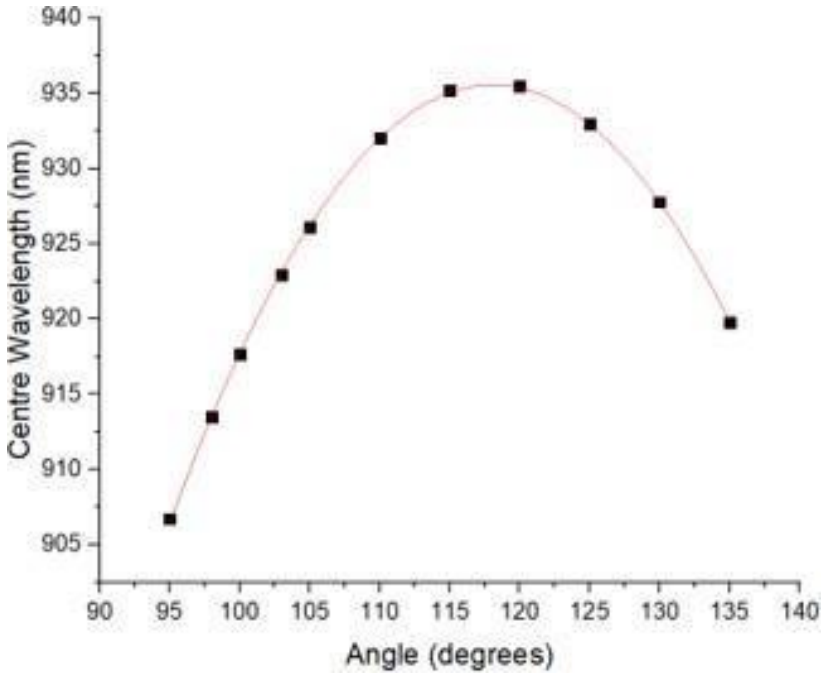

Figure 5.3. Band-pass filter: centre wavelength versus angle with quadratic fit.

When a QD is selected for registration, a 0.5 nm band-pass filter removes nearby emission lines. The angle of this filter is controlled mechanically: as the filter rotates, different wavelengths are filtered. The centre wavelength for a series of filter angles is plotted (Figure 5.3). A quadratic curve is fitted to the data, its equation determining the required filter angle for the QD. The exposure time of the camera is increased from 1 s to 10 s to increase emission intensity, then ten consecutive images are taken for averaging.

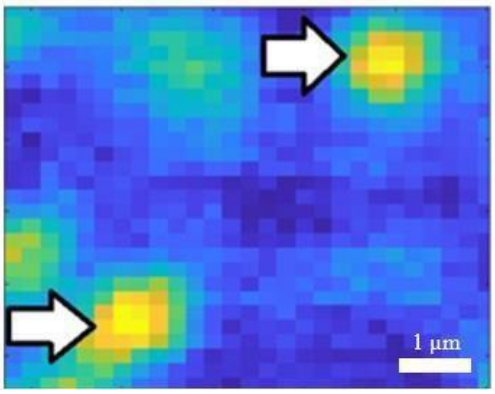

Figure 5.4. µ-PL camera image of a QD pair selected for device fabrication, viewed in MATLAB. Yellow-blue represents highest-lowest intensity.

The QD registration process relies on images captured by a camera with a resolution of 1 pixel = 250 nm. Information on the light intensity at each pixel can be used to determine QD coordinates with a much higher accuracy. Consequently, A MATLAB script can be used for the fitting procedure. Skew is corrected by firstly applying linear fits to the etched markers, then by rotating the image, so the lines are properly oriented (Figure 5.4).

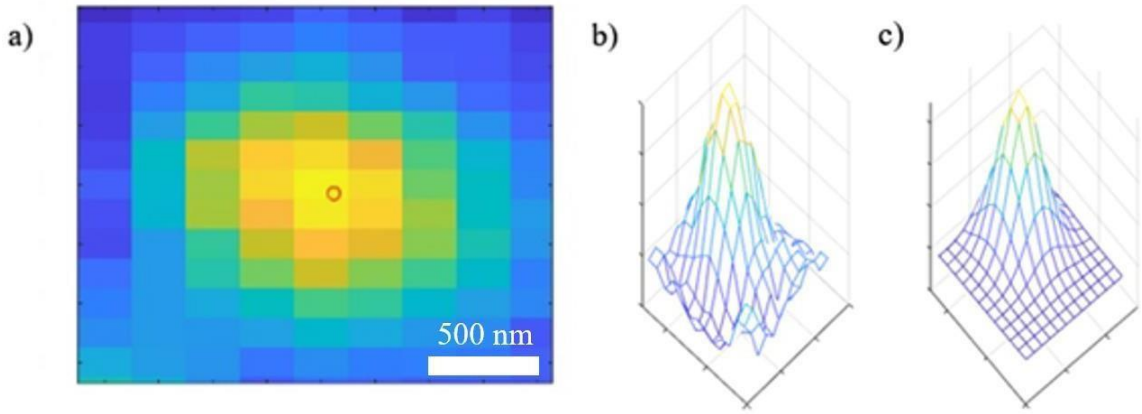

Figure 5.5. Fitting a 2D Gaussian PSF to a QD in MATLAB. a) camera image of the QD: red ring is the emission centre. b) 3D representation of the QD c) 2D Gaussian PSF.

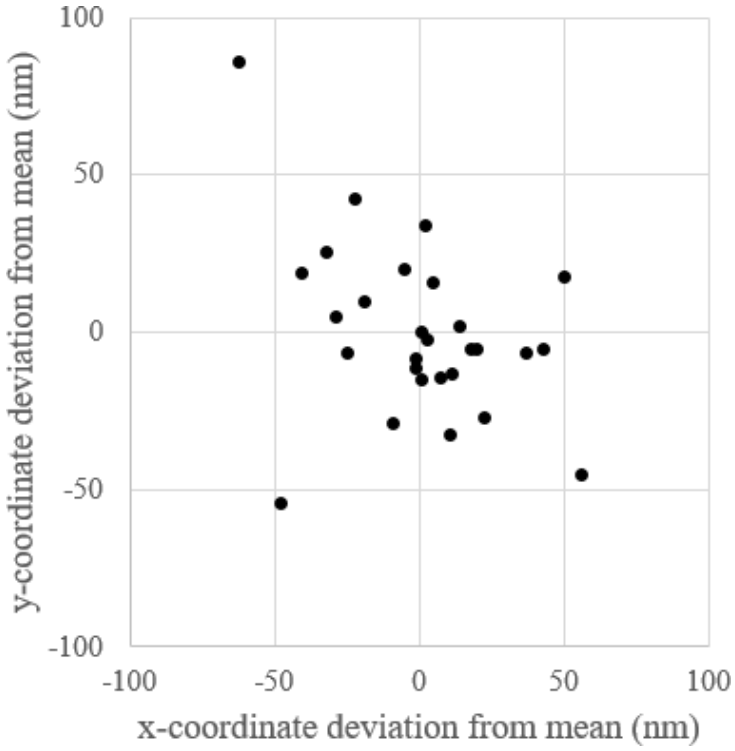

Figure 5.6. How the QD coordinates deviate from their mean values when repeat Gaussian fits are performed. N = 28, unique QDs = 4.

Next, MLE is used (Section 2.2.1), fitting a 2D Gaussian PSF to the QD emission, revealing a more precise position of the QD (Figure 5.5). The error associated with this procedure is calculated by fitting an arbitrary QD, resetting the seed, then fitting the same QD again and so on. This is performed seven times on four unique QDs, extracting the mean positions and the deviations from these means (Figure 5.6). The standard deviation is found to be 28.5 nm in x and 27.9 nm in y.

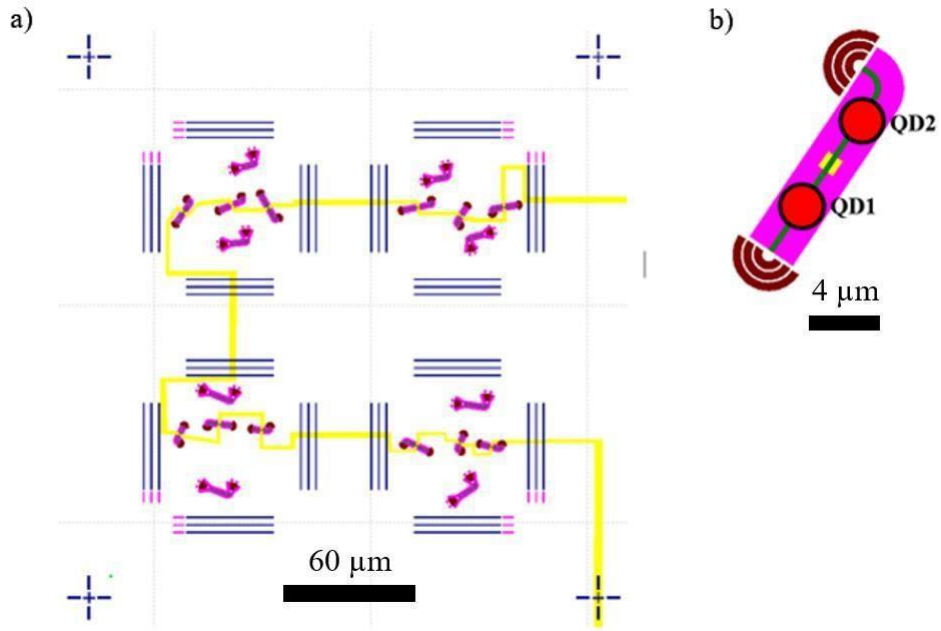

Figure 5.7. NBWGs containing coupled QDs, displayed in VOYAGER. a) A diode of the chip. The yellow line is the electrical contact. b) A circular grating outcoupler NBWG containing two QDs. The yellow square is the etch for the electrical contact. The red circles show the rough positions of each QD.

A NBWG is designed around each QD pair (120 of them), such that the QDs are contained within the waveguide and separated by the electrical contact (Figure 5.7). The QDs are always labelled left to right, so QD2 is to the right of QD1. This design permits the magnetic field tuning of the QD pairs for two-QD resonant coupling experiments.

5.2 Temporal dynamics of coupled quantum dots

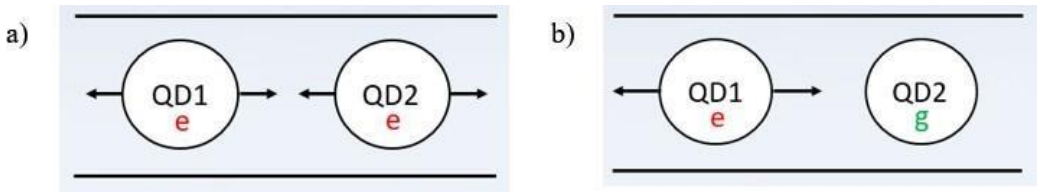

Figure 5.8. Illustrations of two QDs in a waveguide. a) Both QDs in the excited state. b) QD1 in the excited state and QD2 in the ground state. Arrows show emission direction.

Preceding superradiance measurements on NBWGs containing coupled QDs, it is necessary to understand the temporal dynamics of the system, therefore I use QuTiP to investigate this (Section 2.1.3). The QDs emit photons of 925 nm wavelength, with a perfect beta factor (no losses into unguided modes). Each QD can be set to begin either in the ground state or the excited state (Figure 5.8). The temporal dynamics can be calculated for the excited state of each QD, the ground state of each QD, the bright Dicke state of the system (superradiance, Section 1.7, Eq. 1.6), and the dark Dicke state of the system (subradiance, Section 1.7, Eq. 1.7). Each state is quantified by its expectation level (or probability P), where $0 \leq P \leq 1$, describing the likelihood of the QD being in that state.

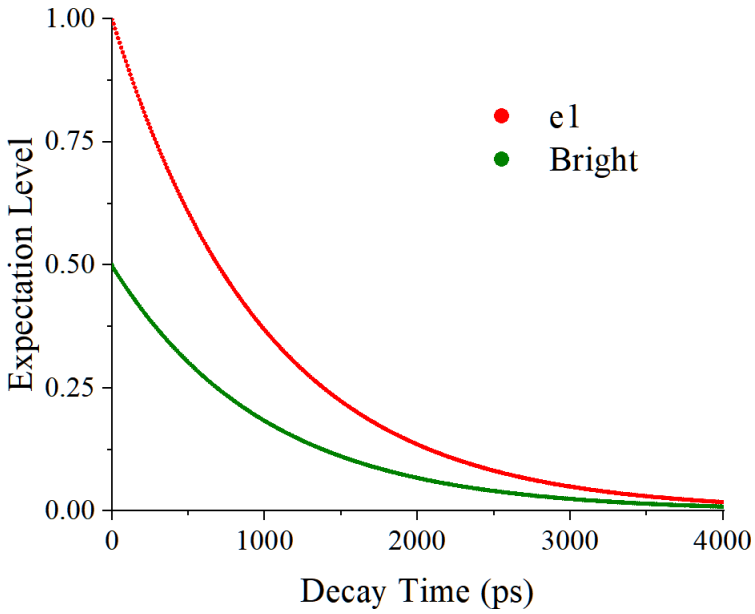

Figure 5.9. Temporal dynamics of a single QD in the excited state, where "e1" is the excited state of the QD and "Bright" is the superradiant state of the system.

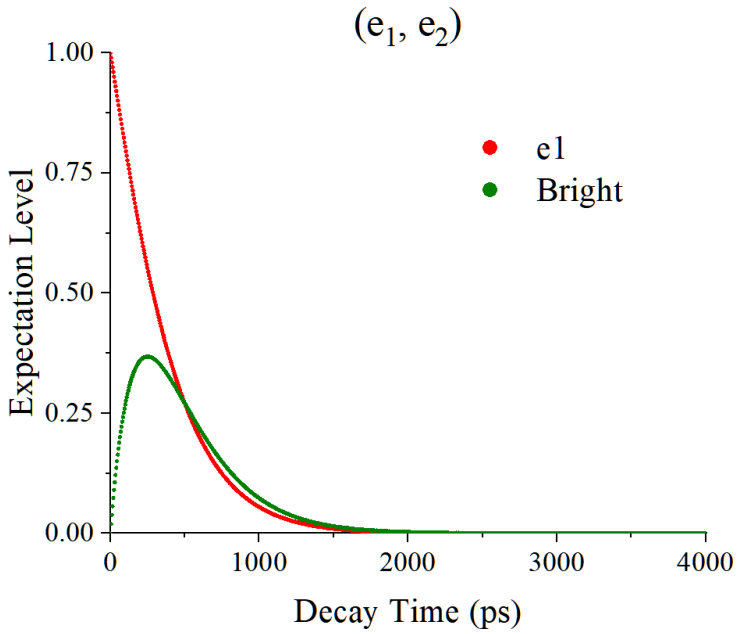

Figure 5.10. Temporal dynamics of coupled QDs in which both QDs begin in the excited state.

By setting one QD to the ground state with total loss into unguided modes, the system is now simply one QD in the excited state (Figure 5.9). If the energy constant of the left-propagating photon is set to zero, the excited QD decays into the right channel, the QD lifetime revealed by the temporal change of the excited state's population. The excited state starts at an expectation level of one, then exponentially decays to zero. The lifetime of the QD is determined by the decay time at an expectation level equal to exp(-1) = 0.368. This is found to be 1 ns (as expected), since the QD decay rate is set to 1 ns^{-1}. The bright state starts at an expectation level of 0.5, then exponentially decays to zero. At 1 ns, the expectation level of the bright state equals 0.5* exp(-1), therefore the bright state is always equal to half the excited state, and decays at the same rate as the excited state. The dark state behaves identically to the bright state.

By setting each QD to the excited state and enabling decay in both directions, a non-chiral, coupled QD system is initiated, with the lifetime of each QD now halved (Figure 5.10). The excited states decay identically, faster than the single QD case, with a decay time of approximately 395 ps at an expectation level equal to exp(-1). Since bi-directional decay halves the lifetime of each QD, this corresponds to a decay rate enhancement of roughly 1.25. The bright state takes a parabolic shape, peaking at a decay time of 250 ps (half of the new QD lifetime) with an expectation level equal to exp(-1). The dark state remains at zero. If chirality is introduced, equally and oppositely to each QD, the decay rate of the excited state slows, until it behaves as a single QD system at a chirality of unity.

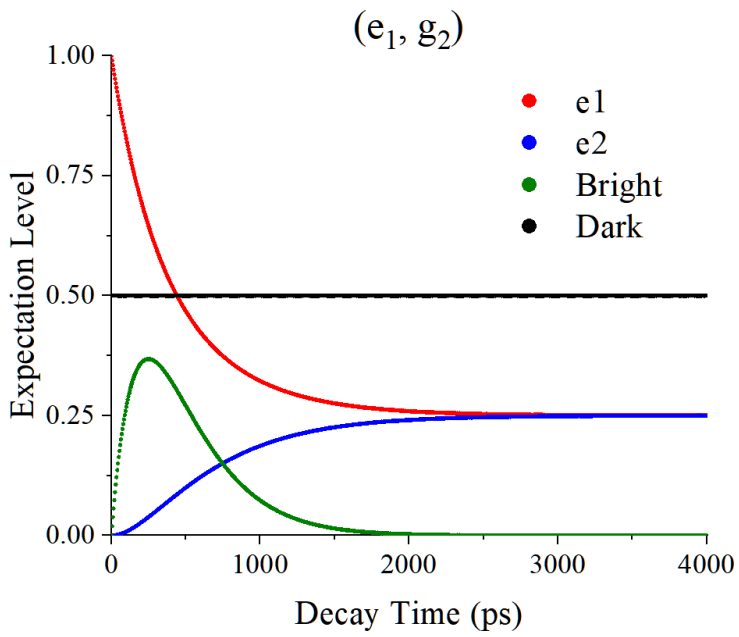

Figure 5.11. Temporal dynamics of coupled QDs in which QD1 begins in the excited state and QD2 begins in the ground state.

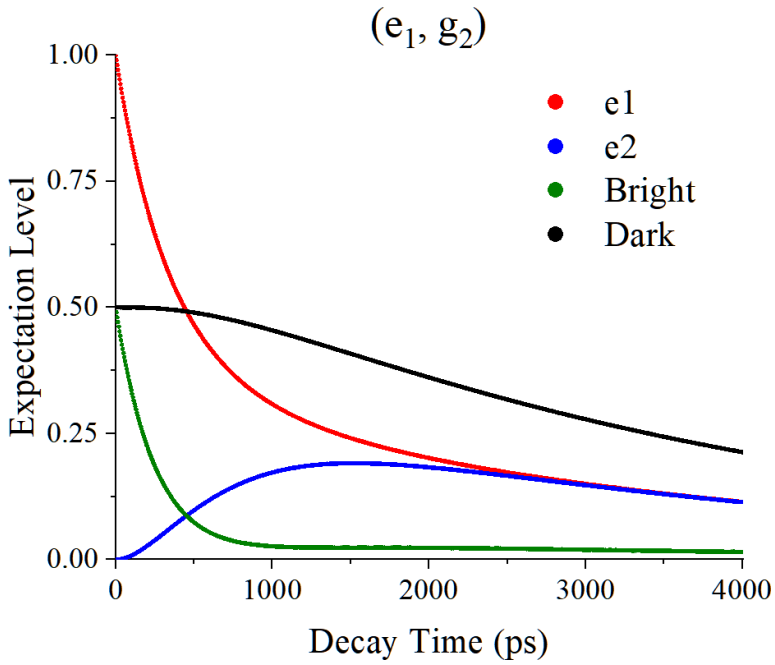

Figure 5.12. Temporal dynamics of coupled QDs in which QD1 begins in the excited state, QD2 begins in the ground state and the QDs are detuned by one linewidth.

By keeping the same settings, except QD2 begins in the ground state, it is now excited by photon emission from the deexcitation of QD1 (Figure 5.11). The expectation levels of the excited states change exponentially until they plateau to a value of 0.25, indicating resonant coupling. The excited state of QD1 decays more slowly than for the previous level configuration, with the decay time equal to approximately 775 ps (roughly half the decay rate found previously). The bright state behaves identically to the previous case. However, the dark state is now non-zero with an expectation level of 0.5, suggesting that subradiance is the mechanism responsible for the resonant coupling.

To investigate the temporal dynamics of detuned QDs, the QD linewidth should be determined, which is approximately 0.454 pm at a wavelength of 925 nm. Then, keeping QD1 in the excited state and QD2 in the ground state, the QDs can be detuned by a single linewidth to observe how the resonant coupling changes (Figure 5.12). The excited states slowly decay to zero alongside the dark state. The bright state now begins at an expectation level of 0.5 and quickly decays to zero (exp(-1) = 75 ps). At 4000 ps, the excited states are at an expectation level of approximately 0.10, lower than the case of no detuning (0.25) but higher than when both QDs are in the excited state with no detuning (zero). So, for a detuning of one QD linewidth, resonant coupling is lost but the excited states decay more slowly than the case of both QDs in the excited state. For a detuning much larger than the QD linewidth, the system behaves identically to the case of a single QD in the excited state, since the model provides no interaction between QDs of vastly different wavelengths.

A QD is sensitive to its local environment, meaning that the optical properties of the QD can be modified by nearby charge states and spin states, due to the Stark effect induced by the electric field of randomly trapped charges. This can generate spectral diffusion,

whereby the emission line of the QD drifts around its central wavelength, producing an effect known as spectral wandering [85].

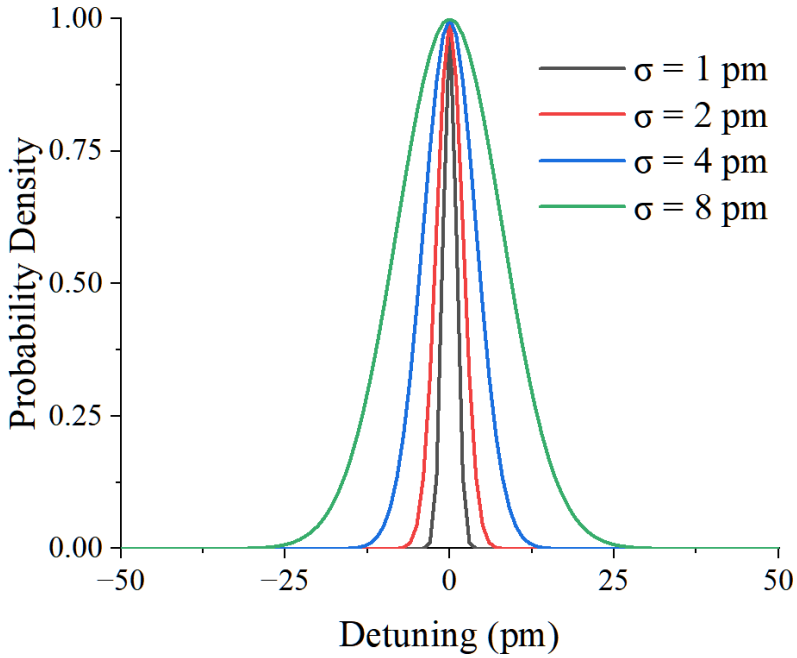

Figure 5.13. Gaussian distributions of detuning for spectral wandering, with different standard deviations.

A Gaussian distribution can be used to simulate spectral wandering for the coupled QDs, given by

$$f(x) = \frac{1}{\sigma\sqrt{2\pi}} e^{-\frac{1}{2}\left(\frac{x}{\sigma}\right)^2} \qquad 5.1$$

where σ is the standard deviation in pm and x is the detuning of QD2 relative to QD1. The emission wavelength of QD1 is fixed at λ = 925 nm, whilst the emission wavelength of QD2 varies at most by ± 50 pm with the probability distribution centred on λ = 925 nm (Figure 5.13).

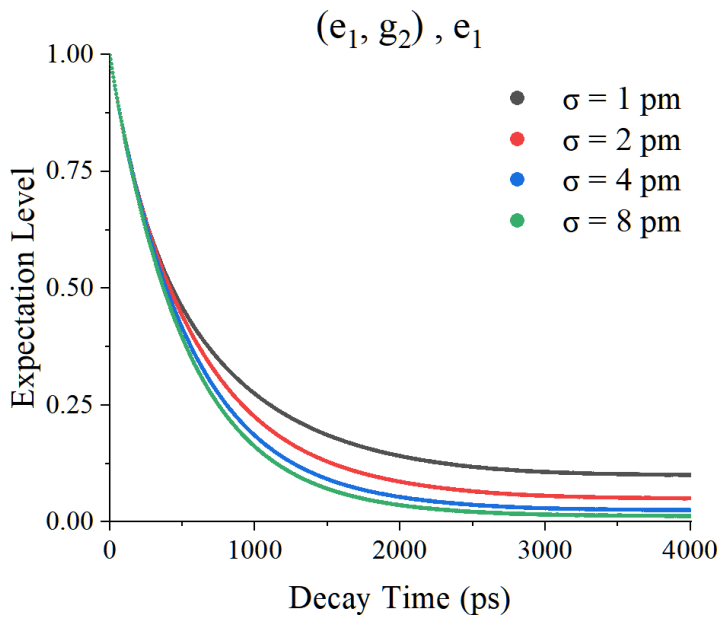

Figure 5.14. Temporal dynamics of the excited state of QD1, in which QD1 begins in the excited state, QD2 begins in the ground state and QD2 experiences spectral wandering.

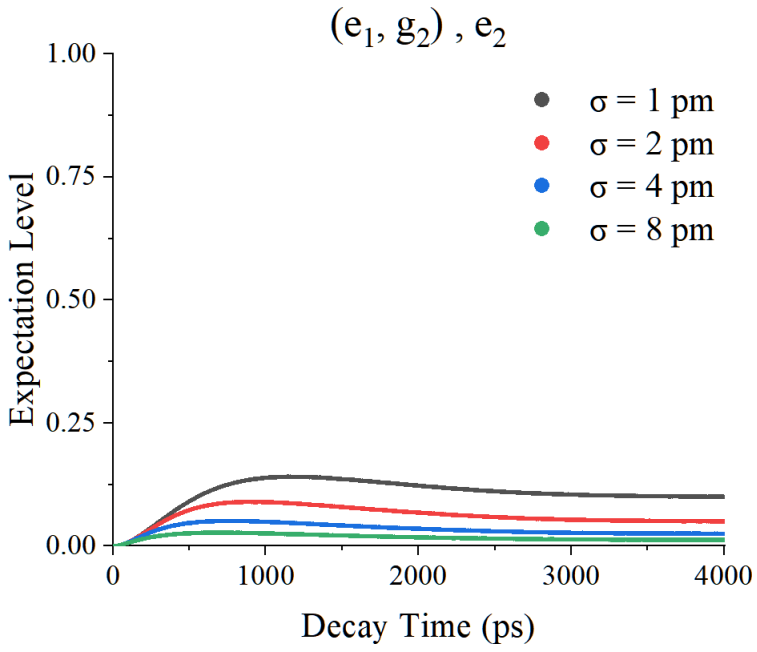

Figure 5.15. Temporal dynamics of the excited state of QD2, in which QD1 begins in the excited state, QD2 begins in the ground state and QD2 experiences spectral wandering.

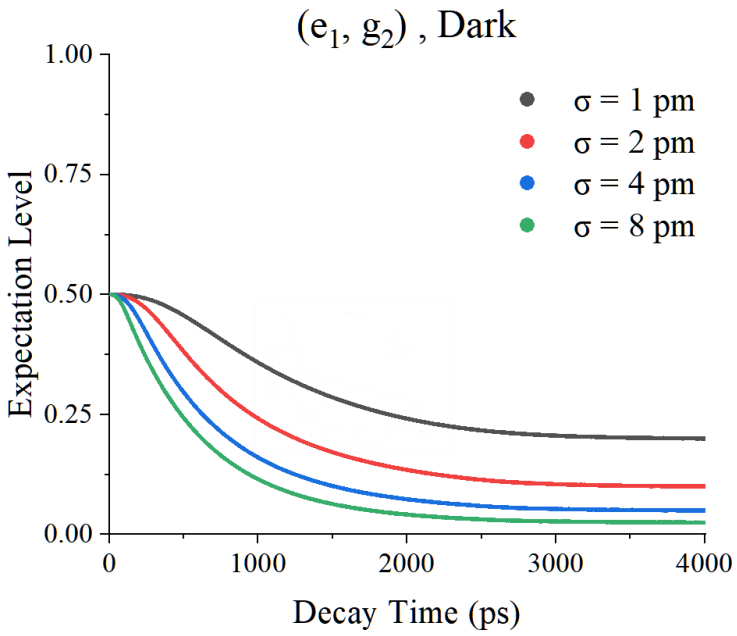

Figure 5.16. Temporal dynamics of the dark state, in which QD1 begins in the excited state, QD2 begins in the ground state and QD2 experiences spectral wandering.

Keeping the previous level configuration, the temporal dynamics are calculated for each point of the Gaussian-distributed QD2 emission wavelength and averaged, revealing the behaviour of the states with spectral wandering (Figure 5.14 to Figure 5.16). Compared to the case of no detuning nor spectral wandering, the states plateau to a lower expectation level, with this expectation level decreasing as the standard deviation increases. Therefore, resonant coupling is attenuated but still present, even for more aggressive spectral wandering. When the standard deviation doubles, the limit of the expectation level halves as the decay time tends to infinity (for the excited state of QD1, $\lim_{t\to\infty} P(\sigma = 1) = 0.1$, $\lim_{t\to\infty} P(\sigma = 2) = 0.05$, $\lim_{t\to\infty} P(\sigma = 4) = 0.025$, $\lim_{t\to\infty} P(\sigma = 8) = 0.0125$).

5.3 Experimental analysis of coupled quantum dots

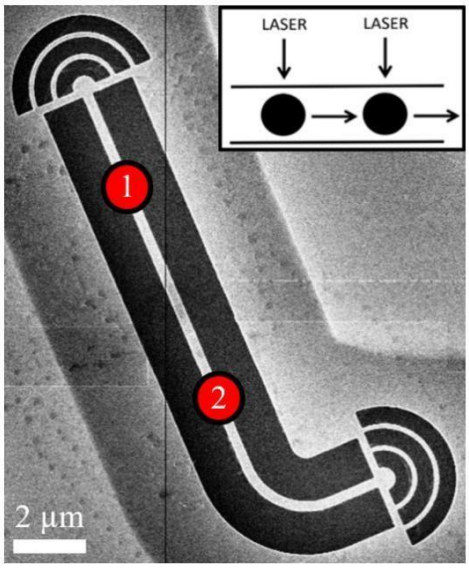

Figure 5.17. SEM of the NBWG containing coupled QDs. The red circles mark the rough positions of QD1 and QD2. The inset shows the principle of excitation for superradiant emission, where the black circles are the QDs and the horizontal arrows show the direction of photonic emission.

QD1 λ (nm)	**QD2 λ (nm)**	**QD1 spec LW (pm)**	**QD2 spec LW (pm)**	**QD1 FPI LW (pm)**	**QD2 FPI LW (pm)**	**QD1+2 FPI LW (pm)**
916.54	916.33	19	17	10.4	6.3	10.4
QD1 left chi	**QD1 right chi**	**QD2 left chi**	**QD2 right chi**	**QD1 abs chi**	**QD2 abs chi**	
+0.54	-0.77	-0.47	+0.47	0.66	0.47	

Table 5.1. Properties of the QDs. λ is the emission wavelength. Spec LW is the linewidth determined by the spectrometer. FPI LW is the linewidth determined by Fabry-Pérot Interferometry. Chi is the chiral contrast. Left/right refers to the top/bottom outcoupler of the NBWG. Abs chi is the absolute average chiral contrast.

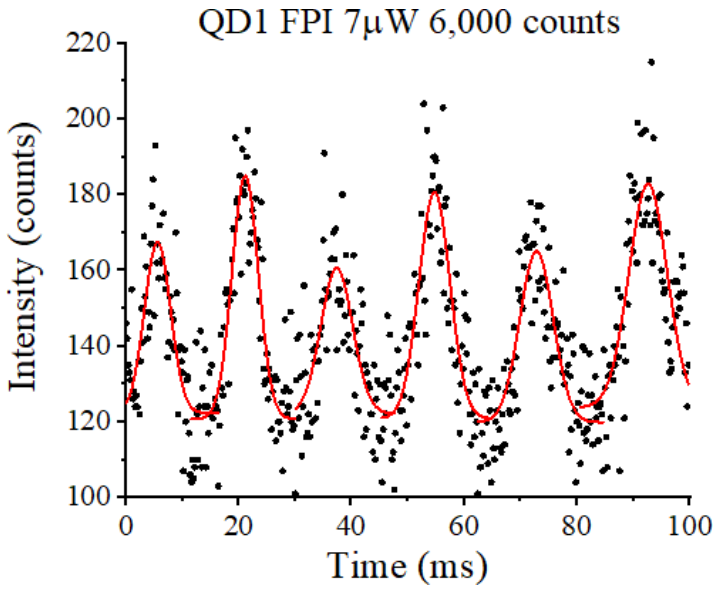

Figure 5.18. FPI of QD1 excited by 7μW of laser power, achieving 6,000 counts on the APD spectrum. Red curves are gaussian fits to the interference fringes.

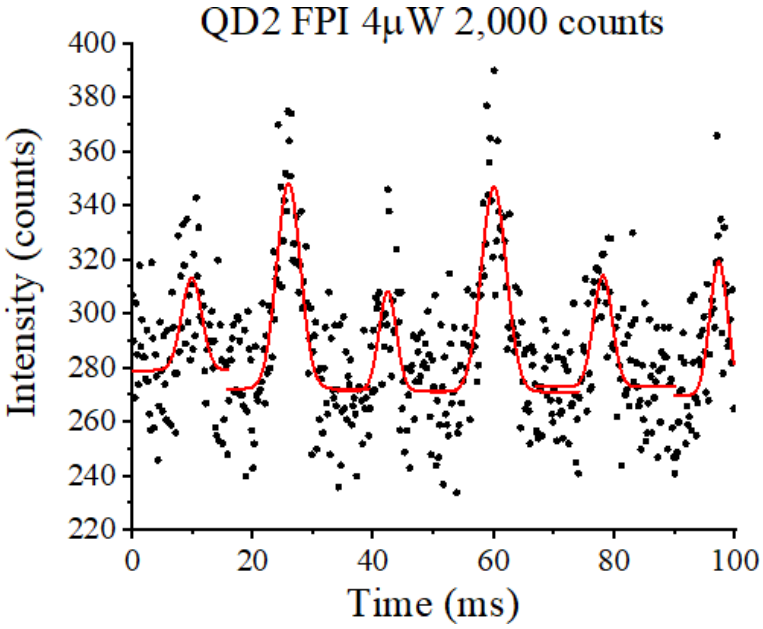

Figure 5.19. FPI of QD2 excited by 4μW of laser power, achieving 2,000 counts on the APD spectrum.

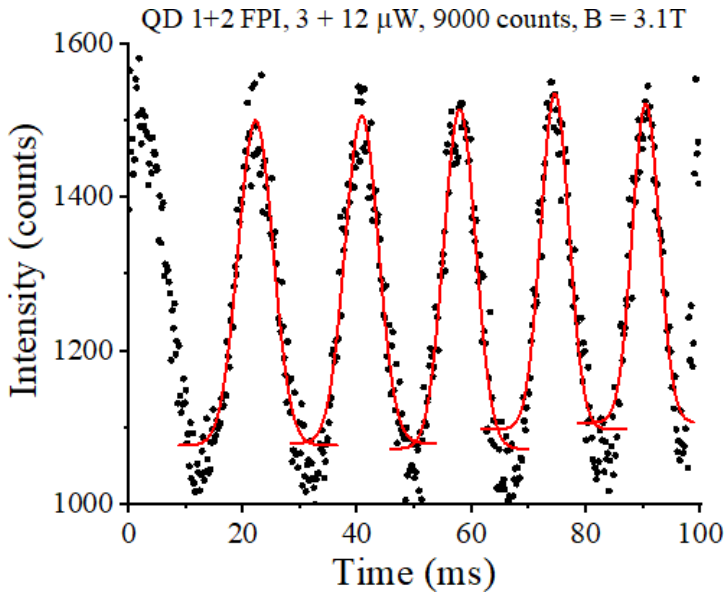

Figure 5.20. FPI of QD1 (excited by 3µW laser power) and QD2 (excited by 12µW laser power), tuned into resonance at a field strength of 3.1 T, achieving 9,000 counts on the APD spectrum.

Post-fabrication, SEMs are taken of the NBWGs containing coupled QDs. The sample is then placed in a helium bath cryostat with a built-in magnet, to enable tuning of the QDs. µ-PL is performed using an 808 nm CW laser, to determine which NBWGs are suitable for further analysis. Some NBWGs contain two QDs with matching emission wavelengths, but these wavelengths do not match the wavelengths recorded in the QD registration process. This could be because the heating/cooling processes undergone in fabrication/instalment shifted the wavelengths of the QDs. The best device is displayed in Figure 5.17, chosen due to the good properties of QD1 and QD2 (Table 5.1): high intensities, narrow linewidths, and emission wavelengths close enough for tuning. The QDs are also somewhat chiral. The device has circular grating outcouplers with a 90° bend in the waveguide when approaching

the right outcoupler, ensuring the device is both compact and well spatially isolated from the other devices. The linewidth of each QD is determined by FPI using an 808 nm CW laser (methodology in Section 2.2.3), with the number of counts on the APD inferring the quality of the measurement (higher counts produce clearer interference fringes). For QD1, the mean linewidth is 10.4 pm, with a standard deviation of 1.5 pm (Figure 5.18). For QD2, the mean linewidth is 6.3 pm, with a standard deviation of 1.0 pm (Figure 5.19). The linewidth of the QD pair is then determined by FPI, performed by first exciting both QDs simultaneously with 808 nm CW lasers until their emission lines are of equal intensity, and then applying a reversable magnetic field to the sample. This temporarily brings the two QD emission lines spectrally closer until they overlap, forming a resonant emission line with double the intensity of a single line. The mean linewidth is 10.4 pm with a standard deviation of 1.1 pm (Figure 5.20). This result hints that the linewidth of the QD pair is limited by the QD with the greatest linewidth.

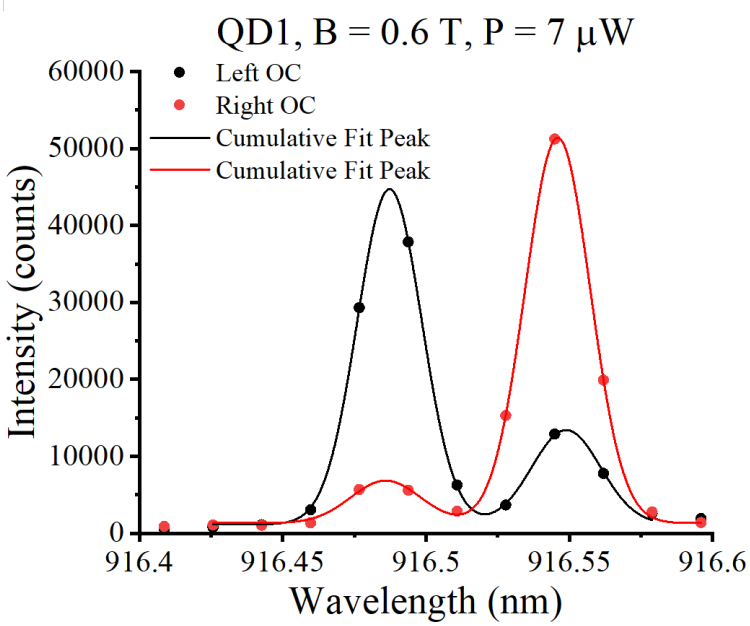

Figure 5.21. Spectra of QD1 collected from each outcoupler, with a weak magnetic field to split the QD states. B is the magnetic field strength and P is the power of the excitation laser. Cumulative Gaussian peaks are fitted to the data points.

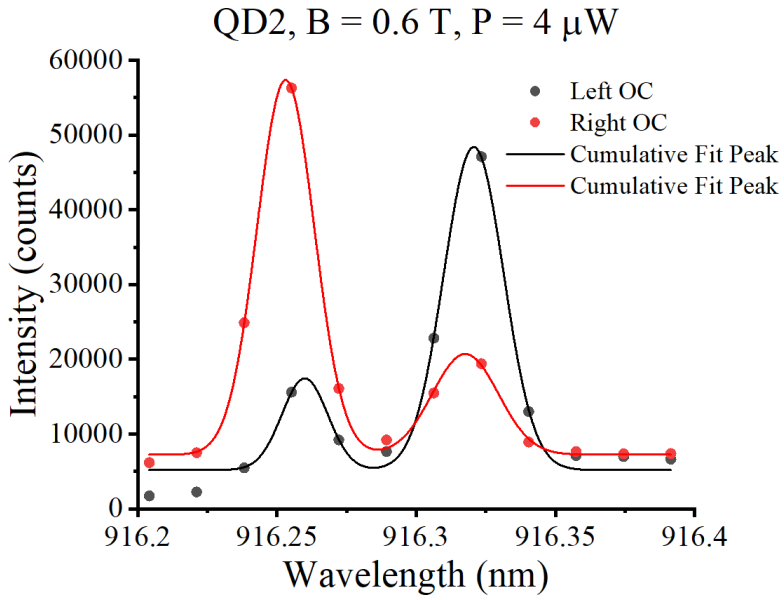

Figure 5.22. Spectra of QD2 collected from each outcoupler, with a weak magnetic field to split the QD states.

Applying a weak magnetic field of 0.6 T to the sample, the emission line of QD1 splits into a pair of lines (the physics of this is explained in Section 1.5). Since the spectral separation of the pair increases linearly with increasing field, and a field of 1 T is determined to correspond to a spectral separation of roughly 100 pm, a 0.6 T field separates the pair by roughly 60 pm (Figure 5.21). This splitting, when photonic emissions are spectrally measured from either outcoupler with a constant excitation power, reveals the chirality of the QD. This measurement is repeated for the second QD, with a lower excitation power needed to reach saturation intensity (Figure 5.22). According to Eq. 1.10, the chiral contrast of QD1 is +0.54 (left outcoupler) and -0.77 (right outcoupler). The same equation finds the chiral contrast of QD2 to be -0.47 (left outcoupler) and +0.47 (right outcoupler). The absolute average chiral contrast is 0.66 for QD1 and 0.47 for QD2 (Eq. 1.11).

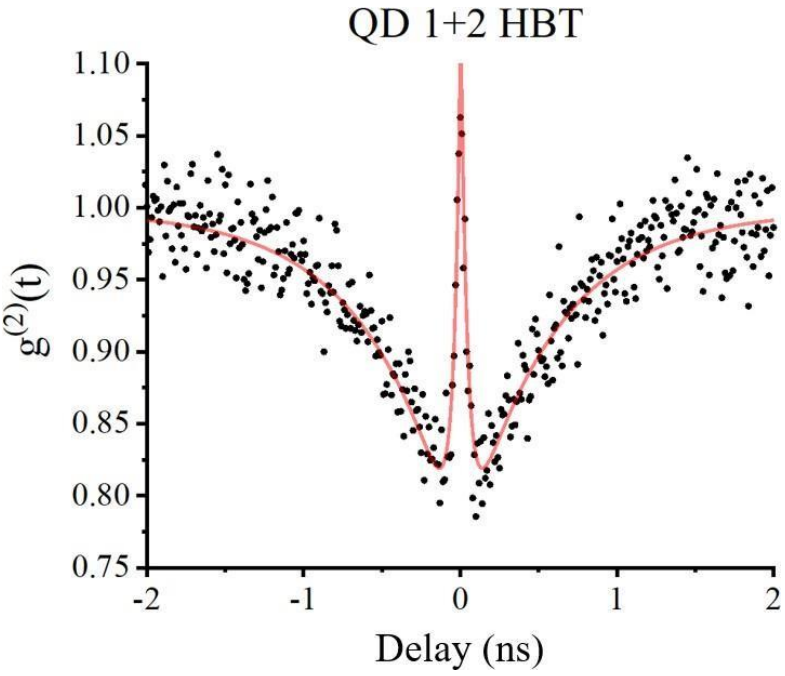

Figure 5.23. HBT of QD1 and QD2 intensity-matched and tuned into resonance by a magnetic field, with a g2 fit.

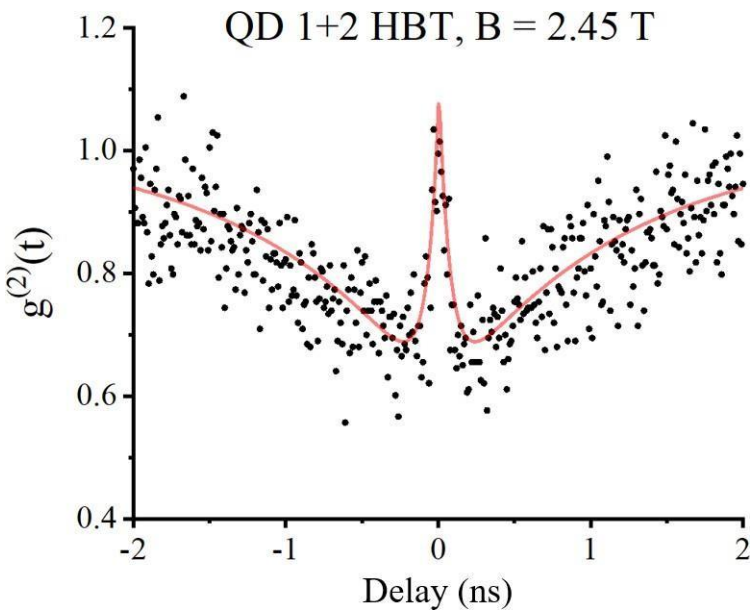

Figure 5.24. HBT of QD1 and QD2 intensity-matched and tuned by the magnetic field at 2.45 T, with a g2 fit.

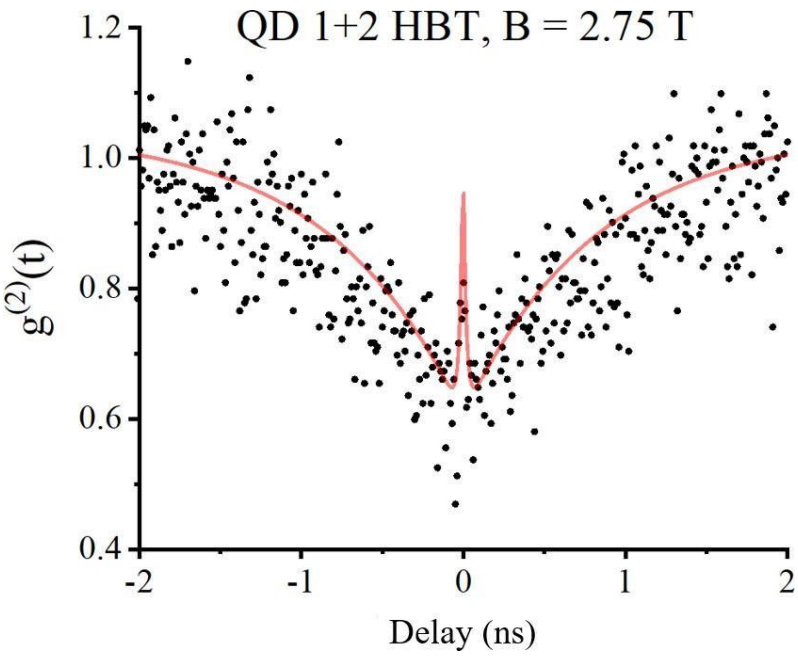

Figure 5.25. HBT of QD1 and QD2 intensity-matched and tuned by the magnetic field at 2.75 T, with a g2 fit.

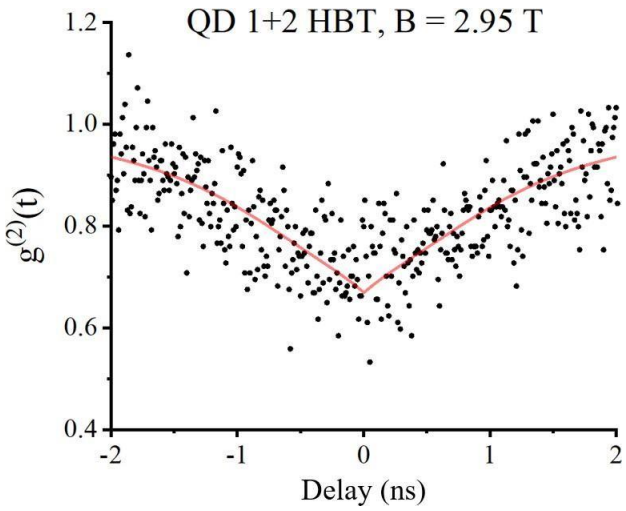

Figure 5.26. HBT of QD1 and QD2 intensity-matched and tuned by the magnetic field at 2.95 T, with a g2 fit.

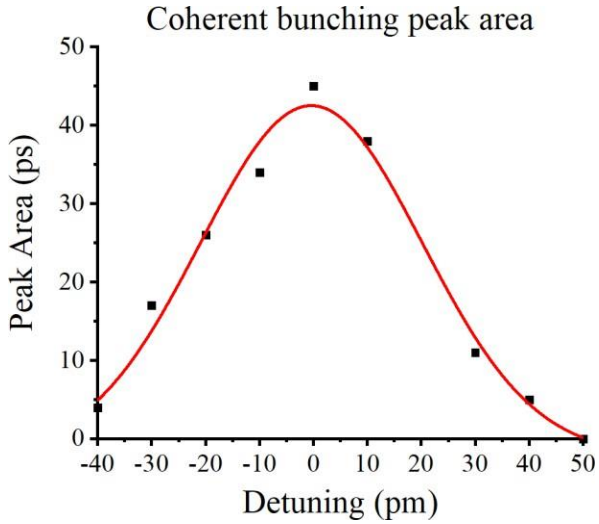

Figure 5.27. The area of the coherent bunching peak versus the spectral separation of the QDs, with a Gaussian fit.

To investigate superradiance, two-photon intensity correlation is performed on the 2QD NBWG via HBT (Section 2.2.2). With QD1 and QD2 intensity matched and tuned into resonance, a sharp coherent bunching peak is obtained for the g2 (Figure 5.23). The curve is fitted using the method outlined in Section 2.1.2.

Because chirality enhances superradiance, the peak surpasses the typical 2QD g2 limit of one (Section 1.7). This is the first observation of superradiance in chirally coupled QDs in a nanophotonic waveguide. Detuning effects are investigated by performing HBT at different magnetic field strengths. With the magnetic field at 2.45 T, the QDs are resonantly coupled, generating a coherent bunching peak (Figure 5.24). Increasing the field by 0.3 T, the coherent bunching peak becomes shorter and narrower (Figure 5.25). Increasing the field by a further 0.2 T, the coherent bunching peak completely vanishes, leaving only the antibunching dip (Figure 5.26). These results match the predictions of the theoretical g2 (Eq. 1.8). The cosine term shifts from one to zero as the detuning increases, making the rest of the second term disappear, leaving only the first term, generating the antibunching dip. For a selection of magnetic field strengths, it becomes apparent that the area of the coherent bunching peak varies in a Gaussian fashion (Figure 5.27). When displayed as the spectral separation of the QDs, the FWHM is 40 pm with an R^2 of 0.98, suggesting the data is highly correlated with a Gaussian fit.

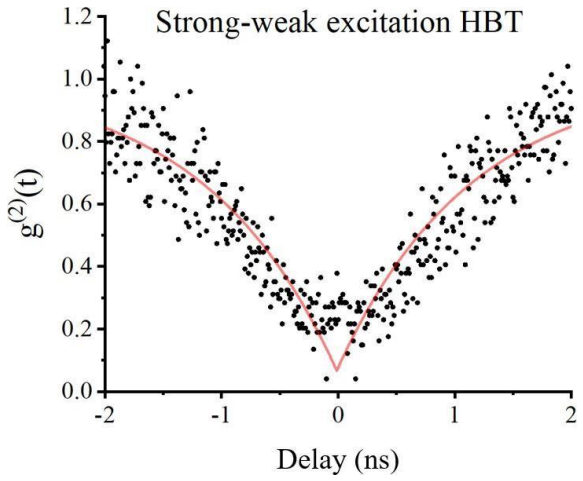

Figure 5.28. HBT of the QDs tuned into resonance, where QD1 is strongly excited and QD2 is weakly excited, with an exponential fit.

The effect of uneven power is investigated by performing HBT with QD1 at saturation and QD2 at a lower intensity (by lowering the power of the excitation laser). In the most extreme case, QD2 is barely switched on, at just 10% the intensity of QD1. The g2 has no coherent bunching peak, with the antibunching dip falling to zero (Figure 5.28). This result agrees with both the experimental and the theoretical result for single QD excitation (Section 1.7: Figure 1.19, Eq. 1.8). The broadness of the antibunching dip determines the lifetime of the QD, so an exponential curve is fitted to the data, in the form

$$g2 = 1 - \exp(-abs(\gamma\tau)) \qquad 5.2$$

where $g2$ is the second-order photon correlation, γ is the decay rate, and τ is the delay time. $1/\gamma$ then gives the lifetime of the QD. A lifetime of 1.1 ns is obtained, which is close to the expected lifetime of 1 ns for InGaAs QDs [29].

To conclude, quantum dot registration was performed, registering 120 QD pairs with similar energies. QuTiP simulations of a waveguide-embedded QD pair were performed, finding resonant coupling is mediated by the dark state, and is attenuated but still present under spectral wandering. 2QD nanobeams were fabricated around the QD pairs, and then characterised by μ-PL, finding a few devices with suitable properties. Fabry-Pérot interferometry was performed on the best device, finding a linewidth of 10.4 pm for QD1 and 6.3 pm for QD2. Hanbury Brown-Twiss interferometry was performed on this device, observing signatures of superradiance from the chirally-coupled QDs. The QDs were detuned using an applied magnetic field, finding the area of the coherent bunching peak disappears for detunings larger than 40 pm. Strong-weak excitation was performed, recreating the antibunching dip in the g2 found by single-QD excitation experiments.

Conclusion

During my three years in LDSD, I have made some contributions to our understanding of III-V semiconductor photonic devices, thanks to the help of others in the group. Firstly, I designed a circular grating outcoupler with an efficiency that surpassed the previous best iteration. Secondly, I constructed compact beamsplitter devices, demonstrating classical interference with even splitting. Perhaps most significantly, I made the first observation of superradiance from chirally coupled QDs in a nanophotonic waveguide.

There are ways to continue my work. The operation of the circular grating outcoupler could be shifted to a shorter/longer wavelength if the dimensions are manipulated. The beamsplitters could produce quantum interference if a QD is used as the light source. Regarding the NBWGs containing coupled QDs, a few options are available. Firstly, the QD registration process could be refined by determining how to retain the original QD emission wavelengths (improving the reliability of the devices), and by using higher quality reference markers (increasing the precision of QD coordinates). Secondly, the QDs could be tuned by an electric field, potentially surpassing the tuning range achieved by the magnetic field. Finally, coupling of three QDs within a NBWG could be explored.

Bibliography

[1] I. L. Chuang and Y. Yamamoto, "Simple quantum computer," *Physical Review A,* vol. 52, no. 5, p. 3489, 1995.

[2] M. Thompson, A. Politi, J. Matthews and J. O'Brien, "Integrated waveguide circuits for optical quantum computing," *IET circuits, devices & systems,* vol. 5, no. 2, pp. 94-102, 2011.

[3] M. Reed, "Quantum dots," *Scientific American,* vol. 268, no. 1, pp. 118-123, 1993.

[4] F. M. Spedalieri, "Quantum key distribution without reference frame alignment: Exploiting photon orbital angular momentum," *Optics communications,* vol. 260, no. 1, pp. 340-346, 2006.

[5] E. Haven, "A Black-Scholes Schrödinger option price: 'bit' versus 'qubit'," *Physica A: Statistical Mechanics and its Applications,* vol. 324, no. 1-2, pp. 201-206, 2003.

[6] J. O'brien, A. Furusawa and J. Vučković, "Photonic quantum technologies," *Nature Photonics,* vol. 3, no. 12, pp. 687-695, 2009.

[7] V. Shchukin and D. Bimberg, "Spontaneous ordering of nanostructures on crystal surfaces," *Reviews of Modern Physics,* vol. 71, no. 4, p. 1125, 1999.

[8] A. Baskaran and P. Smereka, "Mechanisms of stranski-krastanov growth," *Journal of Applied Physics,* vol. 111, no. 4, p. 044321, 2012.

[9] R. Long and P. McIntyre, "Surface preparation and deposited gate oxides for gallium nitride based metal oxide semiconductor devices," *Materials,* vol. 5, no. 7, pp. 1297-1335, 2012.

[10] A. H. Wilson, "The theory of electronic semi-conductors.-ii," *Proceedings of the Royal Society of London. Series A, Containing Papers of a Mathematical and Physical Character,* vol. 134, no. 823, pp. 277-287, 1931.

[11] J. Huang, M. Pfeiffer, A. Werner, J. Blochwitz, K. Leo and S. Liu, "Low-voltage organic electroluminescent devices using pin structures," *Applied Physics Letters,* vol. 80, no. 1, pp. 139-141, 2002.

[12] D. Leonard, M. Krishnamurthy, C. Reaves, S. P. DenBaars and P. M. Petroff, "Direct formation of quantum-sized dots from uniform coherent islands of InGaAs on GaAs surfaces," *Applied Physics Letters,* vol. 63, no. 23, pp. 3203-3205, 1993.

[13] K. Kowalik, O. Krebs, A. Lemaitre, S. Laurent, P. Senellart, P. Voisin and J. A. Gaj, "Influence of an in-plane electric field on exciton fine structure in InAs-GaAs self-assembled quantum dots," *Applied Physics Letters,* vol. 86, no. 4, p. 041907, 2005.

[14] M. Grundmann, O. Stier and D. Bimberg, "InAs/GaAs pyramidal quantum dots: Strain distribution, optical phonons, and electronic structure," *Physical Review B,* vol. 52, no. 16, p. 11969, 1995.

[15] A. J. Nozik, "Spectroscopy and hot electron relaxation dynamics in semiconductor quantum wells and quantum dots," *Annual Review of Physicl Chemistry,* vol. 52, no. 1, pp. 193-231, 2001.

[16] H. Kimble, M. Dagenais and L. Mandel, "Photon antibunching in resonance fluorescence," *Physical Review Letters,* vol. 39, no. 11, p. 691, 1977.

[17] I. Sychugov, R. Juhasz, J. Valenta and J. Linnros, "Narrow luminescence linewidth of a silicon quantum dot," *Physical Review Letters,* vol. 94, no. 8, p. 087405, 2005.

[18] S. Tsukamoto, Y. Nagamune, M. Nishioka and Y. Arakawa, "Fabrication of GaAs quantum wires (∼ 10 nm) by metalorganic chemical vapor selective deposition growth," *Applied Physics Letters,* vol. 63, no. 3, pp. 355-357, 1993.

[19] T. Pregnolato, X. L. Chu, T. Schröder, R. Schott, A. Wieck, A. Ludwig, P. Lodahl and N. Rotenberg, "Deterministic positioning of quantum dots in nanophotonic waveguides," *arXiv preprint arXiv:1907.01426,* 2019.

[20] D. Matthews, H. Summers, P. Smowton and M. Hopkinson, "Experimental investigation of the effect of wetting-layer states on the gain–current characteristic of quantum-dot lasers," *Applied Physics Letters,* vol. 81, no. 26, pp. 4904-4906, 2002.

[21] P. Lodahl, S. Mahmoodian and S. Stobbe, "Interfacing single photons and single quantum dots with photonic nanostructures," *Reviews of Modern Physics,* vol. 87, no. 2, p. 347, 2015.

[22] G. Wang, A. Chernikov, M. M. Glazov, T. F. Heinz, X. Marie, T. Amand and B. Urbaszek, "Colloquium: Excitons in atomically thin transition metal dichalcogenides," *Reviews of Modern Physics,* vol. 90, no. 2, p. 021001, 2018.

[23] S. S. Li, J. B. Xia, Z. L. Yuan, Z. Y. Xu, W. Ge, X. R. Wang, Y. Wang, J. Wang and L. L. Chang, "Effective-mass theory for InAs/GaAs strained coupled quantum dots," *Physical review B,* vol. 54, no. 16, p. 11575, 1996.

[24] P. D. Wang, N. N. Ledentsov, C. M. Sotomayor Torres, P. S. Kopev and V. M. Ustinov, "Optical characterization of submonolayer and monolayer InAs structures grown in a GaAs matrix on (100) and high-index surfaces," *Applied physics letters,* vol. 64, no. 12, pp. 1526-1528, 1994.

[25] Z. G. Lu, J. R. Liu, P. J. Poole, Y. C. Song and S. D. Chang, "Ultra-narrow linewidth quantum dot coherent comb lasers with self-injection feedback locking," *Optics express,* vol. 26, no. 9, pp. 11909-11914, 2018.

[26] W. Ouerghui, A. Melliti, M. A. Maaref and J. Bloch, "Dependence on temperature of homogeneous broadening of InGaAs/InAs/GaAs quantum dot fundamental transitions," *Physica E: Low-dimensional Systems and Nanostructures,* vol. 28, no. 4, pp. 519-524, 2005.

[27] J. Frenkel, Wave Mechanics; Advanced General Theory, Oxford: Clarendon Press, 1934.

[28] T. Takagahara, "Electron-phonon interactions and excitonic dephasing in semiconductor nanocrystals," *Physical Review Letters,* vol. 71, no. 21, p. 3577, 1993.

[29] Z. Xu, Y. Zhang and J. M. Hvam, "Long luminescence lifetime in self-assembled InGaAs/GaAs quantum dots at room temperature," *Applied Physics Letters,* vol. 93, no. 18, p. 183116, 2008.

[30] S. Sabri, R. Malek and K. Kassmi, "A theoretical study of InAs/InP and InAs/GaAs QDs systems: Formation mechanisms and photoluminescence characterization," *Materials Today: Proceedings,* 2022.

[31] M. Richter, "Nanoplatelets as material system between strong confinement and weak confinement," *Physical Review Materials,* vol. 1, no. 1, p. 016001, 2017.

[32] B. Lounis and M. Orrit, "Single-photon sources," *Reports on Progress in Physics,* vol. 68, no. 5, p. 1129, 2005.

[33] G. Kiršanskė, H. Thyrrestrup, R. Daveau, C. Dreeßen, T. Pregnolato, L. Midolo, P. Tighineanu, A. Javadi, S. Stobbe, R. Schott and A. Ludwig, "Indistinguishable and efficient single photons from a quantum dot in a planar nanobeam waveguide," *Physical Review B,* vol. 96, no. 16, p. 165306, 2017.

[34] C. Vieu, F. Carcenac, A. Pepin, Y. Chen, M. Mejias, A. Lebib, L. Manin-Ferlazzo, L. Couraud and H. Launois, "Electron beam lithography: resolution limits and applications," *Applied surface science,* vol. 164, no. 1-4, pp. 111-117, 2000.

[35] U. Woggon, S. Gaponenko, W. Langbein, A. Uhrig and C. Klingshirn, "Homogeneous linewidth of confined electron-hole-pair states in II-VI quantum dots," *Physical Review B,* vol. 47, no. 7, p. 3684, 1993.

[36] J. Grim, A. Bracker, M. Zalalutdinov, S. Carter, A. Kozen, M. Kim, C. Kim, J. Mlack, M. Yakes, B. Lee and D. Gammon, "Scalable in operando strain tuning in nanophotonic waveguides enabling three-quantum-dot superradiance," *Nature materials,* vol. 18, no. 9, pp. 963-969, 2019.

[37] J. H. Kim, S. Aghaeimeibodi, C. J. Richardson, R. P. Leavitt and E. Waks, "Super-radiant emission from quantum dots in a nanophotonic waveguide," *Nano Letters,* vol. 18, no. 8, pp. 4734-4740, 2018.

[38] A. Bennett, R. Patel, J. Skiba-Szymanska, C. Nicoll, I. Farrer, D. Ritchie and A. Shields, "Giant Stark effect in the emission of single semiconductor quantum dots," *Applied Physics Letters,* vol. 97, no. 3, p. 031104, 2010.

[39] R. Rinaldi, P. V. Giugno, R. Cingolani, H. Lipsanen, M. Sopanen, J. Tulkki and J. Ahopelto, "Zeeman effect in parabolic quantum dots," *Physical Review Letters,* vol. 77, no. 2, p. 342, 1996.

[40] R. Hanson, B. Witkamp, L. M. K. Vandersypen, L. W. van Beveren, J. M. Elzerman and L. P. Kouwenhoven, "Zeeman energy and spin relaxation in a one-electron quantum dot," *Physical Review Letters,* vol. 91, no. 19, p. 196802, 2003.

[41] J. Wang, A. Santamato, P. Jiang, D. Bonneau, E. Engin, J. Silverstone, M. Lermer, J. Beetz, M. Kamp, S. Höfling, M. Tanner, C. Natarajan, R. Hadfield, S. Dorenbos, V. Zwiller, J. O'Brien and M. Thompson, "Gallium arsenide (GaAs) quantum photonic waveguide circuits," *Optics Communications,* vol. 327, pp. 49-55, 2014.

[42] A. Brańczyk, "Hong-ou-mandel interference," *arXiv preprint arXiv:1711.00080,* 2017.

[43] D. Chang, J. Douglas, A. González-Tudela, C. Hung and H. Kimble, "Colloquium: Quantum matter built from nanoscopic lattices of atoms and photons.," *Reviews of Modern Physics,* vol. 90, no. 3, p. 031002, 2018.

[44] A. Van Loo, A. Fedorov, K. Lalumiere, B. Sanders, A. Blais and A. Wallraff, "Photon-mediated interactions between distant artificial atoms," *Science,* vol. 342, no. 6165, pp. 1494-1496, 2013.

[45] P. Borri, W. Langbein, S. Schneider, U. Woggon, R. L. Sellin, D. Ouyang and D. Bimberg, "Ultralong dephasing time in InGaAs quantum dots.," *Physical Review Letters,* vol. 87, no. 15, p. 157401, 2001.

[46] H. D. Robinson and B. B. Goldberg, "Light-induced spectral diffusion in single self-assembled quantum dots," *Physical Review B,* vol. 61, no. 8, p. R5086, 2000.

[47] P. Lodahl, S. Mahmoodian, S. Stobbe, A. Rauschenbeutel, P. Schneeweiss, J. Volz, H. Pichler and P. Zoller, "Chiral quantum optics," *Nature,* vol. 541, no. 7638, pp. 473-480, 2017.

[48] C. Gonzalez-Ballestero, A. Gonzalez-Tudela, F. Garcia-Vidal and E. Moreno, "Chiral route to spontaneous entanglement generation," *Physical Review,* vol. 92, no. 15, p. 155304, 2015.

[49] R. J. Coles, D. M. Price, J. E. Dixon, B. Royall, E. Clarke, P. Kok, M. S. Skolnick, A. M. Fox and M. N. Makhonin, "Chirality of nanophotonic waveguide with embedded quantum emitter for unidirectional spin transfer," *Nature communications,* vol. 7, no. 1, p. 11183, 2016.

[50] K. Yee, "Numerical solution of initial boundary value problems involving Maxwell's equations in isotropic media," *IEEE Transactions on antennas and propagation,* vol. 14, no. 3, pp. 302-307, 1966.

[51] S. Adams, J. Payne and R. Boppana, "Finite difference time domain (FDTD) simulations using graphics processors," in *DoD High Performance Computing Modernization Program Users Group Conference*, 2007.

[52] G. Mur, "Absorbing boundary conditions for the finite-difference approximation of the time-domain electromagnetic-field equations," *IEEE transactions on Electromagnetic Compatibility,* vol. 4, pp. 377-382, 1981.

[53] D. Markovich, K. Ladutenko and P. Belov, "Performance of FDTD method CPU implementations for simulation of electromagnetic processes," *Progress in Electromagnetics Research,* vol. 139, pp. 655-670, 2013.

[54] M. Bahadoran, A. Seyfari, P. Sanati and L. Chua, "Label free identification of the different status of anemia disease using optimized double-slot microring resonator," *Scientific Reports,* vol. 12, no. 1, pp. 1-10, 2022.

[55] K. Levenberg, "A method for the solution of certain non-linear problems in least squares," *Quarterly of applied mathematics 2,* vol. 2, no. 2, pp. 164-168, 1944.

[56] L. Zhang, M. Gu, T. Jia, R. Xu, C. Wan, L. Kang, J. Chen and P. Wu, "Multimode fiber coupled superconductor nanowire single-photon detector," *IEEE Photonics Journal,* vol. 6, no. 5, pp. 1-8, 2014.

[57] J. R. Johansson, P. D. Nation and F. Nori, "QuTiP: An open-source Python framework for the dynamics of open quantum systems," *Computer Physics Communications,* vol. 183, no. 8, pp. 1760-1772, 2012.

[58] R. Chetrite and K. Mallick, "Quantum fluctuation relations for the Lindblad master equation," *Journal of statistical physics,* vol. 148, no. 3, pp. 480-501, 2012.

[59] L. Sapienza, M. Davanço, A. Badolato and K. Srinivasan, "Nanoscale optical positioning of single quantum dots for bright and pure single-photon emission," *Nature communications,* vol. 6, no. 1, pp. 1-8, 2015.

[60] T. Kojima, K. Kojima, T. Asano and S. Noda, "Accurate alignment of a photonic crystal nanocavity with an embedded quantum dot based on optical microscope photoluminescence imaging," *Applied Physics Letters,* vol. 102, no. 1, p. 011110, 2013.

[61] P. R. Nawrocki, V. R. Nielsen and T. J. Sørensen, "A high-sensitivity rapid acquisition spectrometer for lanthanide (III) luminescence," *Methods and Applications in Fluorescence,* vol. 10, no. 4, p. 045007, 2022.

[62] Teledyne, "PyLoN_100_Datasheet," Princeton Instruments, 9 September 2020. [Online]. Available: https://www.princetoninstruments.com/wp-content/uploads/2020/04/PyLoN_100_Datasheet.pdf. [Accessed 4 January 2023].

[63] J. Liu, M. Davanço, L. Sapienza, K. Konthasinghe, J. De Miranda Cardoso, J. Song, A. Badolato and K. Srinivasan, "Cryogenic photoluminescence imaging system for nanoscale positioning of single quantum emitters," *Review of Scientific Instruments,* vol. 88, no. 2, p. 023116, 2017.

[64] C. M. Natarajan, M. G. Tanner and R. H. Hadfield, "Superconducting nanowire single-photon detectors: physics and applications," *Superconductor science and technology,* vol. 25, no. 6, p. 063001, 2012.

[65] A. J. Kerman, E. A. Dauler, W. E. Keicher, J. K. Yang, K. K. Berggren, G. Gol'Tsman and B. Voronov, "Kinetic-inductance-limited reset time of superconducting nanowire photon counters," *Applied physics letters,* vol. 88, no. 11, p. 111116, 2006.

[66] W. Becker, A. Bergmann, M. A. Hink, K. König, K. Benndorf and C. Biskup, "Fluorescence lifetime imaging by time-correlated single-photon counting," *Microscopy research and technique,* vol. 63, no. 1, pp. 58-66, 2004.

[67] H. Conrad, J. Fricke and G. Reichenauer, "High resolution neutron spectroscopy of the crossover in the vibrational density of states of silica aerogels," *Le Journal de Physique Colloques,* vol. 50, no. C4, pp. C4-157, 1989.

[68] M. Zhu, H. Wei, X. Wu and Y. Li, "Fabry-Perot interferometer with picometer resolution referenced to an optical frequency comb," *Optics and Lasers in Engineering,* vol. 67, pp. 128-134, 2015.

[69] Photonic Solutions, "Wavelength Converter," Photonic Solutions, 3 September 2017. [Online]. Available: https://www.photonicsolutions.co.uk/wavelengths.php. [Accessed 3 February 2023].

[70] A. Faraon, I. Fushman, D. Englund, N. Stoltz, P. Petroff and J. Vučković, "Dipole induced transparency in waveguide coupled photonic crystal cavities," *Optics Express,* vol. 16, no. 16, pp. 12154-12162, 2008.

[71] L. Hajshahvaladi, H. Kaatuzian and M. Danaie, "Design of a hybrid photonic-plasmonic crystal refractive index sensor for highly sensitive and high-resolution sensing applications," *Physics Letters A,* vol. 420, p. 127754, 2021.

[72] D. Robinson and J. Schneider, "On the use of the geometric mean in FDTD near-to-far-field transformations," *IEEE transactions on antennas and propagation,* vol. 55, no. 11, pp. 3204-3211, 2007.

[73] N. Prtljaga, R. J. Coles, J. O'Hara, B. Royall, E. Clarke, A. M. Fox and M. S. Skolnick, "Monolithic integration of a quantum emitter with a compact on-chip beam-splitter," *Applied Physics Letters,* vol. 104, no. 23, p. 231107, 2014.

[74] X. Xu, Z. Xie, J. Zheng, J. Liang, T. Zhong, M. Yu, S. Kocaman, G. Lo, D. Kwong, D. Englund and F. Wong, "Near-infrared Hong-Ou-Mandel interference on a silicon quantum photonic chip," *Optics Express,* vol. 21, no. 4, pp. 5014-5024, 2013.

[75] N. Prtljaga, C. Bentham, J. O'Hara, B. Royall, E. Clarke, L. Wilson, M. Skolnick and A. Fox, "On-chip interference of single photons from an embedded quantum dot and an external laser," *Applied Physics Letters,* vol. 108, no. 25, p. 251101, 2016.

[76] F. Xia, L. Sekaric and Y. A. Vlasov, "Mode conversion losses in silicon-on-insulator photonic wire based racetrack resonators," *Optics express,* vol. 14, no. 9, pp. 3872-3886, 2006.

[77] L. Midolo, S. Hansen, W. Zhang, C. Papon, R. Schott, A. Ludwig, A. Wieck, P. Lodahl and S. Stobbe, "Electro-optic routing of photons from a single quantum dot in photonic integrated circuits," *Optics Express,* vol. 25, no. 26, pp. 33514-33526, 2017.

[78] M. Felicetti, K. Kojima, T. Koike-Akino, B. Wang, K. Parsons, S. Nishikawa and E. Yagyu, "MMI-based polarization beam splitter/combiner for InP photonic integrated circuits," *Optica Publishing Group,* pp. IM2A-5, 2015.

[79] J. Alama, "The rank+nullity theorem," *Formalized Mathematics,* vol. 15, no. 3, pp. 137-142, 2007.

[80] K. Cooney and F. Peters, "Analysis of multimode interferometers," *Optics Express,* vol. 24, no. 20, pp. 22481-22515, 2016.

[81] L. Coldren, S. Corzine and M. Mashanovitch, Diode lasers and photonic integrated circuits, John Wiley & Sons, 2012.

[82] K. Latunde-Dada and F. Payne, "Theory and design of adiabatically tapered multimode interference couplers," *Journal of Lightwave Technology,* vol. 25, no. 3, pp. 834-839, 2007.

[83] C. Chen and C. Chiu, "Taper-integrated multimode-interference based waveguide crossing design," *IEEE Journal of Quantum Electronics,* vol. 46, no. 11, pp. 1656-1661, 2010.

[84] X. Zhou, I. Kulkova, T. Lund-Hansen, S. Hansen, P. Lodahl and L. Midolo, "High-efficiency shallow-etched grating on GaAs membranes for quantum photonic applications," *Applied Physics Letters,* vol. 113, no. 25, p. 251103, 2018.

[85] G. Sallen, A. Tribu, T. Aichele, R. André, L. Besombes, C. Bougerol, M. Richard, S. Tatarenko, K. Kheng and J. P. Poizat, "Subnanosecond spectral diffusion of a single quantum dot in a nanowire," *Physical Review B,* vol. 84, no. 4, p. 041405, 2011.

Glossary

μ

μ-PL
micro-photoluminescence spectroscopy ... 37, 38, 39, 92, 93, 95, 108

0

0.5 NA
0.5 numerical aperture value..... 53, 60

A

ADC
analog-to-digital converter..... 41
APD
avalanche photodiode 43, 44, 107, 108, 109

C

CCD
charge-coupled device..... 37, 39
CFD
constant fraction discriminator 41
CW
continuous wave 42, 44, 108, 109

D

DC
directional coupler.. 20, 63, 64, 65, 66, 67, 68, 69, 70, 71, 72, 73, 74, 84

E

EBL
electron beam lithography..... 14, 87

F

FDTD
finite-difference time-domain simulation .. 30, 31, 32, 47, 48, 51, 58, 65, 66, 76, 77, 87
FOB
fibre-optic splitter..... 42, 43
FPI
Fabry-Pérot interferometry.. 43, 44, 106, 107, 108, 109
FWHM
full width at half maximum 10, 35, 44, 45, 114

G

g2
second-order photon correlation.....24, 25, 26, 33, 34, 35, 40, 111, 112, 113, 114, 115

H

HBT
Hanbury Brown-Twiss 40, 42, 111, 112, 113, 114, 115
HH
heavy-hole..... 9, 10

L

LDSD
the Low Dimensional Structures and Devices group ..... , 116
LED
light-emitting diode 37, 38
LH
light-hole..... 9, 10

M

MATLAB
matrix laboratory 39, 91, 95
MBE
molecular beam epitaxy..... 3, 4
MLE
maximum likelihood estimation..... 39, 96
MMI
multimode interferometer . 73, 74, 75, 76, 77, 78, 79, 80, 81, 82, 83, 84, 85, 86, 87, 88, 89, 90, 91

N

NBWG
nanobeam waveguide...13, 14, 23, 28, 38, 40, 42, 43, 60, 62, 92, 97, 98, 106, 108, 114, 116

P

PL
photoluminescence 5, 10, 11
PLE
photoluminescence excitation..... 10
PSF
point-spread function 39, 95, 96

Q

QD